Faculty of Engineering, Built Environment and Information Technology

Helically coiled cavity receiver for a micro-scale direct generation steam Rankine cycle using a novel solar dish design

by

Jonathan Kyle Swanepoel

Supervisors: Dr WG le Roux and Dr AS Lexmond
Co-supervisor: Prof JP Meyer

Submitted in partial fulfilment of the requirements for the degree
Master of Engineering (Mechanical Engineering)

UNIVERSITY OF PRETORIA

2019

Abstract

Title:	Helically coiled cavity receiver for a micro-scale direct generation steam Rankine cycle using a novel solar dish design.
Supervisors:	Dr WG le Roux and Dr AS Lexmond
Co-supervisor:	Prof JP Meyer
Department:	Mechanical and Aeronautical Engineering
Degree:	Master of Engineering (Mechanical Engineering)

Sub-Saharan Africa has an underutilised solar resource that is available to provide distributed-scale power to rural communities that are not reached by the current grid systems that are in place. Renewable power generation systems are typically infeasible for this purpose due to their high manufacturing and maintenance costs. This research proposes to address this by experimentally investigating the performance of a micro-scale, solar thermal Rankine cycle with direct steam generation using an affordable solar collector design. The intended power generation range is between 0.1 and 1 kW, which can be used for the direct mechanical pumping of rural irrigation systems or municipal water supplies. The study focuses on the performance of the solar collector (the solar reflector and the solar receiver) under realistic solar thermal conditions in sub-Saharan Africa, as it is considered to be one of the most important components in the solar thermal Rankine cycle. The performance of the solar collector was first characterised in an optical analysis of the new faceted dish reflector design, which comprised six Mylar membranes stretched over the elliptical rims of television satellite dishes. The optical analysis was conducted with the main goal of determining how much concentrated solar radiation would intercept the experimental receiver aperture during solar testing. This was determined by measuring the reflectivity of the reflector facets through ultraviolet and visible light (UV-VIS) spectroscopy and producing an intercept factor trend as a function of receiver aperture size through photographic lunar flux mapping. Based on the spectroscopy analysis, the spectral reflectivity of the clean Mylar facets was determined to be 97% for the visible light spectrum. The intercept factor was determined to be 87% for the designed receiver aperture diameter of 135 mm. The thermal testing took place on a clear, sunny day with low wind velocities. The solar collector followed the arc of the sun throughout the day with a 1° tracking error. During the testing, municipal water was passed through the receiver at 0.284 g/s and the temperature and pressure within the receiver were recorded. A 91-minute testing period occurred, where the inlet and outlet process flows obtained relatively constant operating temperatures with the inlet temperature at 54 °C and the outlet temperature at 343 °C. The total solar irradiance dropped from 801 to 705 W/m^2 during this

testing period. Using a reflector with a total incident area of 2.73 m^2, the total radiation intercepted at the aperture dropped from 1 845 to 1 625 W during this period. The total power capture by the working fluid averaged at approximately 861 W and the total rate of heat loss was determined to be between 1 000 and 750 W. An average collector efficiency of 42% and an average receiver efficiency of 49% were determined for the testing period. An analysis of the heat loss showed that approximately 84% of the heat was lost through the aperture, of which, 31% was from reflected radiation. The second-law analysis showed that most of the irreversibility in the solar collector was caused by absorption of the concentrated radiation at the coil surface. This was because of the large temperature difference between the sun and the receiver coils. The experimental thermal analysis highlighted the design challenges of the micro-scale thermal Rankine cycle. However, the analysis showed that a solar collector can be constructed using locally sourced, affordable materials and can be used to produce power at a micro-scale. With appropriate attention given to optimising the collector design and determining the optimum operating conditions of the solar receiver, the power cycle would be able to compete with current technologies to provide decentralised power to communities in need.

Acknowledgements

Above all, I would like to thank my Lord and Saviour for supporting me and helping me overcome the challenges that I faced. This work was done for His glory and the extension of his kingdom here on earth.

I would also like to extend my gratitude towards the following people who supported me in my endeavours:

- Dr Willem G le Roux for the financial support and fundamental guidance throughout the year.
- Dr Axel S Lexmond for his helpful contribution towards the design and thermal analysis of the experimental model.
- Mr Peet Kruger, Mr Edwin Mohale, Mr Chris Govinder and Mr Donald Keeste for their experienced technical support during the design and construction phase of the research.
- Dr Radhakrishnan for her assistance in the UV/VIS spectrometry analysis.
- Mr George Breitenbach and Mr Leandrew Pestana for their assistance in the photogrammetry analysis.
- Mr Casey Roosendaal for the research collaboration during the optical analysis.
- Mr Vincent Good for his assistance in photography during the lunar flux testing.

I would like to thank the South African Universities Radiometric Network (SAURAN) for providing the solar and weather measurements that were used in the research. I would also like to extend my gratitude to Prof Josua P Meyer and the various institutions that provided the financial support I needed during my studies. These included the following:

- Department of Science and Innovation
- National Research Foundation
- Technology Innovation Agency

Opinions expressed, and conclusions arrived at are those of the author and are not necessarily to be attributed to the DRT, NRF or TIA.

Finally, I would like to thank my family for supporting me and keeping me motivated throughout my endeavours, all the way through to the completion of my research. To my life partner, Ms Lauren Kay Pijper, for the fundamental support both emotionally and as my assistant during the experimental analyses. This work would not have been completed in time without your support.

Table of Contents

List of figures

List of tables

List of symbols

Alphabetical symbol	Description	Unit
A	Area	m^2
A	Major axis length	m
A'	New major axis length	m
a	Scaling equation coefficient	-
B	Minor axis length	m
B	Boiling suppression factor	-
b	Positional equation coefficient	-
b	Measurement bias	-
Bo	Boiling number	-
C	Constant	-
C	Concentration coefficient	-
Co	Convection number	-
Cp	Specific heat	J/kg.K
D	Diameter	m
d	Delta	-
Dn	Dean number	-
E	Pixel value	V/m^2
F	Convective boiling enhancement factor	-
F	View factor	-
f	Focal length	m
f	Function	-
f	Friction factor	-
G	Mass flux	$Kg/s.m^2$
g	Gravitational acceleration (9.81 m/s^2)	m/s^2
Gr	Grashof number	-
H	Enthalpy	J
H	Height	m
h	Specific enthalpy	J/kg
$\bar{h}$	Convection heat transfer coefficient	$W/m^2.K$
I	Irradiance	W/m^2
$\bar{I}$	Irreversibility	W
IF	Intercept factor	-
K	Thermal scaling factor	W/m^2
k	Thermal conductivity	W/m.°C
L	Length	m
m	Mass	kg
$\dot{m}$	Mass flow rate	kg/s
Nu	Nusselt number	-

Alphabetical symbol	Description	Unit
n	Experimental constant	-
n	Sample size	-
P	Pressure	Pa
Pr	Prandtl number	-
$\dot{Q}$	Heat transfer rate	W
$\dot{q}$	Heat flux	W/m^2
R	Thermal resistance	W/K
Ra	Rayleigh number	-
Re	Reynolds number	-
Ri	Richardson number	-
s	Linear displacement	m
s	Geometric constant	-
s	Specific entropy	J/kg.K
T	Temperature	°C
TC	Thermocouple	-
t	Thickness	m
V	Average velocity	m/s
v	Kinematic viscosity	m^2/s
x	Vapour quality	-
x	x-coordinate	m
x	Measured value	-
y	y-coordinate	m
y	Output parameter	-
z	z-coordinate	m

Greek symbol	Description	Unit
α	Thermal diffusivity	m^2/s
α	Absorptivity	-
β	Thermal expansion coefficient	1/K
ΔW	Change in work	W
$\Delta\Phi$	Change in available work	W
$\Delta\Psi$	Change in exergy	W
ΔP	Change in pressure	Pa
δ	Standard uncertainty	-
ε	Emissivity	W/m^2K^4
η	Efficiency	-
θ	Elevation angle	° (degrees)
ϑ	Tilt coefficient	-
λ	Wavelength	nm
μ	Dynamic viscosity	kg/m.s
ρ	Density	Kg/m^3
ρ	Reflectivity	-
σ	Surface tension	N/m
σ	Stephan Boltzmann constant	W/m^2K^4
τ	Shear stress	Pa
τ	Transmissivity	-
Φ	Available work	W
φ	Inclination angle	° (degrees)
ϕ^2	Pressure drop multiplier	-
χ	Martinelli parameter	-
Ψ	Exergy	W
ψ	Rim angle	° (degrees)

Subscript symbol	Description
$2nd$	Second law
∞	Ambient
abs	Absorbed
acc	Acceleration
ap	Aperture
$approx$	Approximate
avg	Average
b	Bulk fluid property
$back$	Back
$bottom$	Bottom
CP	CoolProp
c	Characteristic parameter
$camera$	Camera
cav	Cavity
$coil$	Coil
$combined$	Combined
$cond$	Conduction
$conv$	Convection
cr	Critical condition
cs	Cross-section
$dish$	Dish
$emitted$	Emitted
f	Film property
f	Fluid
fg	Liquid to gas
$forced$	Forced convection
fr	Friction
$front$	Front
g	Gas
$grav$	Gravity
h	Hydraulic diameter
i	Inner wall
i	Increment
img	Photographic image
in	Control volume inlet
ins	Insulation
$intercept$	Intercepted
j	Increment
L	Characteristic length
LFM	Lunar flux mapping
l	Liquid
$left$	Left
lo	Liquid only
$loss$	Loss from control volume

Subscript symbol	Description
m	Mixture
max	Maximum
min	Minimum
$mylar$	Mylar facet
$natural$	Natural convection
net	Net
$nucleate$	Nucleate boiling
o	Outer wall
op	Optical
out	Control volume outlet
$prop$	Fluid property
$python$	Python code
rad	Radiation
ref	Reflectivity
ref	Reference
$right$	Right
rim	Rim of facet or dish
s	Surface
sat	Saturation
sf	Solid-fluid
$steel$	Steel
sun	Sun
$surr$	Surroundings
TP	Two-phase
TS	Target surface
th	Thermal efficiency
top	Top
tot	Total
tt	Turbulent-turbulent
v	Vapour
w	Working fluid (water)
$wind$	Wind

Acronym	Description
3D	Three-dimensional
CCD	Charge coupled device
CHP	Combined heat and power
CSP	Concentrated solar power
DNI	Direct normal irradiance
GIS	Geographic information system
IAPWS	International Association of Properties of Water and Steam
PHLUX	Photographic flux mapping
PHLLUX	Photographic lunar flux mapping method
PV	Photovoltaic
RMS	Root mean square
TC	Thermocouple
TES	Thermal energy storage
T-s	Temperature versus entropy diagram
UV-VIS	Ultraviolet and visible light
WHR	Waste heat recovery

1. Introduction

1.1 Background

There is currently an increasing demand for off-grid power generation systems in Africa, where rural settlements such as villages or farms, which are located outside urban areas such as towns or cities, experience inflated rates of electricity supply or may not be reached by on-grid supply at all. This is mainly due to the fact that these rural settlements are sparsely located, which makes the process of extending the grid to these settlements an infeasible option in the short- or medium-term development process [1].

The supply of energy plays an important role in nearly all aspects of human welfare. Some of these aspects include heating, air circulation, agricultural production, job creation, healthcare and education. Beneficial aspects of electrification primarily pertain to health benefits when substituting fuel-burning processes in the household with electrical alternatives [2]. The provision of adequate power to households negates the need for indoor kerosene lamps and candles, which emit harmful by-products such as carbon monoxide, nitric oxide and sulphur dioxide, which lead to lung disease. Alternatives to fuel-fired cooking would further stem the health risk of smoke inhalation [3].

In the sub-Saharan African region, a study by the International Energy Agency showed that although a grid expansion of 7% has been achieved since 2010, the population without access to electricity has increased from 518 million to 588 million between 2000 and 2016 [4]. One study claims that sub-Saharan Africa is the only region in which the percentage of its population without access to electricity is expected to increase in the coming future [5]. Studies show that the emerging middle class in Africa will facilitate a large growth in the demand for electricity in the future. Coupled with the inadequate grid supply, the potential becomes apparent for the production of distributed mini-grid systems where power may be generated closer to rural settlements [6, 7].

In South Africa, the Department of Energy considers electricity to be every citizen's constitutional right, regardless of their location. The Department views electrification as a tool to positively affect poverty alleviation and education. However, in acknowledging the fact that operational costs can generally not be recovered when supplying on-grid electricity to poorer settlements, the Department currently regards the expansion of the grid network into such settlements to be infeasible and unsustainable in the long term [8].

1.1.1 Comparing methods of power generation

Means of generating power using mini-grid solutions within sub-Saharan Africa range from fossil fuel power generation to more renewable methods such as biomass, wind, hydro, solar, geothermal and nuclear power generation. With the ever-increasing presence of climate change, the need to look for renewable solutions becomes more evident. When considering sub-Saharan Africa, mini-grids that are powered by renewable energy become a very relevant solution in addressing energy poverty in these countries. Renewable power generation provides a sustainable means of electricity where the dependence on foreign fuel supply is decreased. Three prominent renewable generation methods, according to energy potential, come into focus. These are wind, hydro and solar power generation [1]. Since the purpose of mini-grid systems is to provide settlements or households, which have been developed in a decentralised manner, with power, wind and solar power generation methods become a more prevalent option. This is because of their sources of power (wind velocity and solar irradiance), which are mostly present throughout the region. In the case of hydropower, even though the energy potential within most countries is notable, the way in which dams need to be built has the potential to displace communities upstream, as well as affect environments downstream. Fundamentally, this does not solve the solution of feasible energy provision to distributed rural communities [9, 10].

In comparing the energy potential of both wind and solar, an energy potential map of Africa is considered. Belward et al. [11] illustrated the wind energy potential throughout Africa with a Geographic Information System (GIS)-based approach, which accounted for exclusion zones. These exclusion zones consisted of water bodies, protected zones, forested zones and urban centres. It is evident from Figure 1 that the wind energy potential in sub-Saharan Africa ranges from 5 kWh/m^2 per annum to roughly 15 kWh/m^2 per annum inland, while coastal regions such as coastlines along South Africa, and particularly along the Cape Horn, may reach potentials from 20 to 45 kWh/m^2 per annum. Figure 2 shows the annual sum of the direct normal irradiance across southern Africa. In observing the distribution, it is evident that, apart from the eastern coastal regions along Madagascar and South Africa, as well as regions along the equator, the rest of sub-Saharan Africa experiences an annual sum of direct normal irradiance greater than 2 000 kWh/m^2 per annum [12]. By considering the efficiency with which the irradiance can be transformed into useful work in the general case of photovoltaic (PV) power generation, an energy potential can be determined. The conversion efficiencies of most commercial technologies range from 10 to 20%, with more experimental technologies currently approaching 50% efficiency [13-15]. This shows that the potential of solar energy is well above that of wind in the region. The main reason for the competition between the two methods of power generation is generally the feasible implementation of each method.

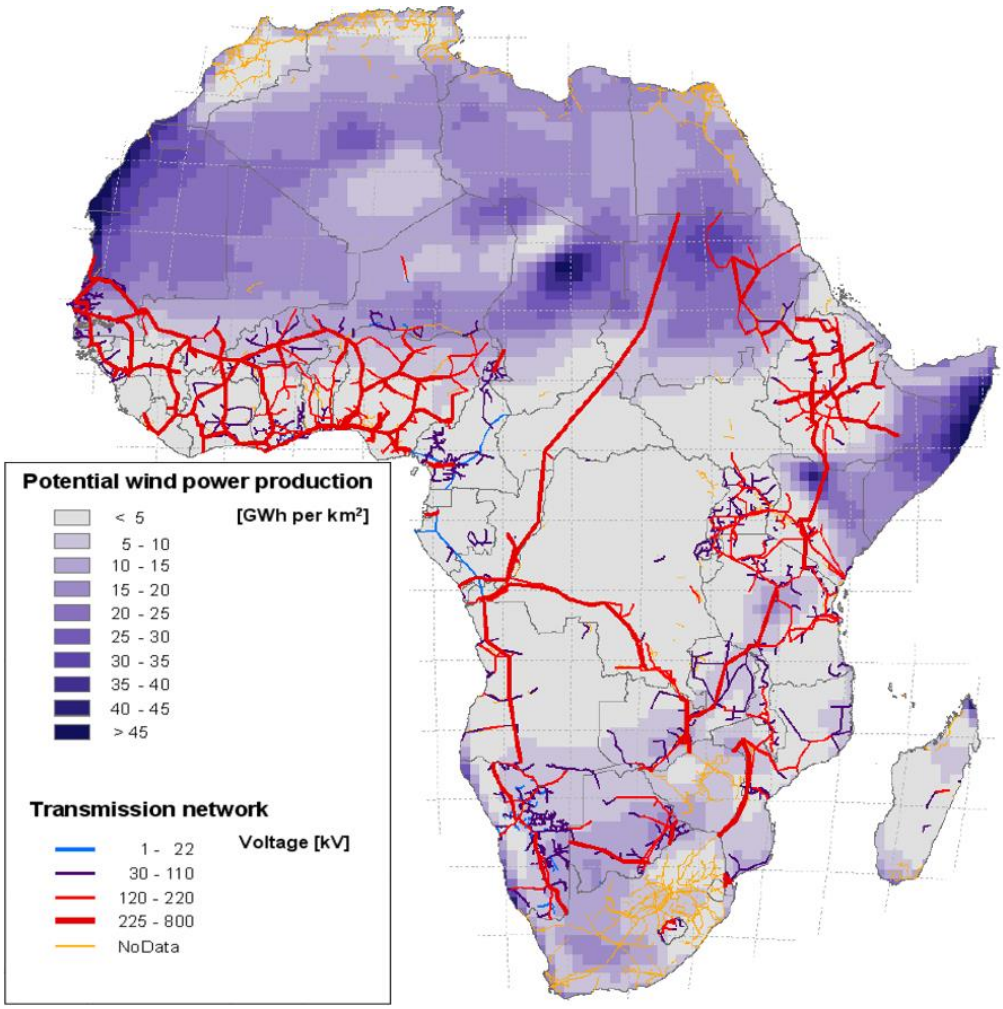

Figure 1: Wind energy potential across southern Africa [11]

1.1.2 Comparison between solar PV and concentrated solar thermal power generation

Micro-scale solar power generation has seen rapid growth in popularity in the past few years due to advancements in technology. Solar power generation in sub-Saharan Africa evidently has a far greater potential than its renewable competitor, wind. For this reason, solar power generation is considered in the current research. There are many ways of harnessing solar power. The prominent method is the use of PV panels, which converts light directly into electrical current through the photoelectric effect [16].

The generated electrical power needs to be stored in a battery or processed by an inverter before it can be used as a means of mitigating the intermittency of the solar energy supply. The use of solar PV generation can be used in both a distributed manner and in centralised power plants since the general case of a PV setup only requires a simple storage and panel addition to increase its capacity. In other words, the scalability of solar PV systems is a direct advantage when compared to other methods such as concentrated solar thermal generation.

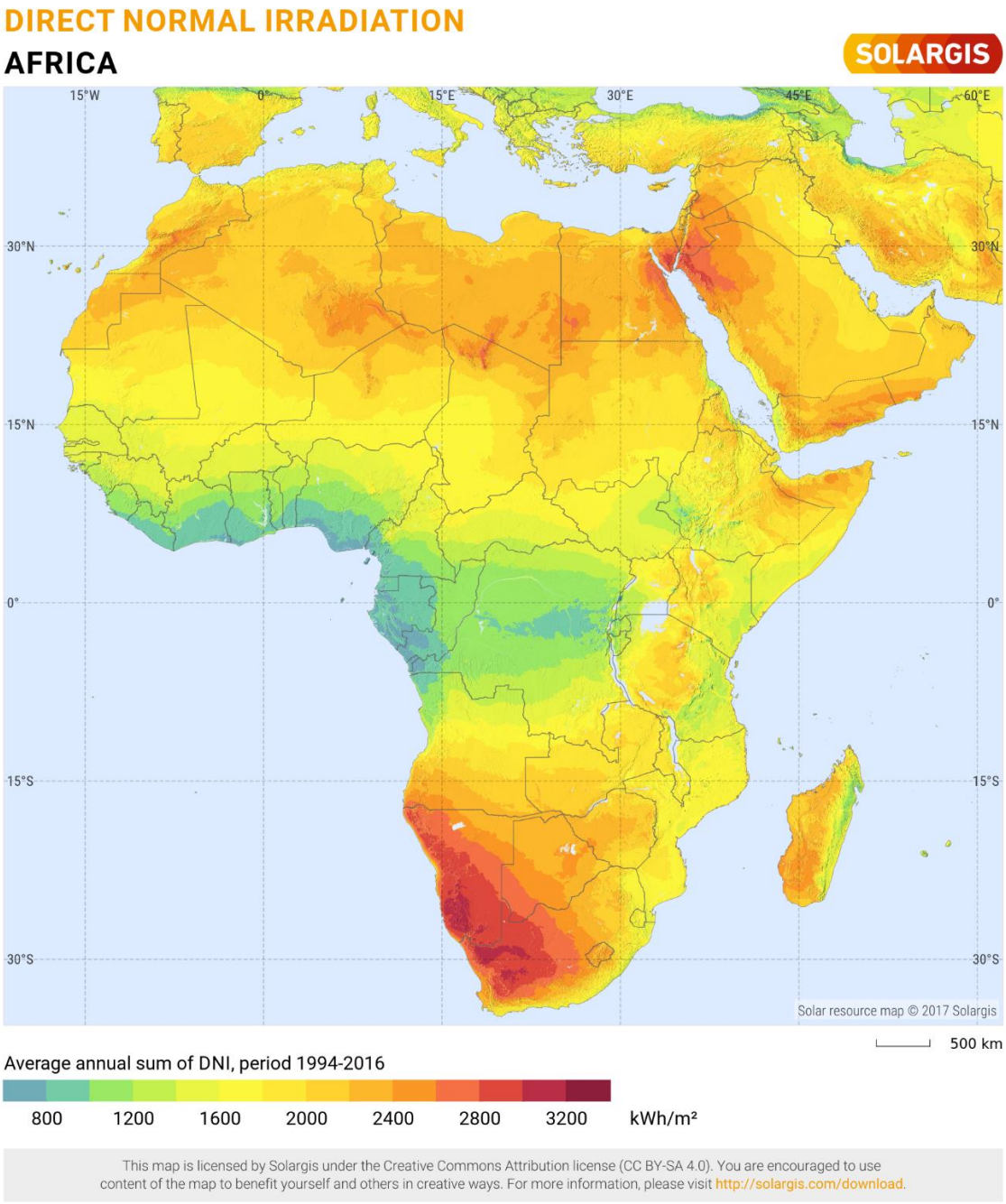

Figure 2: Direct normal irradiation in southern Africa [12]

Quansah et al. [17] discuss the prospects of implementing solar PV schemes in the different cases of small-scale, off-grid, decentralised mini-grid and large-scale centralised systems. It was highlighted that decentralised mini-grid PV systems have great potential within sub-Saharan Africa and that micro-scale, off-grid systems are adequate in the short term. However, as the grid network expands, there should be a transition from off-grid solar solutions to grid-connected, decentralised mini-grid systems. This is due to the impractical operational cost of electrical storage in off-grid systems as opposed to grid-connected solutions.

One of the primary disadvantages of solar PV systems is that the effectiveness of the system relies directly on the efficiency of the electrical storage or processing device, since the panels generate electricity directly from the irradiance. An alternative method would be to generate power from the irradiance using concentrated solar thermal systems. This provides an advantage in that thermal energy can easily be stored by means of more environmentally friendly materials. Alva et al. [18] present an overview of current methods of thermal energy storage (TES) and the associated technology and materials. In comparison with battery technology, it is noted that TES does not undergo cycling-induced degradation as rapidly as PV and battery technologies do.

1.1.3 Solar power used in irrigating rural farming settlements in sub-Saharan Africa

One of the advantages of concentrated solar thermal generation is its ability to harness the direct mechanical work output. This provides the option of either using the mechanical power to perform the required work directly, or when no direct mechanical work is required, the system could simply generate electricity similar to that of a PV system. The use of direct mechanical work means that losses that occur due to converting the work into electricity may be mitigated. The mechanical work may be used in rural settlements to power water-pumping systems such as those used in irrigation, as well as general community water supply.

In the early 2000s, Wong and Sumathy [19] reviewed both conventional and unconventional methods of solar pumping systems. Conventional solar PV systems were considered, along with solar thermal steam cycles. Both PV and solar thermal methods were considered infeasible due to PV's high procurement cost and CSP's high maintenance costs and low efficiency at the time of research. In order to suit the likely purpose of powering pumping systems for rural farming villages, the start-up and operating costs would have to be relatively inexpensive and simple to operate and maintain. As time progressed and technology advanced, the initial cost of both PV and concentrated solar technology declined, and researchers started to look at both methods as a feasible option for powering irrigation pumps.

Ali [20] performed a comparative feasibility study on possible methods for solar irrigation pumps to be implemented in agriculture in Sudan. In this study, the conventional methods of concentrated solar thermal and solar PV power generation were compared. It was determined that, although concentrated solar systems, particularly the concentrating dish, water pumping systems had a conversion efficiency of 22%, which was roughly 6.5 times more efficient than a solar PV system, which had a conversion efficiency of 3.4%. The normalised energy cost of solar PV power generation in $/kWh outperformed concentrated solar by a factor of 2. Although the study did not promote concentrated

solar as a dominant method, very little research was focused on the climate conditions of sub-Saharan Africa and its effect on viably implementing solar pumping systems in irrigating rural farmlands.

Mohammed Wazed et al. [21] presented a review of solar irrigation systems and discussed their sustainability in the context of rural sub-Saharan Africa. It was noted that, in comparison with solar PV systems, concentrated solar systems had received substantially less attention in research for the purpose of micro-scale solar irrigation systems within the region. It was also noted that one of the main drawbacks of a solar PV system was the large carbon footprint currently associated with the construction and importation of associated parts for solar PV systems into Africa, since there is a lack of manufacturing facilities for such units in Africa. The report states that concentrated solar systems have a large potential to power irrigation systems in rural farming settlements in the region, but very little research is available pertaining to the feasibility of implementing such methods.

1.1.4 Experimental performance of solar thermal power cycles

During the planning phase of the research, it is important to review experimental work pertaining to the analysis of solar thermal power cycles in order to determine acceptable research parameters that are based on what has been done in the past. The focus of the literature study is on the experimental analysis of solar receivers, since this is what will be considered in the current research.

Zhu et al. [22] carried out an experimental investigation on a parabolic dish receiver to determine the heat transfer characteristics of the receiver under real conditions using a Brayton cycle for power generation. A steady-state solar irradiance was achieved for over two hours in the afternoon. The performance was characterised by an energy and exergy analysis. The concentrated radiation heat transfer rate at the receiver aperture was determined to be 1 000 W/m^2 with a direct normal irradiance of roughly 650 W/m^2. During steady-state conditions of the experiment, the thermal efficiency of the receiver was maintained at approximately 80% and the second-law efficiency or exergy efficiency was maintained at approximately 35%. For the analysis, the Brayton cycle's operating conditions were controlled, such as mass flow rate, operating pressure and inlet temperature.

In the analysis of the results, the progression of the Brayton cycle's power and efficiency during the steady-state ambient conditions were presented and discussed. Plots of solar irradiance vs time, the power captured vs time, energy efficiency vs time, heat loss factor vs time, exergy vs time, and exergy efficiency vs time were presented.

Pavlovic et al. [23] performed a set of experiments on a simple, low-cost parabolic dish collector with a spiral absorber to validate a numerical model that was developed. The numerical model was then used to determine the performance of the receiver using different working fluids. Water was used in

the validation experiments. The measured parameters were the water flow rate, the water inlet and outlet temperatures from the receiver, the ambient temperature and wind velocity. The solar radiation was measured using a self-tracking weather station that adjusted at a time step of 30 seconds. Once the numerical model had been validated, the receiver was numerically investigated for the working fluids of water, air and thermal oil. The energy and exergy performance of the receiver was investigated for each working fluid at varying mass flow rates and inlet temperatures.

Bouvier et al. [24] experimentally studied the performance of micro combined heat and power (CHP) generation with a parabolic trough setup using a Rankine cycle with direct steam generation. The micro CHP system produced 19 kW of thermal energy and 1.3 kW of electrical energy and had a solar-to-electricity efficiency of 3%. The receiver performance was characterised by an energy analysis from which the thermal efficiency could be determined. Bouvier et al. [24] used an electrical superheater directly after the receiver to ensure that the steam was in single-phase and to determine the enthalpy state of the fluid at the outlet using temperature and pressure measurements. The additional power input from the electrical superheater could easily be determined from the voltage load of the electrical superheater. The experimental work varied operation pressure, mass flow rate and inlet temperature to the receiver for an estimated constant solar irradiance and measured the performance of the system through an energy analysis.

As seen in the literature, the performance of a solar receiver can be characterised by performing an energy and exergy analysis on the system for the varying parameters of mass flow rate, operating pressure and inlet temperature to the receiver. The energy and exergy states are measured at the inlet and outlet of the receiver for constant solar irradiance, ambient temperature and wind velocity conditions. The energy and second-law efficiency of the receiver can then be determined. This encompasses the aim of the experimental study that is to be conducted in the current research.

1.2 Justification of research

The Brayton and Rankine power cycles were considered as possible power generation methods for the current research. The Brayton cycle is currently being investigated at the University of Pretoria through the work of Dellar et al. [25], Le Roux [26] and Wolff et al. [27]. Therefore, the Rankine cycle is considered in the current investigation. Other current works pertaining to the research of micro-scale Rankine cycles are generally directed towards organic Rankine cycles for the use of waste heat recovery or low temperature solar thermal power generation [28-30]. As an example, the work of Loni et al. [31] focused on the experimental analysis of small-scale, concentrated solar thermal organic Rankine cycles for indirect steam generation using a parabolic dish. Different cavity receiver shapes

were investigated both numerically and experimentally, and receiver efficiencies ranging between 56.44 and 65.14% were obtained using Behran thermal oil as the heat transfer fluid. The outlet temperatures of the heat transfer fluid from the receiver cavities ranged between 92 and 117 °C. Numerical models, characterising the performance of the receiver, were also validated against the experimental results [32, 33]. Organic Rankine cycle power generation generally takes advantage of low-temperature evaporation (80 to 250 °C). Dry fluids are generally considered as the working fluid. These organic fluids are generally harmful to the environment and cannot easily be sourced in rural areas. When considering higher operating temperatures, steam begins to become the more attractive option since its fluid properties are maintained at these temperatures (>250 °C). The higher temperature range is expected when considering super-heated steam generation at pressures above 3 bar from a concentrating dish reflector. For the purpose of rural off-grid power generation, a micro-scale steam Rankine cycle with a helical coil cavity receiver, powered by concentrated solar energy from a parabolic dish, is considered.

As is evident in Section 1.1.4, inadequate literature was found with regard to the experimental investigation of the performance of micro-scale, direct steam generation solar thermal Rankine cycles for realistic solar conditions in sub-Saharan Africa. Coupled with the use of a helically coiled cavity receiver and a novel dish design, the current research is considered novel.

1.3 Problem statement

There is currently insufficient literature available characterising the performance of micro-scale, direct solar thermal power generation, using a Rankine cycle and a concentrating dish, for solar conditions in sub-Saharan Africa. The performance of the cycle's receiver unit is considered to be one of the most important units in a conventional solar Rankine cycle and must be characterised for different operating conditions to allow for a more complete understanding of the overall performance of the cycle.

A more detailed insight will be obtained with regard to the viability of implementing such a method for off-grid power generation to aid rural settlements in sub-Saharan Africa.

1.4 Preliminary target operating conditions for thermal testing

One of the first design goals of the current study was to estimate the mass flow rate of the water as a type of crude approximation since it was suspected that the mass flow rate would be too low for practical purposes, given the intended sizing of the receiver.

It was estimated that a good operating pressure through the receiver, and thus at the inlet of the turbine, would be 6 bar (absolute). The pressure drop through the receiver coil and the connecting pipes was assumed to be negligible. It was initially estimated that 1 000 W of solar energy would be transferred into the water and the inlet water temperature to the receiver was estimated to be 30 °C. Assuming the collector efficiency to be 50% and a direct normal irradiance (DNI) of 1 000 W/m^2, the required incident area of the reflector would have to be 2 m^2. A target outlet temperature from the receiver was selected to be 400 °C, which would be the inlet condition to the turbine, assuming no heat losses occur. The associated thermodynamic properties were determined through CoolProp, an Excel add-on that provides thermodynamic states for different working fluids [34]. A tabulation of the estimated operating conditions is presented in Table 1.

From the energy balance shown in Equation 1-1, the required mass flow rate was calculated to be roughly 0.32 g/s. The mass flow rate is low, but it is considered practically possible to control the flow rate within a tolerance of 0.001 g/s given appropriate experimental equipment.

Table 1: Target operating conditions for the solar receiver

Condition	**Symbol**	**Value**	**Units**
Captured solar power	$\dot{Q}_i$	1 000	W
Operating pressure	P	600 000	Pa
Associated saturation temperature	T_{sat}	158.83	°C
Inlet temperature	T_{in}	30	°C
Outlet temperature	T_{out}	400	°C
Associated inlet enthalpy	h_{in}	126.28	kJ/kg
Associated outlet enthalpy	h_{out}	3 270.78	kJ/kg

$$\dot{Q}_i = \dot{m}_w(h_{out} - h_{in}) \tag{1-1}$$

The heat required for preheating and boiling at the given flow rate was determined to be 0.84 kW, which is 84% of the available heat. The heat required for superheating was determined to be 0.16 kW, which is 16% of the available heat.

1.5 Research objectives

The most important and least understood unit within the solar thermal Rankine cycle is the solar collector (comprising the reflector and the receiver). Characterisation of its performance is a challenge since two-phase flow is expected to occur within the receiver as the water boils. The main objectives of this research can be summarised in the following list.

- Provide a mechanical design for the experimental setup.
- Construct a solar collector that is capable of boiling and superheating steam using concentrated solar power (CSP).
- Perform optical experiments on the novel reflector to characterise its performance.
- Perform thermal experiments on the solar collector, characterising the performance of the receiver throughout the day for realistic operating conditions.
- Analyse the performance of the solar collector through first- and second-law analysis.

1.6 Scope of the research

Since the primary objective of this study is to characterise the performance of a helically coiled cavity receiver for realistic solar conditions in sub-Saharan Africa, the work primarily focuses on the design and study of the experimental receiver, while the other units contained in the Rankine cycle are mimicked. To obtain a mass flow rate in the magnitude of 0.3 g/s, the pumping is mimicked by a water reservoir supplied by a regulated compressed air line to provide a constant supply pressure, and the steam turbine is mimicked using a constant aperture needle valve to provide tight control over the steam mass flow rate. A stainless steel receiver coil that had already been constructed for the purpose of superheating steam is integrated into the receiver design. During the experimental analysis, the receiver is analysed for a set of testing conditions with an operating pressure of 3 bar and an average DNI of 757 W/m^2.

This, of course, differs from the initial estimate presented in Table 1. Unforeseen erratic pressure pulsations that occurred in preliminary testing meant that the supply pressure was lowered in the interest of safety.

1.7 Overview of dissertation

A study of relevant literature that provides a supporting theoretical background to the research is presented in Chapter 2. Chapter 3 and 4 present the process of experimental investigation that was followed from the experimental setup to the discussion of testing results.

Chapter 3 presents an optical analysis, which characterises the solar reflector's performance by determining its intercept factor under full moon conditions. The experimental and analytical thermal analysis characterising the performance of the solar collector is presented in Chapter 4. An uncertainty analysis pertaining to the fundamental test parameters that were considered in the research is presented in Chapter 5. The research is summarised and concluded in Chapter 6.

Appendix A presents the Python code that is used to process the digital images taken during lunar flux testing to determine the intercept factor for different aperture sizes. Appendix B presents the Python code used to determine the true shape of the reflector facet concavity. Appendix C presents the calibration of the different measurement devices used in the experimental analysis of the cavity receiver. The fundamental theory behind the uncertainty analysis pertaining to the experimental parameters is presented in Appendix D.

2. Literature study

2.1 Introduction

A review of current literature will be conducted with regard to the fundamental components that are present in a CSP plant. This will provide a basis of analysis that explains the considerations that are made towards designing such plants. The study breaks down the Rankine cycle into its fundamental components and determines each component's basis of analysis with the support of literature. Particular focus is put on the concentrator and the solar receiver since both units were designed and constructed for the current study.

2.2 Solar Rankine cycle

In a solar Rankine cycle, the heat from the sun is used to heat up the working fluid that is passed through the receiver. This added energy, in the form of enthalpy change, is transformed to mechanical work as the heated working fluid is expanded through the turbine. The fundamental components of a solar Rankine cycle are presented in a flow diagram in Figure 3. The associated idealised, non-scaled temperature versus entropy diagram (T-s diagram) is also presented on the right in Figure 3 with the working fluid states illustrated to describe the processes through each component in the flow diagram.

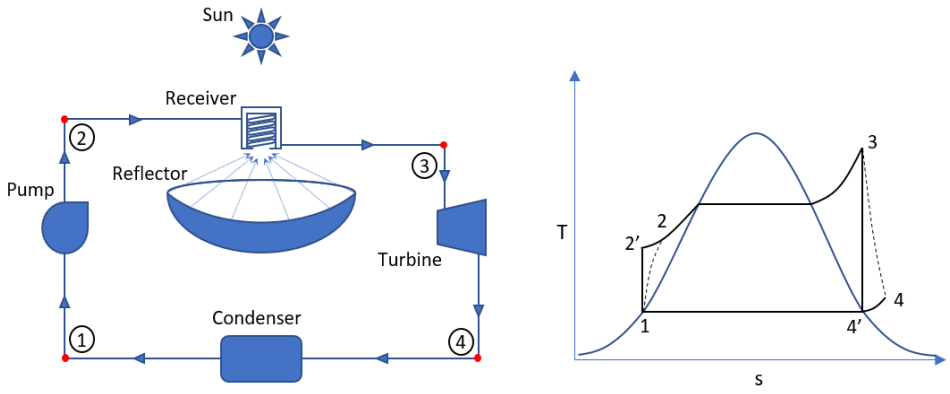

Figure 3: (left) Flow diagram of a solar Rankine cycle using a parabolic dish collector; and (right) a T-s diagram of an idealised Rankine cycle

2.3 Solar reflector

Solar reflectors, also referred to as solar concentrators, fulfil the role of directing the incident solar radiation towards a central receiver by means of a concave reflective surface. The incident aperture area of the reflector is much larger than that of the receiver, thereby concentrating the heat flux at the receiver to within a certain concentration ratio [35].

2.3.1 Reflector shape and size

There are many different types of concentrators, but the prominent ones are the parabolic trough concentrator, the linear Fresnel reflector and the central receiver tower [29]. Parabolic dishes were investigated throughout the 19th century to generate power through a steam Rankine cycle for various purposes, but the industrial implementation could never be reached since the expansion devices' conversion efficiencies were inadequate [36]. An estimate given for the respective idealised concentration ratios of these four concentrators is presented in Table 2. The sizing of the concentrator is proportional to the solar radiation that is required to be captured by the reflector.

Table 2: Generalised operating conditions of specified concentrator types [37].

Concentrator	Operating temperature	Concentration ratio	Tracking
Parabolic trough concentrator	70–400 °C	8–80	One axis
Linear Fresnel reflector	100–400 °C	8–80	One axis
Central receiver tower	500–800 °C	600–1 000	Two axis
Parabolic dish concentrator	500–1 200 °C	800–8 000	Two axis

2.3.2 Solar tracking

In CSP generation, one must consider the fact that the concentrator and receiver must be orientated towards the sun as the sun moves across the sky throughout the day. This is achieved by incorporating a tracking system into the base structure, which holds the solar collector, known as the solar tracker. The most common method of tracking the sun is through azimuth-elevation tracking. This method of tracking rotates the entire CSP plant around a vertical axis perpendicular to the horizontal plane (defined as the azimuth axis), while also rotating the dish and receiver around a horizontal axis, defined as the elevation axis. The azimuth angle produced from rotating the plant around the vertical axis is defined to be 0° facing north, 90° facing east, 180° facing south and 270° facing west. The elevation angle is defined by the angle between the focal axis of the reflector and the horizontal plane.

Using developed tracking algorithms, such as the algorithms reviewed by Lee et al. [38], and a microprocessor connected to the motors driving the azimuth-elevation rotations, a tracking error of less than 2.0° can be achieved [38, 39].

2.3.3 Rim angle

In considering the design of a conventional parabolic dish reflector, the rim angle and the dish diameter determine the concentrator's focal length. This is the length at which the aperture of the

receiver must be held from the concentrator in order to have the focal point of the concentrator coincident with the receiver aperture plane as shown in Figure 4.

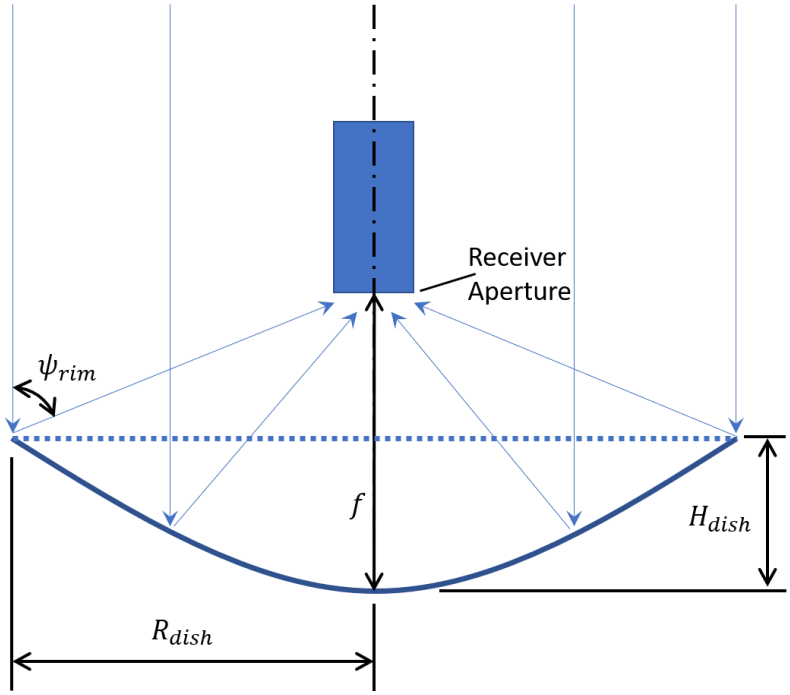

Figure 4: Fundamental dimensions of a parabolic dish shown through a cross-section

The focal length (f) is related to the rim angle (ψ_{rim}) through the dish radius (R_{dish}) according to Equation 2-1. The focal length is also related to the dish height (H_{dish}) through the dish diameter according to Equation 2-2.

$$f = \frac{R_{dish}}{2\tan\left(\frac{\psi_{rim}}{2}\right)} \tag{2-1}$$

$$H_{dish} = f - \frac{R_{dish}}{\tan(\psi_{rim})} \tag{2-2}$$

Many researchers choose a rim angle close to $\psi_{rim} = 45°$ as it is considered the theoretical optimum that will result in the greatest concentration ratio [40-43]. However, this study was conducted for a flat receiver. When considering other receiver shapes, the optimum can vary due to the geometrical characteristics of the receiver.

Fraser [44] made the argument that convection heat losses from the receiver aperture could be decreased with an increase in rim angle, based on a study conducted by Paitoonsurikarn and Lovegrove [45], since the focal length is decreased. This argument is justified through the work of Uzair [46], who performed a numerical analysis on the convection heat losses from the receiver aperture when considering both the dish and a constant wind velocity. The study showed that heat losses from

the aperture do, in fact, decrease with a decrease in focal length due to the shielding effect of the dish. This, however, decreases the intercept factor at the receiver aperture of the cavity receiver due to the optical error of the reflector. Since the incident angle at the receiver aperture is increased with a shorter focal length, the projected image at the aperture increases in size, which causes a decrease in intercept factor. More spillage occurs with a decrease in focal length. This means that less solar radiation can make it into the receiver cavity. The estimated ideal rim angle of 45° was thus considered in the current design of the new dish reflector.

2.3.4 Surface reflectivity

The reflectivity (ρ) of the surface of the concentrator determines how much energy is directed towards the receiver. It is thus a very important characteristic of the concentrator that must be considered. The reflectivities of some common materials are considered in the work of Hafez et al. [47], where the reflectivity of these materials range between values of 87 and 98%.

2.4 Solar receiver

The solar receiver performs the role of the evaporator in the conventional Rankine cycle, where the working fluid is evaporated and further heated up to a designed superheated state before it is expanded through the turbine. The combination of the solar reflector and the solar receiver is referred to as the solar collector in this research. The efficiency of the power generation cycle strongly depends on the performance of the receiver. It is thus investigated in detail in this section. The heat transfer coefficient of the working fluid is investigated through the two fundamental mechanisms of boiling (pool boiling and flow boiling). The cavity design is then investigated with regard to the heat losses that are expected to occur.

Before an investigation on heat transfer can be performed, it is important to describe the primary parameters by which heat transfer is defined. Convection heat transfer is defined through the use of a convection heat transfer coefficient ($\bar{h}$) and the dimensionless equivalent, the Nusselt number (Nu). The Nusselt number describes the relationship between the convective mechanism of the working fluid and its conduction mechanism, as shown in Equation 2-3. Empirical correlations have been formulated through research to describe heat transfer for many situations, a few of which are considered in the coming paragraphs.

$$Nu = \frac{\bar{h}L_c}{k} \tag{2-3}$$

Another important parameter that is used universally in pool boiling, as well as in continuous flow correlations, is the Prandtl number. This parameter describes the relationship between the molecular

diffusivity of momentum and the thermal diffusivity of heat within the working fluid and is presented in Equation 2-4.

$$Pr = \frac{v}{\alpha} = \frac{\mu Cp}{k} \tag{2-4}$$

2.4.1 Pool boiling

Pool boiling is considered to occur when there is no forced fluid flow from an external source such as a pump. It is important to consider the pool boiling mechanism since flow rates within the coil tubes may be so low that pool boiling dominates the flow regime and thus the heat transfer correlations may apply. Any movement of the fluid occurs due to buoyancy forces from the heated sections of fluid within the volume, as well as the rising of nucleated bubbles from the heated surface. The fundamental boiling regimes that have been determined to occur during pool boiling are natural convection boiling, nucleate boiling, transition boiling and film boiling. These regimes are described by Cengel and Ghajar [48], along with appropriate empirical heat transfer correlations.

The boiling curve for water at a pressure of 1 atm is illustrated in Figure 5, which describes the correlation of the heat transfer rate from the boiling surface to the working fluid as a function of the temperature difference between the heated surface and the fluid saturation temperature, which is referred to as the excess temperature. The shape of the curve is dependent on the material of the heated surface and the type of working fluid but is essentially independent of surface geometry [48].

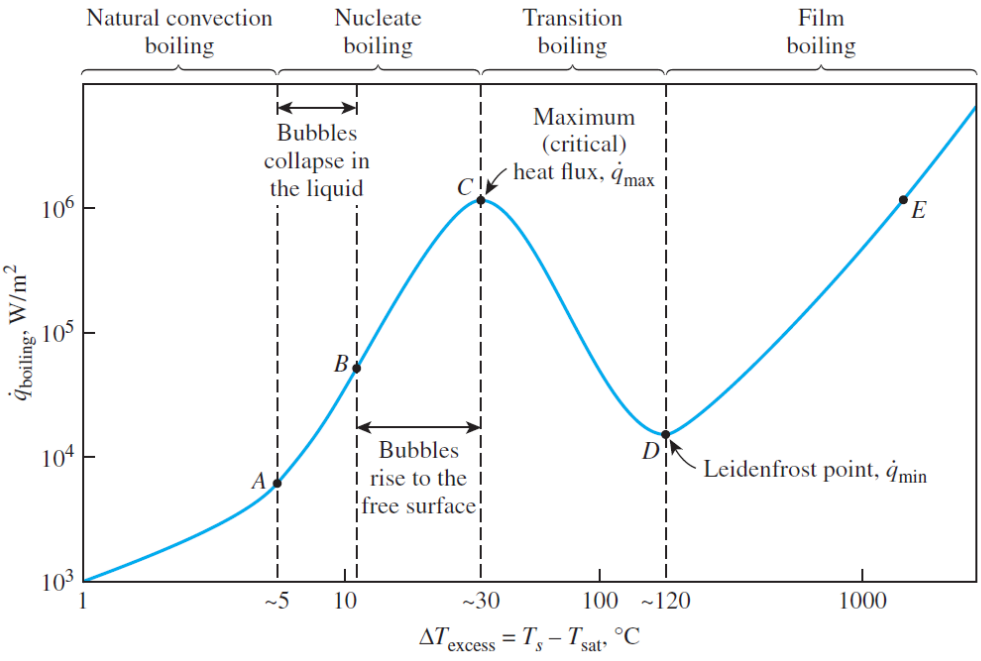

Figure 5: Boiling curve of water at a pressure of 1 atm [48]

2.4.1.1 Natural convection boiling

Nucleation of vapour bubbles only occurs after an excess temperature of roughly 5 °C is reached when pool boiling is considered in practice. Before nucleation boiling occurs, the boiling regime is dominated by natural convection boiling due to the buoyancy effect from the heated section of fluid.

Heat transfer correlations during natural convection are described through the use of the following dimensionless parameters.

$$Gr = \frac{g\beta(T_s - T_\infty)L_c^3}{v^2} \tag{2-5}$$

$$Ra = GrPr \tag{2-6}$$

$$Nu = f(Ra, Pr) \tag{2-7}$$

The Grashof number, shown in Equation 2-5, is a dimensionless parameter that describes the relationship between the buoyancy forces and the viscous forces within the working fluid. The Rayleigh number, shown in Equation 2-6, describes the relationship between the Grashof number and the Prandtl number within the working fluid. The Nusselt number considered in natural convection boiling is typically a function of the Rayleigh and Prandtl numbers associated with the fluid, as presented in Equation 2-7.

All the fluid properties are taken at film temperature, which is the average between the heating surface temperature and the bulk fluid temperature, as shown in Equation 2-8.

$$T_f = \frac{1}{2}(T_s + T_b) \tag{2-8}$$

2.4.1.2 Nucleate boiling

Nucleate boiling is described to occur for an excess temperature between 5 and 30 °C for water at 1 atm [48]. The regime is characterised by the nucleation of bubbles at the heating surface. The heat transfer rate spikes towards a peak heat flux, illustrated as point C in Figure 5.

Rohsenow [49] developed a heat flux correlation for this regime, which is given in Equation 2-9.

$$\dot{q}_{nucleate} = \mu_l h_{fg}\left[\frac{g(\rho_l - \rho_v)}{\sigma}\right]^{1/2}\left[\frac{Cp_l(T_s - T_{sat})}{C_{sf}h_{fg}Pr_l^n}\right]^3 \tag{2-9}$$

The fluid properties are evaluated at saturation temperature. The constant C_{sf} is an experimental constant that depends on the surface-fluid combination. The constant n is an experimental constant that depends on the type of working fluid. The symbol σ represents the surface tension at the liquid-vapour interface.

2.4.1.3 Transition boiling

Transition boiling is characterised by a drop in the heat transfer rate from the heating surface since most of the heating surface is covered by a thin film of expanded vapour that has an insulating effect. This regime is generally avoided since the objective of heat exchangers is to provide heat transfer at as rapid a rate as possible. As shown in the boiling curve, the regime occurs with a temperature range between 30 and 120 °C. The maximum or critical heat flux occurs at the lower temperature limit and was theoretically modelled by the work of Zuber [50]. The theoretical derivation is presented in Equation 2-10 where C_{cr} is a constant that is dependent on the heating element geometry.

$$\dot{q}_{max} = C_{cr} h_{fg} [\sigma g \rho_v^2 (\rho_l - \rho_v)]^{1/4} \tag{2-10}$$

Minimum heat flux occurs at the upper temperature limit and is defined as the Leidenfrost point. A correlation to estimate the heat transfer rate at this point was developed by Zuber [50] and is shown in Equation 2-11.

$$\dot{q}_{min} = 0.09 \rho_v h_{fg} \left[\frac{\sigma g (\rho_l - \rho_v)}{(\rho_l + \rho_v)^2} \right]^{1/4} \tag{2-11}$$

Heat exchangers are generally not designed for conditions beyond the point of maximum heat transfer (point C in Figure 5) as heating surface temperatures tend to spike towards the melting point of the surface material. This is called burnout.

2.4.1.4 Film boiling

Film boiling is characterised by the heating surface being completely covered by a thin film of expanded vapour. The regime occurs above an excess temperature of 120 °C. From the Leidenfrost point, the heat transfer rate begins to gradually rise once again.

2.4.2 Flow boiling in helical coils

Flow boiling is expected to occur in the helical coil tubes of the receiver due to the work input from the pump in the Rankine cycle. This boiling mechanism is dominated by forced convection heat transfer due to the flow of the working fluid in the cycle. In comparison to straight tubes, heat transfer in helical coils is greater due to secondary flow effects from the fluid flowing through the curved tube. These effects also extend the period before dryout occurs. Correlations to model the heat transfer rate, as well as the pressure drop in a helical coil during boiling, are investigated to aid in design.

An important term that is considered during continuous flow is the mass flux (G) of the working fluid. The mass flux of the working fluid is defined in Equation 2-12 where G_l is the mass flux of the liquid component and G_v is the mass flux of the vapour component during two-phase flow.

$$G = \frac{\dot{m}_w}{A_{cs}} = \frac{\dot{m}_l + \dot{m}_v}{A_{cs}} = G_l + G_v \tag{2-12}$$

The steam quality (x) is described by the relationship given in Equation 2-13.

$$x = \frac{G_v}{G} \tag{2-13}$$

2.4.2.1 Dimensionless parameters

It is important to describe the commonly used dimensionless parameters that help in the correlation of the heat transfer rate, as well as the pressure drop during continuous flow. The dimensionless parameters are presented as equations 2-14 to 2-19 in Table 3.

Table 3: Dimensionless parameters used during continuous flow boiling.

Dimensionless parameter	**Description**	**Relationship**	**Equation**
Reynolds number	Relates the inertial forces within the working fluid to the viscous forces.	$Re = \frac{\rho V L_c}{\mu}$	2-14
Friction factor	Also known as the Darcy-Weisbach friction factor, it relates the local wall shear stress to the mass flux moving through a pipe.	$f = \frac{8\tau_w}{\rho V_{avg}^2}$	2-15
Boiling number [51]	Relates the actual heat flux to the potential heat flux during boiling.	$Bo = \frac{\dot{q}}{G h_{fg}}$	2-16
Dean number [52]	Relates the inertial forces within a curved tube to the centrifugal forces.	$Dn = Re\sqrt{\frac{D_i}{D_{coil}}}$	2-17
Convection number [53]	A measure of the contribution between the convective boiling component and the nucleate boiling component.	$Co = \left(\frac{1-x}{x}\right)^{0.8}\left(\frac{\rho_l}{\rho_v}\right)^{0.5}$	2-18
Martinelli parameter [54]	Relates pressure drop per unit length of the vapour phase to that of the liquid phase.	$\chi = \sqrt{\frac{\left(dP/dL\right)_l}{\left(dP/dL\right)_v}}$	2-19

The work of Kakac et al. [53] describes the significance of convective boiling through the relationship provided in Table 4.

Table 4: Dominant boiling regime

Nucleate boiling	$Co > 0.65$
Convective boiling	$Co \leq 0.65$

The relationship shows the point at which convective boiling heat transfer becomes dominant in the boiling regime.

2.4.2.2 Flow regimes

For the purpose of the current study, a brief review of basic flow regimes that are expected to occur is given.

The centrifugal force occurring from fluid moving in a radial arc produces vortices inside a tube as shown in Figure 6, defined as secondary flow. These vortices were initially investigated in the work of Dean [52], who formulated a mathematical relationship between the centrifugal forces and the inertial forces of the fluid at a given cross-section of a curved tube, referred to in Equation 2-17 as the Dean number.

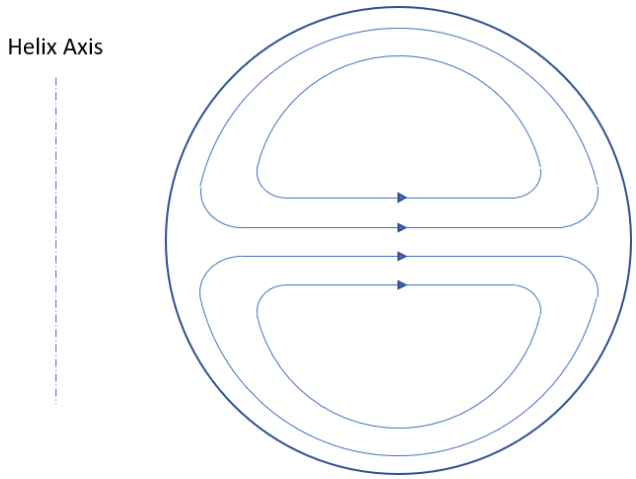

Figure 6: Idealised single-phase flow in a helical coil showing secondary flow streamlines

Early research into two-phase flow in helical coils investigated the effect of secondary flow on the film distribution in the coil tubes. Ishida [55] found that at pressures of 1 to 20 atm and high mass velocities with a fixed heat flux, the secondary flow is so dominant that liquid begins to be carried from the inner coil surface farthest from the helix axis to the inner coil surface closest to the helix axis, as shown in Figure 7C. The phenomenon is known as film inversion and is beneficial for coil evaporators used in cavity receivers since the heat transfer coefficient along the surface, which holds the bulk of the liquid film, is

much larger than at the surface where the film layer is much thinner (closer to burnout). It was even reported that film inversion occurred at low pressure and low mass fluxes, as shown in Figure 7D, which is counter-intuitive, since one would expect this condition to be dominated by centrifugal forces. Instead, the flow is dominated by gravity and the secondary flow of the vapour. It is expected that relatively large vapour flow rates would be induced in the flow to obtain this result.

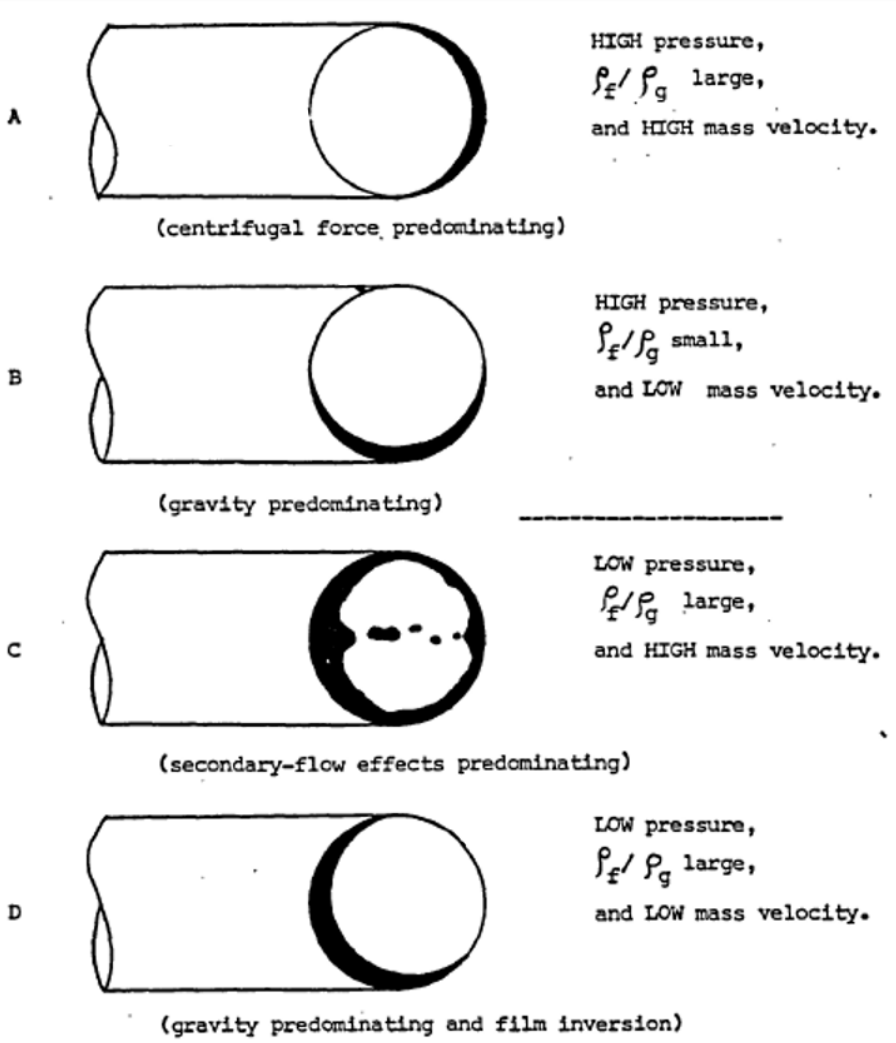

Figure 7: Film position in the cross-section of the coil tube for specific conditions [55]

The work of Zhu et al. [56] identified six flow regimes for adiabatic two-phase air-water flow, which is similar to that of straight and inclined tubes. The six regimes identified were bubbly flow, plug flow, slug flow, wavy flow, annular flow and slug annular flow. Their respective flow patterns are presented in Figure 8. The research found that stratified flow was not present, even at flow rates of 0.3 g/s. It was determined that, in order for stratified flow to occur, the gas phase would have to exert an appropriate pressure at the liquid-gas interface to overcome the gravitational influence on the liquid.

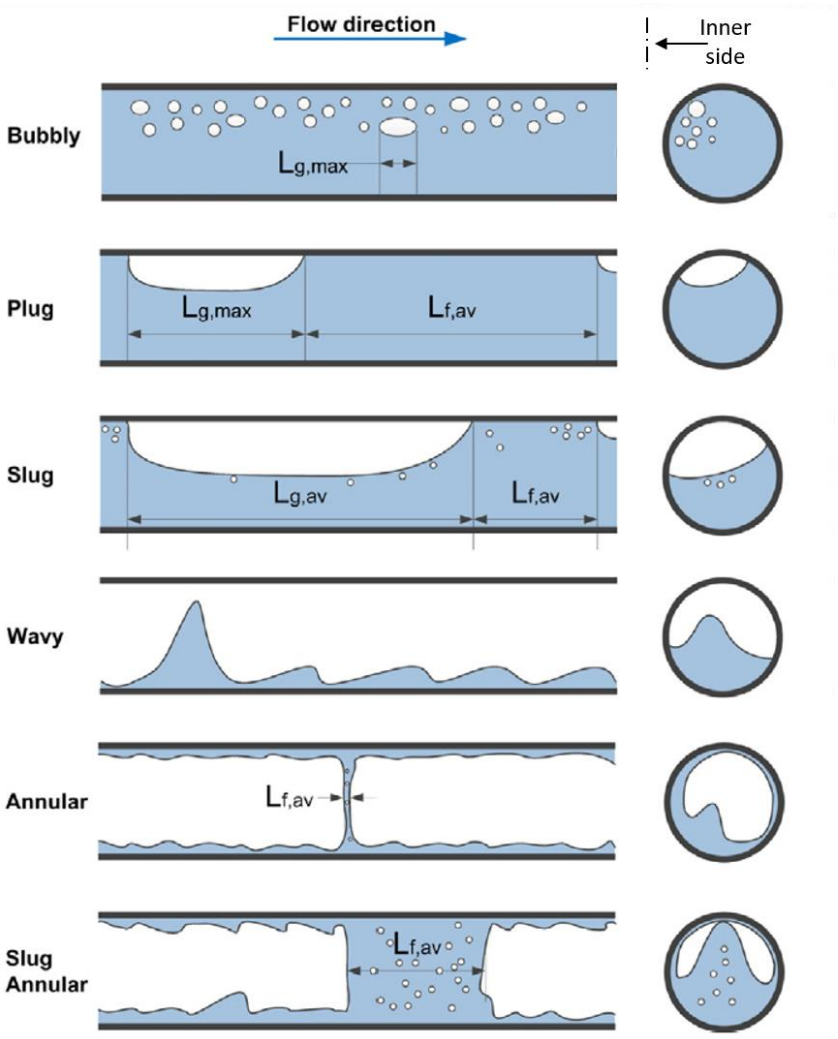

Figure 8: Flow regimes identified for two-phase flow in a helically coiled tube [56]

The work of Cui et al. [57] identified flow patterns and correlated their associated pressure drops for the flow boiling of R134a inside a micro-finned, helical coiled tube. The identified flow patterns are presented in Figure 9. It was found that the flow regime stayed within stratified flow for mass flux values less than 100 kg/m^{2}s. The coil had an outer diameter of 12.7 mm, an inner diameter of 11.2 mm, a pitch of 50 mm and a coil diameter of 185 mm. The test conditions were an evaporating pressure of 0.5–0.58 MPa, a mass flux of 61–315 kg/m^{2}s, a uniform heat flux applied to the test tube of 2.0–21.8 kW/m^2, and a vapour quality of 0.05–92%. A flow map was produced, which shows the transitions between flow regimes as a function of mass flux and vapour quality, as shown in Figure 10.

Based on the literature found on flow regimes for two-phase flow in helical coils, it is expected that bubbly flow will be the regime that occurs at the initiation of boiling inside the helical coil, which gradually moves towards plug and slug flow further along the coil length as the nucleated bubbles

accumulate. If the vapour places an appropriate pressure at the liquid-vapour interface to overcome the static pressure of the liquid, the flow may transition into stratified flow.

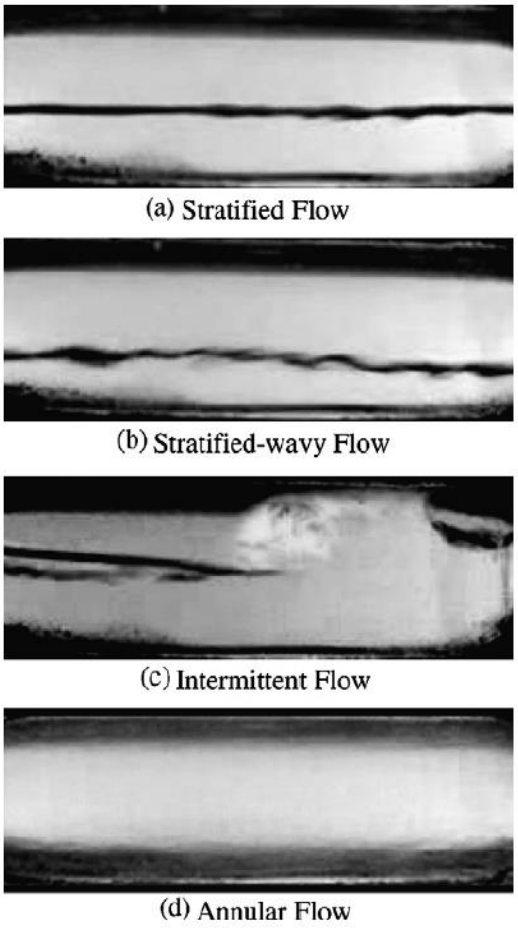

Figure 9: Flow patterns inside micro-finned, helically coiled tubes during boiling [57]

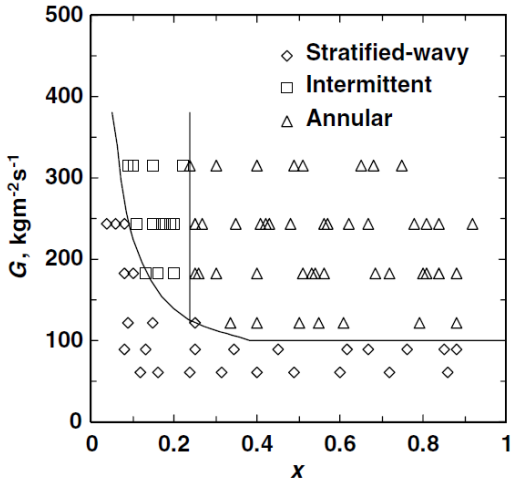

Figure 10: Flow map for boiling flow through a micro-finned helical coil as a function of mass flux and vapour quality [57]

The expansion of the liquid into gas forces the vapour to move at a faster mass flux in comparison to the flow of the liquid. As the relative velocities between the vapour and the liquid change, the secondary flow experienced by the gas moving through the helical coil tube presses the liquid against the surface of the tube, and annular flow occurs. At relatively high vapour mass fluxes, film inversion may occur, but this is not expected during practical flow boiling in helical coils since the mass flux of the steam is not expected to be fast enough to cause this phenomenon.

One conclusion can be made from this study, and that is that the flow regime is strongly dependent on the experimental setup, the working fluid considered, and the operating conditions chosen.

2.4.2.3 Dryout

Dryout, also referred to as burnout by Ishida [55], is the phenomenon where the liquid vapour film completely evaporates from the heating surface and only vapour convects the heat from the surface. This is characterised by a rise in the wall temperature, since heat is no longer efficiently transferred from the heated wall. This rise in the wall temperature could lead to the coil reaching melting point. This destruction of the coil is referred to as burnout. The phenomenon of dryout is illustrated in Figure 11. The figure shows how dryout usually initiates at the top of the coil tube and gradually increases along the tube surface towards the inner side of the helix.

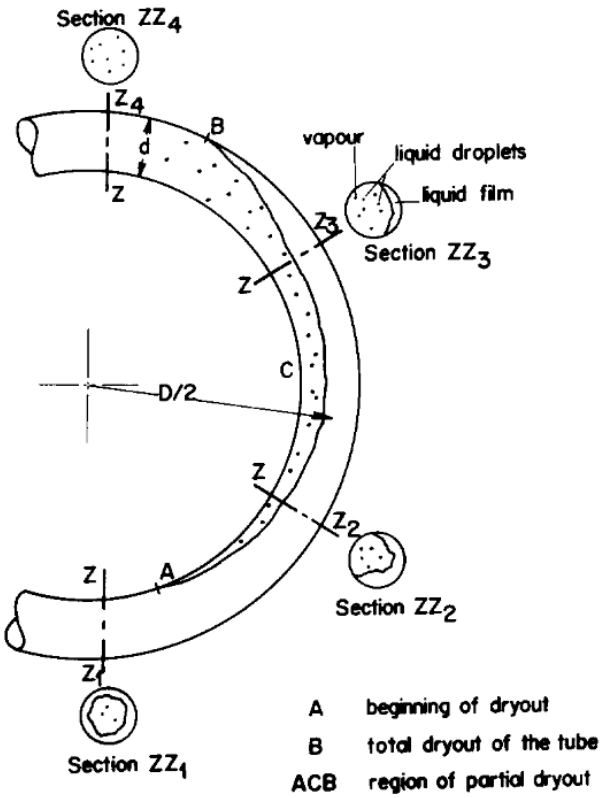

Figure 11: Dryout in a helical coil [58]

This initiation of dryout would raise the coil surface temperature, which would lead to a higher rate of boiling at the liquid surface interface, so initiation of dryout is expected to be helpful for the evaporation of the liquid. Since the objective of the receiver in the current research is to superheat water vapour, the receiver should be designed to achieve the initiation of dryout as soon as possible. Elsayed [59] showed that dryout would occur earlier along the length of the coil for larger coil diameters since the effect of centrifugal forces and secondary flow diminishes with the increase in coil diameter. It was also reported that smaller coil diameters that operate at low pressures have better heat transfer characteristics [59].

2.4.2.4 Heat transfer correlations

Over the years, many correlations have been developed to model boiling heat transfer in helically coiled tubes. The correlations that are commonly considered in coil design, as well as some lesser-known correlations that are considered to suit the estimated experimental setup and operating conditions, will be presented and discussed in this section.

One of the oldest and most well-known correlations is the Modified Chen correlation for straight tubes, formulated in the work of Owhadi et al. [60]. This is presented in equations 2-20 to 2-23. The correlation was formulated to model the boiling of water inside helically coiled tubes by considering the contributions of convective and nucleate boiling through the nucleate boiling suppression factor (B) and the convective boiling enhancement factor (F).

$$\bar{h}_i = 0.00122 \frac{k_l^{0.79} Cp_l^{0.45} \rho_l^{0.49}}{\sigma^{0.5} \mu_l^{0.29} \Delta h^{0.24} \rho_v^{0.24}} T_{sat}^{0.24} P_{sat}^{0.75} B + 0.023 Re_l^{0.8} Pr_l^{0.4} \frac{k_l}{D_i} F \tag{2-20}$$

$$\chi_{tt} = \left(\frac{1-x}{x}\right)^{0.9} \left(\frac{\rho_v}{\rho_l}\right)^{0.5} \left(\frac{\mu_l}{\mu_v}\right)^{0.1} \tag{2-21}$$

$$F = \begin{cases} 1 & \text{, for } \frac{1}{\chi_{tt}} \leq 0.1 \\ 2.35\left(\frac{1}{\chi_{tt}} + 0.213\right)^{0.736} & \text{, for } \frac{1}{\chi_{tt}} > 0.1 \end{cases} \tag{2-22}$$

$$B = \frac{1}{1 + 2.53 \times 10^{-6} F^{1.25} Re_l} \tag{2-23}$$

The Martinelli parameter for turbulent-turbulent flow (χ_{tt}), as defined in Equation 2-21, was considered in later empirical correlations to model heat transfer at certain operating conditions such as equations 2-24 and 2-25, listed in Table 5.

Table 5: Empirical correlation for the heat transfer coefficient during boiling flow in a helical coil

Correlation reference and mean error	**Correlation**	**Parameters**	**Equation**
Kozeki et al. [61] ($\pm 20\%$)	$\frac{\bar{h}_{TP}}{\bar{h}_{lo}} = 2.5\left(\frac{1}{\chi_{tt}}\right)^{0.75}$	$0 < x < 1$ $Do = 21.7\ mm$ $0.032 < Di/Dc < 0.035$ $151 < \dot{q} < 346$ $0.5 < P < 2.1\ MPa$ $161 < G < 486$	2-24
Schrock and Grossman [62] ($\pm 30\%$)	$\frac{\bar{h}_{TP}}{\bar{h}_{lo}} = 1.11\left(\frac{1}{\chi_{tt}}\right)^{0.66} + 7400Bo$	$0.1 < x < 0.9$ $Di = 14.3; 20\ mm$ $0.024 < Di/Dc < 0.034$ $70000 < \dot{q} < 180000$ $2 < P < 3.5\ MPa$ $150 < G < 850$	2-25

The liquid-only heat transfer coefficient can be calculated from the correlation of Seban and McLaughlin [63] according to the work of Zhao et al. [64], as presented in Equation 2-26.

$$Nu_{lo} = 0.0023 Re_{lo}^{0.8} \mathrm{Pr}_l^{0.4} \left[Re_{lo}^{0.05} \left(\frac{D_i}{D_c}\right)^{0.1} \right] \tag{2-26}$$

The liquid-only Reynolds number is calculated using Equation 2-27.

$$Re_{lo} = \frac{G D_h}{\mu_l} \tag{2-27}$$

The work of Cui et al. [65] formulated an empirical correlation that describes the heat transfer rate in helically coiled tubes by modifying the well-known correlation of Klimenko [66] for straight tubes to fit experimental results using an additional term containing the respective Dean number as shown in Equation 2-28. The correlation was formulated for boiling heat transfer in micro-finned helical coil tubes using R134a, so care should be taken when considering these results.

$$Nu_{TP} = 8.76 Re_m^{0.6} Pr_l^{\frac{1}{6}} \left(\frac{\rho_v}{\rho_l}\right)^{0.5} \left(\frac{k_{l,s}}{k_{l,b}}\right)^{0.09} Dn^{0.1} Co^{-0.414} \tag{2-28}$$

The number Re_m is the Reynolds number for the two-phase mixture described in Equation 2-29.

$$Re_m = \frac{\left[x\left(\frac{\rho_l}{\rho_v} - 1\right) + 1\right] G D_h}{\mu_l} \tag{2-29}$$

The hydraulic diameter (D_h) is taken as the characteristic length.

2.4.2.5 Pressure drop correlations

When considering the pressure drop in a helical coil during boiling, the fundamental term that must be considered is the pressure drop due to gravity, momentum and friction, as presented in Equation 2-30.

$$\Delta P_{tot,TP} = \Delta P_{grav,TP} + \Delta P_{acc,TP} + \Delta P_{fr,TP} \tag{2-30}$$

The pressure drop due to gravity and momentum is commonly determined through equations 2-31 and 2-32, where H_{coil} is the coil height.

$$\Delta P_{grav} = \left[\frac{gH_{coil}}{x_{out} - x_{in}}\right]\left\{\left[\frac{\ln\left(1 + x\left(\frac{\rho_l}{\rho_v} - 1\right)\right)}{\frac{1}{\rho_v} - \frac{1}{\rho_l}}\right]_{out} - \left[\frac{\ln\left(1 + x\left(\frac{\rho_l}{\rho_v} - 1\right)\right)}{\frac{1}{\rho_v} - \frac{1}{\rho_l}}\right]_{in}\right\} \tag{2-31}$$

$$\Delta P_{acc} = G^2\left\{\left[\frac{1-x}{\rho_l} + \frac{x}{\rho_v}\right]_{out} - \left[\frac{1-x}{\rho_l} + \frac{x}{\rho_v}\right]_{in}\right\} \tag{2-32}$$

The frictional pressure drop during boiling is more complicated to determine, but common practice in research is to present the friction pressure drop for two-phase flow as a function of a dimensionless multiplier, and the equivalent single-phase pressure drop as presented in Equation 2-33.

$$\Delta P_{fr,TP} = \Delta P_l \times \phi_l^2 \tag{2-33}$$

Correlations for the liquid pressure drop multiplier (ϕ_l^2) have been researched and determined through multiple studies for specific operating parameters. Some of the correlations considered to be relevant for the current study and respective parameters are presented in equations 2-34 to 2-36 in Table 6.

2.4.3 Natural convection vs forced convection

An interesting parameter to consider is the relationship between the natural convection component and the forced convection component as it defines what mode should be considered during design. The parameter that describes this relationship is the Richardson number presented in Equation 2-37. The Richardson value intervals that estimate the convection modes are presented in Table 7.

Table 6: Pressure drop multiplier correlations

Correlation reference and mean error	Correlation	Parameters	Equation
Owhadi et al. [60] ($\pm 15\%$)	$\phi_{l,tt}^2 = 1 + \frac{C}{\chi_{tt}} + \frac{1}{\chi_{tt}}$ where C is an experimentally determined constant	$0.5 < x < 1$ $Di = 12.5\ mm$ $0.024 < Di/Dc < 0.05$ $60 < \dot{q} < 256$ $P = 0.1\ MPa$ $80 < G < 315$	2-34
Zhao et al. [64] ($\pm 12\%$)	$\phi_l^2 = 1 + \left[\frac{\rho_l}{\rho_g} - 1\right]\left[0.303x^{1.63}(1 - x)^{0.885} Re_l^{0.282} + x^2\right]$	(Horizontal coil) $0.1 < x < 0.9$ $Di = 9\ mm$ $0.024 < Di/Dc < 0.034$ $70000 < \dot{q} < 180000$ $2 < P < 3.5\ MPa$ $150 < G < 850$	2-35
Cioncolini et al. [67] ($\pm 16.3\%$)	$\phi_l^2 = \left[1 + \frac{C}{\chi_{tt}} + \frac{1}{\chi_{tt}}\right]\left[1 + 0.0044\left(\frac{\dot{q}}{G}\right)^{0.7}\right]$ where C is an experimentally determined constant	$0 < x < 0.9$ $Di = 4.03; 4.98\ mm$ $0.011 < Di/Dc < 0.038$ $50 < \dot{q} < 440$ $120 < P < 660\ kPa$ $290 < G < 690$	2-36

Table 7: Dominating convection modes [48]

Convection mode	Relationship
Forced convection	$Ri < 0.1$
Both convection modes	$0.1 < Ri < 10$
Natural convection	$Ri > 10$

$$Ri = \frac{Gr}{Re^2} \tag{2-37}$$

2.4.4 Convection heat loss from a cylindrical receiver aperture

The convection heat loss through the aperture of an open cylindrical cavity is one of the prominent losses that occurs during operation and is also one of the more difficult modes of heat transfer to model. Natural convection heat loss from a cylindrical aperture has been studied and reported on quite extensively, but little progress has been made in modelling forced convection heat loss due to the wind. Prominent correlations that are considered for natural convection heat loss in the current study are presented in Table 8.

Table 8: Nusselt number correlation for natural convection heat loss through a circular aperture on a cylindrical cavity

Model and conditions	Correlation	Equation
Koenig and Marvin [68] $550\ ℃ \leq T_s \leq 900\ ℃$ $0° \leq \theta \leq 90°$	$Nu_{natural} = 0.52\vartheta \left(\frac{D_{ap}}{D_{cav}}\right)^{1.75} (GrPr)^{1/4}$ where: $\vartheta = \cos(\theta)^{3.2} \quad 0° \leq \theta \leq 45°$ $\vartheta = 0.707\cos(\theta)^{2.2} \quad 45° \leq \theta \leq 90°$ $L_c = D_{ap}\left(\frac{\sqrt{2}}{2}\right)$ $T_{prop} = \frac{11}{16}T_s + \frac{3}{16}T_\infty$	2-38 2-39 2-40
Stine and McDonald [43] $0° \leq \theta \leq 90°$	$Nu_{natural} = 0.088Gr^{1/3}\left(\frac{T_s}{T_\infty}\right)^{0.18} \cos^{2.47}(\theta)\left(\frac{D_{ap}}{L_c}\right)^{s}$ where: $s = 1.12 - 0.98\left(\frac{D_{ap}}{L_c}\right)$ $L_c = D_{cav,i}$ $T_{prop} = T_\infty$	2-41 2-42

The cavity tilt angle (θ) is the angle between the normal aperture and the horizontal plane, also referred to as the elevation angle in the current research. When the cavity aperture is facing downwards, the tilt angle is 90°, and when the cavity is concentric along the horizontal plane, the tilt angle is 0°.

Many numerical studies show that side-on wind, parallel to the receiver aperture, results in the greatest heat loss regardless of the receiver tilt angle [46, 69, 70]. Studies show that wind effects on the forced convection heat loss can result in an increase of three to four times that of natural convection if a wind-skirt is not used [71, 72].

If a wind skirt is used, the forced convection heat loss is estimated to be twice that of natural convection heat loss at wind speeds below 4.5 m/s [72]. A crude correlation to side-on forced convection heat loss was formulated in the work of Ma [71], where the heat loss was simply a function of the wind velocity as presented in Equation 2-43.

$$\bar{h}_{forced} = 0.1967V_{wind}^{1.849} \tag{2-43}$$

Ma [71] further suggested that the natural and forced convection heat losses can simply be added together for the condition of side-on wind flow as presented in Equation 2-44.

$$\bar{h}_{conv} = \bar{h}_{forced} + \bar{h}_{natural} \quad (2\text{-}44)$$

2.5 Expander

It was estimated that an appropriate design pressure to work with is 6 bar as this would allow an expansion ratio of roughly 6 if the expansion device expands the fluid to a low-pressure state close to atmospheric pressure. An expansion ratio of 6 was estimated to encompass the most optimal isentropic efficiencies of common expansion devices.

A brief investigation of previous work is performed to justify this estimation and obtain a basic understanding of the types of expansion devices that could be considered along with an improved estimate of expected operating conditions. Since the primary objective is to optimise the design of the solar receiver, it is relevant to consider the operating boundary conditions of the surrounding units within the cycle and, preferably, to determine an optimum set of operating conditions that suit the entire Rankine cycle and not just the evaporator.

Quoilin et al. [73] reviewed the prospects of three of the most commonly used expansion devices in organic Rankine cycles in industry. These are the axial turbine, the radial turbine and the screw expander. The scroll expander was also considered as a promising emerging expansion device for micropower-generation Rankine cycles. Organic Rankine cycles were discretised into five common applications according to the evaporating temperature of the working fluid, listed in Table 9. After considering the operating maps for the expansion devices with regard to a selection of organic working fluids (excluding steam), an estimated power range was developed. This is presented in Figure 12.

From the analysis, it is evident that scroll expanders could suit the low output power expected from the current study if organic working fluids are considered, but commercial scroll expanders are generally modified from the scroll compressors used in refrigeration and have a peak operating temperature of roughly 130 °C according to the study of Quoilin et al. [73]. This is not ideal since the preliminary target temperature presented in Table 1 is 400 °C.

A recent study by Pethurajan et al. [74] reviewed the appropriateness of certain expansion devices in common organic Rankine applications, which also included steam as a working fluid. The expansion devices reviewed were the radial-inflow turbine, the scroll expander, the screw expander and the rotary vane expander. The estimated operating conditions for each expansion device, along with their respective advantages and disadvantages, were tabulated and are presented in Table 10. In this study,

the rotary van expander is introduced as a promising device for micro-power generation applications. This includes those with high inlet temperatures. However, a highlighted disadvantage of both the scroll expander and the rotary vane expander is the lubrication requirement, which suggests high maintenance requirements.

Table 9: Common applications for organic Rankine cycles [73]

Organic Rankine cycle application	**Evaporation temperature**
High-temperature biomass or solar plant (CHP)	~280 ℃
High-temperature waste heat recovery (WHR)	~250 ℃
Medium-temperature waste heat recovery (WHR)	~170 ℃
Low-temperature solar plant (solar)	~120 ℃
Low-temperature geothermal plant (geoth)	~80 ℃

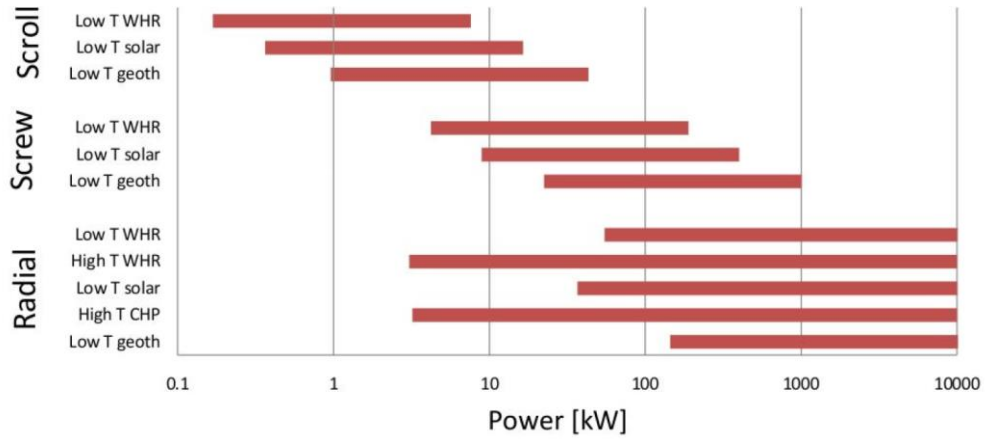

Figure 12: Applicable power range for the expansion devices [73]

Table 10: Estimated operating conditions for the considered turbines [74]

Type	Capacity range (kW)	Rotate speed (rpm)	Cost	Advantages	Disadvantages
Radial-inflow turbine	50–500	8000–80,000	High	Lightweight, with high efficiency	Cannot bear two-phase
Scroll Expander	1–10	< 6000	Low	High efficiency, lightweight, low rotating speed and tolerable two-phase	Lubrication and modification requirement
Screw Expander	15–200	< 6000	Medium	Tolerable two-phase, low rotate speed and high efficiency	Lubrication requirement
Rotary vane expander	1–10	< 6000	Low	Tolerable two-phase, torque stable, simple structure, low cost, and noise	Lubrication requirement and low capacity

Imran et al. [75] performed a detailed study on expander selection for micro-power generation. The study reviewed multiple sources and tabulated the respective operating conditions and performance of the considered expanders using different working fluids. A summary of the relevant works is presented in Table 11.

Table 11: Performance and operating conditions of investigated expanders [75]

Reference	Working fluid	Isentropic efficiency (%)	Power output (kW)	Expander speed (RPM)	Inlet temperature (°C)	Inlet pressure (MPa)	Pressure ratio (-)
Vane expander							
[76]	R113	40–50	0.6–1.4	1 500–4 000	105–112	0.45–0.55	1.7–2.2
[77]	R123	40–71	0.8-2.2	1 500–3 600	120–131	0.4–0.9	2.24–4.25
[78]	Isopentane	30–50	0.015–0.09	1 300–2 700	53–72	0.22–0.32	2.3–3.8
Screw expander							
[79]	Steam	22–45	200–800	2 500–3 333	177	0.3–1.4	-
[80]	R123	63–73	2–10.2	800–2 600	120–140	0.1–1.2	2.5–4.5
[81]	R245fa	55–70	3.5–5.2	800–1 200	-	0.4–1.1	2.7–6.54
Piston expander							
[82]	Steam	41–48	2.1–9	90e3–120e3	380	3.2	-
[83]	R245fa	35–43.3	0.025–0.35	600–800	75–90	0.6–0.85	2.0–4.5
[84]	CO_2	40–60	0.3–0.427	900–1 248	35	9	2.26–2.65
Scroll expander							
[85]	Steam	34	10–12	1 000–1 400	139–145	1–1.38	-
[86]	Steam	40–48	0.2–0.45	1 200–3 000	130–180	0.3–0.5	3–5
[87]	R123	-	0.11–0.645	300–1 300	64–168	0.3–1.1	2–8
[88]	R134a	55–77	0.28–0.835	2 005–3 670	123–133	1.1–1.8	2.65–4.84

The choice of the type of expander is difficult since there are many different types of commercial expanders available with a wide range of associated operating conditions. However, from the target operating conditions presented in Table 1, an expander would have to operate with mass flow rates as low as 0.3 g/s and inlet temperatures ranging from an estimated 150 °C to 400 °C. It would also have to be able to handle fluid in two phases if the receiver does not fully evaporate the working fluid.

This narrows the expansion devices down to a select few. It is evident from Table 11 that promising results are shown for scroll expanders with regard to their ability to work with superheated steam, but the limitations still apply with regard to their ability to efficiently expand high-temperature steam at low flow rates, as well as their maintenance requirements. A self-lubricating scroll expander could possibly be considered to extend maintenance intervals.

Axial and radial turbines did not really feature due to their inability to operate efficiently at low power outputs and handle two-phase flow, but steady progress is being made in the development of micro-steam generation turbines. An example of this is the 1.5 kW steam turbine, developed and manufactured in The Netherlands by Green Turbine™. The 1.5 kW turbine was being sold for £5 550 on 5 November 2019. It has an operating fluid inlet temperature in the range of 200 to 220 °C and an operating inlet pressure of 5.2 bar. The pressure drop is reportedly 5.1 bar and the designed steam consumption is 5 g/s [89].

2.6 Pump

For the current research, no study will be performed on pump selection since the experimental model described in Chapter 4 has no need for a pump and it is common practice to simply size the pump after the rest of the Rankine cycle has been designed.

2.7 Condenser

For the current research, no research will be performed on the types of condensers present as this is not considered the focus of the current study.

2.8 Conclusion

A detailed investigation of supporting literature pertaining to the research topic was conducted. The solar thermal Rankine cycle with direct steam generation was broken down into its primary components, and relevant research pertaining to each component was presented and discussed. It was determined that the solar collector, the solar receiver and the steam turbine were the most important components in this research, and the complexities associated with each component were investigated extensively.

It was determined that a 45° rim angle and the required captured solar radiation were the two primary design conditions that needed to be considered in the construction of a solar reflector. Different turbine technologies were investigated, and their associated performances were compared with regard to generating small-scale power generation. It was determined that scroll turbines had the highest potential, with the only limitation being the low operating temperatures.

The flow through the receiver coils was studied extensively, and important correlations of boiling heat transfer and pressure drop through the helical coils were presented. One of the important outcomes of this literature review is that boiling flow through helical coils is underdefined, particularly with regard to heat transfer through non-uniform incident heat flux on the coils. Any methods used to design such coils are crude approximations at best. The two-phase boiling flow regimes through the receiver coil have been studied extensively and can be approximated more easily in the experimental analysis.

3. Optical analysis

3.1 Introduction

A new modular dish reflector was developed at the University of Pretoria by a fellow postgraduate student, Mr Casey Roosendaal. It comprised multiple dish facets that could be adjusted independently of one another. Each facet comprised a 0.2 mm Mylar sheet membrane, stretched and sealed over the elliptical rim of an off-the-shelf television satellite dish, forming a narrow cavity in which a vacuum could be drawn to pull the Mylar sheet into a concave shape. An illustration of a single dish facet is presented in Figure 13.

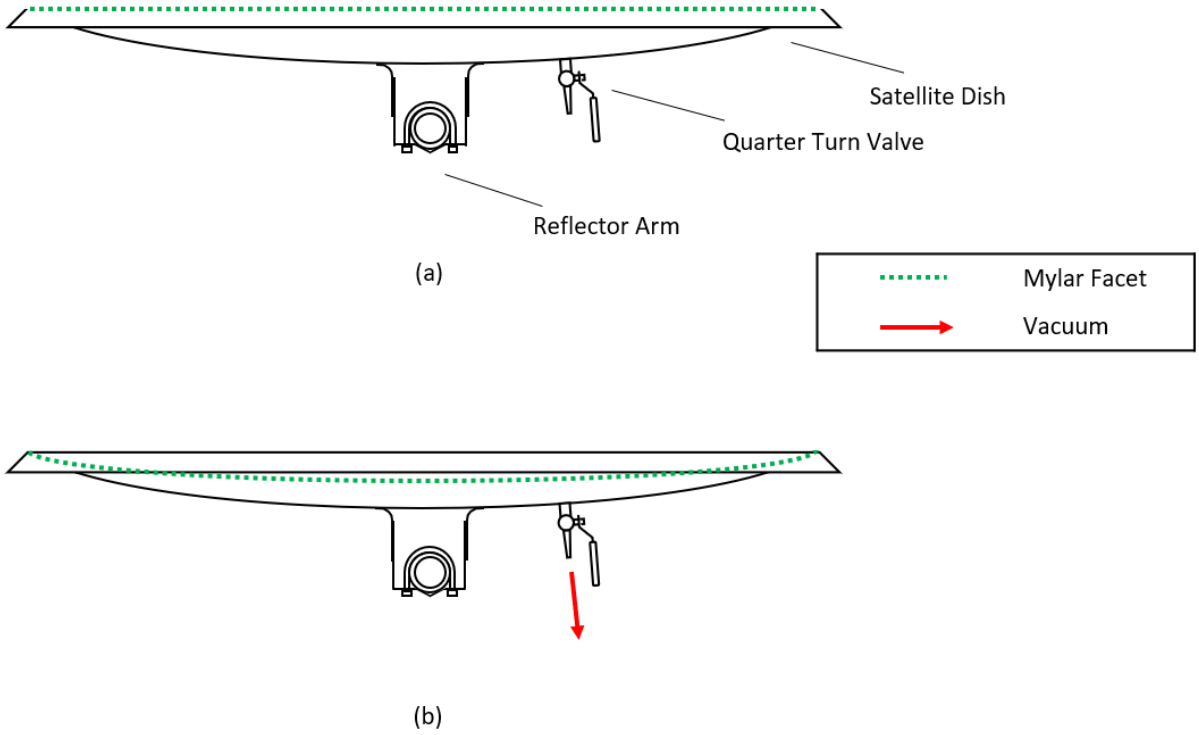

Figure 13: Illustration of a single dish facet: (a) in non-vacuum state; and (b) in a vacuum state

Conventional parabolic dishes were determined to be inappropriate for the current research since such dishes are not manufactured locally and importing these dishes incur costs that do not contribute to the feasibility of the research. In addition, the conventional design of a parabolic dish does not allow for the parameterisation of the dish's rim angle and thus the dish's focal length to suit a given receiver geometry. The new dish design could easily be manufactured in-house, using locally sourced and affordable materials. The reflector facets of the dish provided modularity to the design in that they could be adjusted separately from one another to obtain an optimum intercept factor at the receiver aperture, while allowing for the adjustment of the reflector's focal length.

With this new design, more freedom is allowed in research since the design of the receiver's coil shape is not dependent on the dish's shape anymore due to the reflector's modularity. One may simply use an existing receiver design that has been optimised for certain flow and heat flux conditions and then adjust the reflector's shape to accommodate such conditions. For these reasons, the reflector design was incorporated into the current research, in collaboration with Mr Roosendaal.

This section presents the optical analysis that was performed on the new dish design. It is important to characterise the performance of the reflector before running solar tests on the entire collector as the results can be used to aid the analysis of the solar receiver. The solar flux distribution that is projected onto the aperture plane from the reflector must be determined to calculate the intercept factor and the maximum concentration ratio at the experimental aperture. This was achieved by first determining the reflectivity of the Mylar facets through UV/VIS spectroscopy. The shape of the facet concavity that occurs during the vacuum state was then investigated through a photogrammetry analysis. A lunar flux mapping analysis was conducted to determine normalised flux distribution on the aperture plane. From this, the intercept factor was determined as a function of aperture size. Using the results of the UV/VIS spectroscopy and the lunar flux mapping analysis, the peak concentration ratio and the solar flux distribution at the aperture were determined.

3.2 UV/VIS spectroscopy analysis

In order to determine how much radiation is reflected towards the focal point of the dish reflector, the spectral reflectivity of the Mylar facets was determined. This was done using a UV/VIS spectrometry analysis conducted with the assistance of Mr Roosendaal and under the supervision of Dr Radhakrishnan at the University of Pretoria. The UV/VIS spectrometer used was a CARY 100 Bio [90]. A spectrometer has three primary components: the light source, the monochromator and the detector. The monochromator splits the light from the light source into discretised wavelengths using diffraction, and the detector measures the intensities of the discretised light through a voltage response [91].

The analysis measured the transmissivity and absorption of a clean Mylar sample for wavelengths varying from 200 to 850 nm. The results are plotted in Figure 14. Based on the resulting trend and the guidance given by Dr Radhakrishnan, the optical response could only be measured for wavelengths above 330 nm. This means that a spectral reflectivity could be determined for a waveband within the range of 330 to 850 nm. It is important to determine how much of the total solar irradiance this analysis encompassed, and to calculate an effective spectral reflectivity based on the weighted average within the waveband that was analysed.

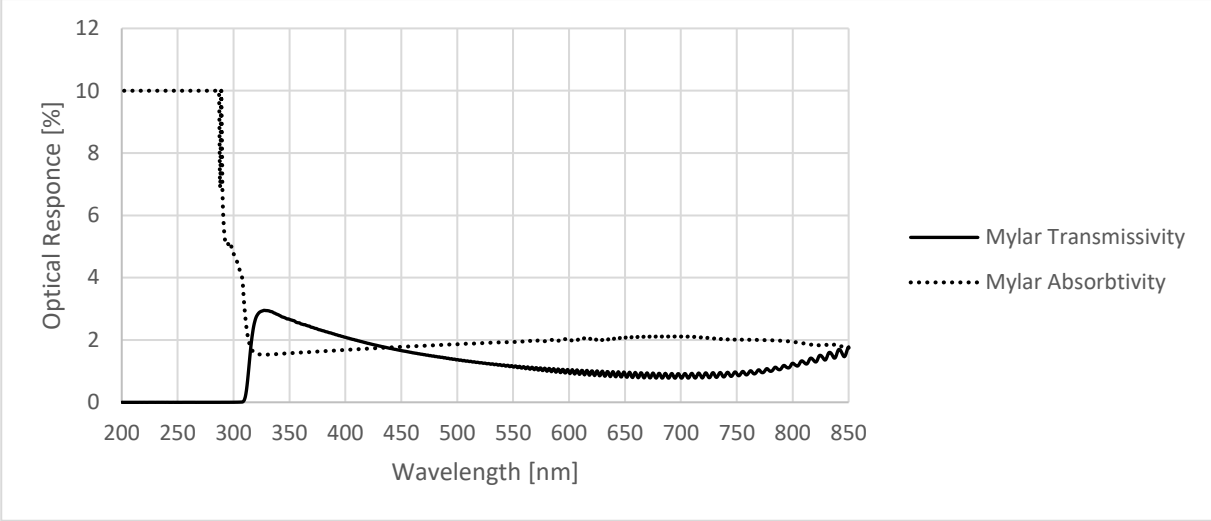

Figure 14: Transmissivity and absorptivity results for a clean Mylar sample for the UV/VIS spectroscopy test

Using the spectral Simple Model for Atmospheric Radiation Transfer of Sunshine (SMARTS2) radiation model [92], a standard DNI spectrum was generated and used as a reference spectrum, as presented in Figure 15. The reference spectrum was generated according to the ASTM G173-03(2012) [93] standard for a direct normal spectral irradiance at an air mass of 1.5. Solar radiation encompasses a waveband of 300 to 3 000 nm [48]. By summating the discretised spectral irradiance values (I_{λ_i}) and multiplying them by their respective wavebands in increments of $\Delta\lambda = 1\ nm$, the DNI over the entire solar spectrum was calculated to be 886.16 W/m^2. Using Equation 3-1 and the reference DNI spectrum in Figure 15, it was determined that the UV/VIS spectroscopy analysis could only account for 62% of the total direct spectrum. However, the visible light spectrum, with a waveband of 400 to 760 nm, was encompassed in the spectroscopy analysis and accounted for 50% of the total direct spectrum. Thus, the spectral reflectivity of the Mylar sheet for visible light could be determined. The reflectivity can be used in the analysis of the lunar flux testing since flux mapping relies on the visible spectrum to capture the illumination flux distribution on the target surface.

$$Direct\ spectrum\ represented = \frac{\sum_{\lambda_1}^{\lambda_2} I_{\lambda_i}\,\Delta\lambda}{\sum_{solar} I_{\lambda_i}\Delta\lambda} \tag{3-1}$$

The spectral optical properties of a material at a given wavelength are broken up into three components: absorptivity, reflectivity and transmissivity, as presented in Equation 3-2.

$$1 = \alpha_{\lambda_i} + \rho_{\lambda_i} + \tau_{\lambda_i} \tag{3-2}$$

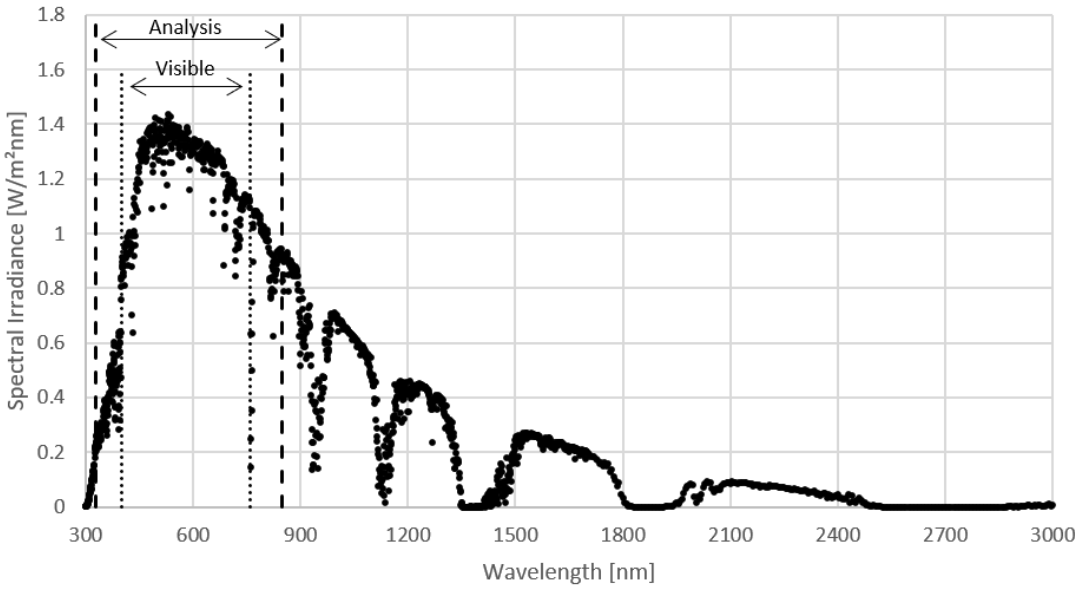

Figure 15: Reference DNI solar spectrum generated using the SMARTS2 model [92]

Spectral reflectivity within a given waveband is determined by calculating the discretised reflectivity values for each wavelength using Equation 3-2, and then multiplying these values by their respective weightings. The weighted reflectivity values are then summed to form a weighted average, which is the spectral reflectivity within the given waveband, as shown in Equation 3-3.

$$\rho_{\lambda} = \frac{\sum_{\lambda_1}^{\lambda_2} \rho_{\lambda_i} I_{\lambda_i} \Delta\lambda}{\sum_{solar} I_{\lambda_i} \Delta\lambda} \tag{3-3}$$

The spectral reflectivity for the spectrometry analysis spectrum and the visible spectrum was calculated to be 96.88 and 96.82%, respectively. It is interesting to note that even though a larger waveband was considered in the spectrometry analysis, the reflectivity of the spectrometry waveband and that of the visible waveband only differed by 0.05%. It is also important to note that the spectrometry analysis was performed on a clean Mylar sample that had not been weathered. However, the lunar flux testing was performed using reflector facets that had already been used in multiple tests prior to this one for approximately two months. The study of Stine and Harrigan [42] showed that the reflectivity of the reflector material decreases with time due to exposure to weather. To account for the weathering of the Mylar sheets, it is approximated that the spectral reflectivity of the dish facets varied between 90 and 97% during testing. This should be accounted for in the uncertainty analysis. However, a reflectivity of 97% is considered as the reflectivity of the experimental dish reflector in the current research.

3.3 Photogrammetry analysis

In order to determine the shape of the elliptical facets on the solar reflector, a digital photogrammetry analysis was performed with the assistance of Mr Leandrew Pestana and under the supervision of Mr George Breitenbach using GOM's ARAMIS Adjustable 4M System. This was done to better estimate the true shape of the concavity of the Mylar sheet under a vacuum. The surface could then be modelled numerically to compare it with the results of the lunar flux mapping analysis. The ARAMIS system is primarily used to measure deformations in a material by determining the relative displacements of certain identified features between two camera shots and transforming them into relative cartesian coordinates. The first camera shot is taken of the initial state of the material and the second is taken of the deformed material [94]. The cameras used in the GOM ARAMIS system are able to take photos at a quality of 4-megapixels and at a rate of 60 frames per seconds. The testing was carried out at camera settings of 4-megapixel quality and 1 frame per second.

Multiple place markers were positioned across the surface of the reflector facet, as well as on a position reference point, and photographs were taken of the facet to gauge the relative position of these place markers in non-vacuum (flat) and vacuum (concave) conditions. The place markers were round, white adhesive polymer stickers which were 15 mm in diameter and had a 3 mm black border around the circumference of the sticker to aid in contrast. They were positioned in a random pattern on the Mylar sheet, shown in Figure 16. They were also placed at position reference points that extended from the side of the facet. The position reference points were solid structures that would not move with the Mylar membrane as a vacuum was formed within the facet cavity. They served as position calibration markers to mitigate errors occurring from the unintentional movement of the photogrammetry cameras.

A self-developed Python code (see Appendix B) was used to read the cartesian coordinates and transform the shape to the respective origins of the cartesian plane. This was done by obtaining three place markers positioned along the rim of the facet and determining the transformations required to align the normal unit of the displacement vectors of the place markers to be parallel to the z-axis. This was achieved using a three-dimensional (3D) transformation matrix and the Nelder-Mead optimisation algorithm [95].

In order to estimate the true shape of the Mylar sheet under a vacuum condition, two 3D surfaces were investigated by fitting them to the cartesian coordinates (x, y and z) from the photogrammetry analysis. These surfaces were elliptical paraboloid and hemi-ellipsoid.

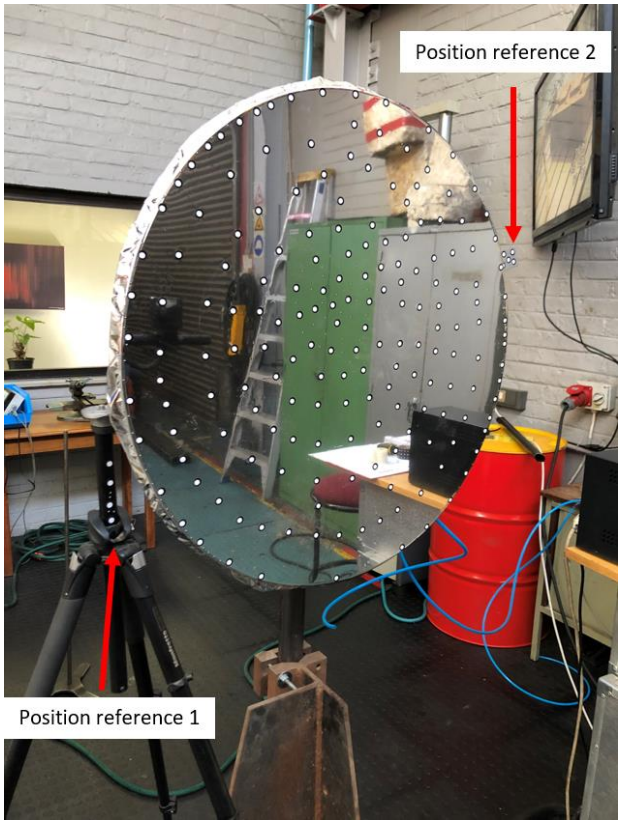

Figure 16: Position marker layout and identification during testing

Their respective surface equations are presented in equations 3-4 and 3-5. For the two surfaces, the a-coefficients define the shape of the surface, while the b-coefficients define the location of the surface in the cartesian system.

Elliptical paraboloid:

$$z(x,y) = \frac{(x+b_1)^{\,2}}{a_1^2} + \frac{(y+b_2)^2}{a_2^2} - b_3 \tag{3-4}$$

Hemi-ellipsoid:

$$z(x,y) = a_3\sqrt{1 - \frac{(x+b_1)^2}{a_1^2} - \frac{(y+b_2)^2}{a_2^2}} - b_3 \tag{3-5}$$

The root mean square (RMS) was applied to the errors between the photogrammetry coordinates and each fitted surface and minimised by adjusting the equation coefficients using the COBYLA optimisation algorithm [96]. An illustration of the resulting surface fit of the hemi-ellipsoid to the photogrammetry coordinates is presented in a surface plot in Figure 17. Since the surface fit of the elliptical paraboloid is effectively indistinguishable from that of the hemi-ellipsoid, the surface plot is not presented in the research. Scaling in the illustration is magnified in the z-direction in order to observe the shape of the surface and photogrammetry coordinates. This means that the errors are also magnified. They are apparent around the rim of the dish.

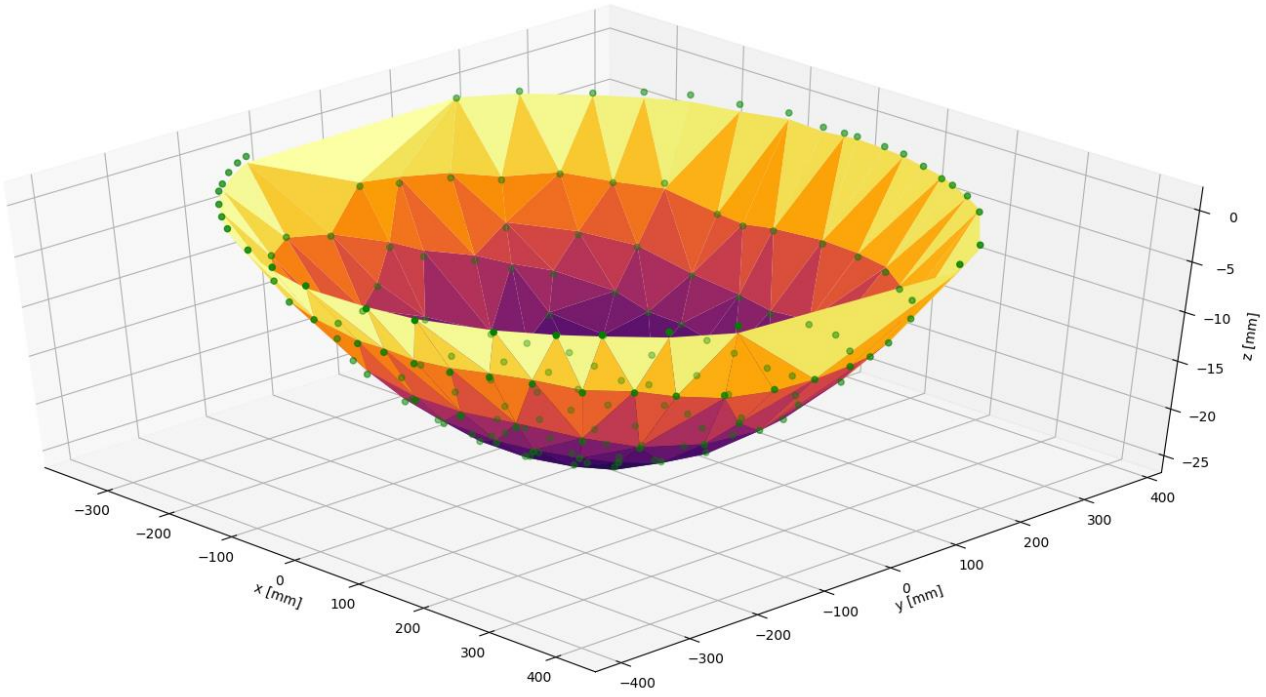

Figure 17: Surface fit of the hemi-ellipsoid to the photogrammetry coordinates

As shown in Figure 18a and 18b, the RMS error, used as the objective function, converged after three iterations for the elliptical paraboloid fit and after approximately 150 iterations for the hemi-ellipsoid fit. The RMS error converged to 27.34 x 10^{-2} mm for the elliptical paraboloid and 24.07 x 10^{-2} mm for the hemi-ellipsoid. When analysing the resulting error contour plots in Figure 17c and 17d, it is evident that both surfaces fit the photogrammetry coordinates in a comparable manner. However, the hemi-ellipsoid can be observed to fit the coordinates with slightly less error, as shown by the maximum and minimum error values given in the colour bars and in the converged RMS errors. The error was calculated by determining the difference in the z-coordinates between the photogrammetry coordinates and the fitted curves.

The surface fits carry particular errors along the rim of the facet and at coordinate (x, y) = (0, 100). An error of approximately -1 mm is observable along the rim. This means that the z-coordinates for the fitted curves are larger than the z-coordinates of the actual rim of the facet. This is believed to have occurred due to the positioning of the markers along the rim. Since the rim is effectively a solid, supporting frame, the position references will not change as the vacuum is pulled and will therefore not describe the shape of the concavity appropriately. This inaccuracy should be addressed in later research. The error that occurs at coordinate (x, y) = (0, 100), is believed to be due to plastic deformation in the facet from the Mylar sheet coming into contact with the insert of the quarter-turn valve at the base of the satellite dish (see Figure 13) prior to testing.

The plastic deformation causes a concave dimple in the sheet from the vacuum. Thus, the z-coordinates of the fitted surfaces are larger than those of the photogrammetry coordinates at this point. These errors contribute to the accuracy of the surface fit, but, for the majority of the fit, it is apparent that the shape of the concavity that occurs from a thin sheet being pulled over an elliptical rim by a vacuum is best described as being hemi-ellipsoidal.

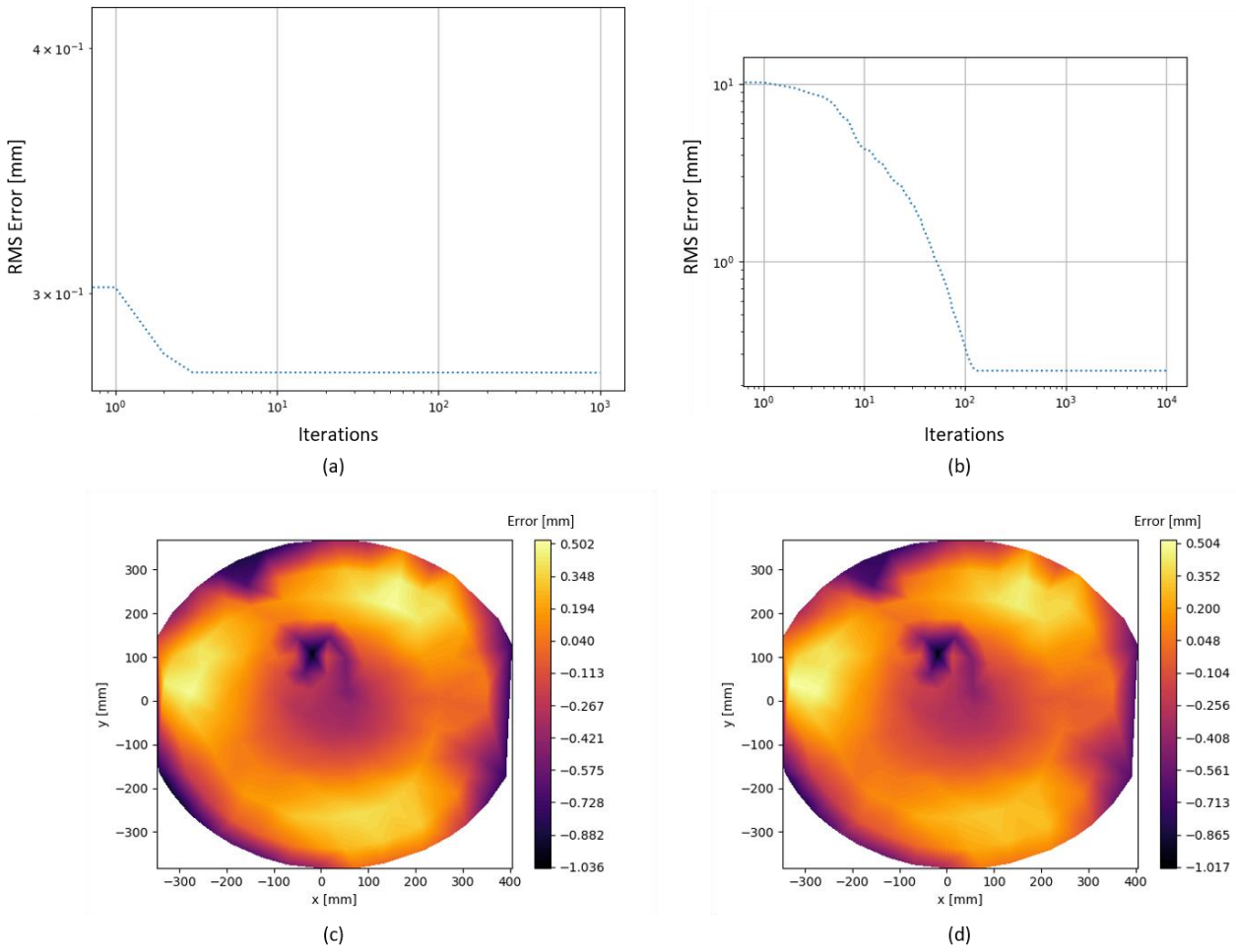

Figure 18: Iterations to convergence and resulting error contour plot for the fit of the elliptical paraboloid (a) and (c) and the hemi-ellipsoid (b) and (d)

The resulting equation coefficients for the elliptical paraboloid are presented in Table 12. Similarly, the resulting equation coefficients for the hemi-ellipsoid are presented in Table 13. These coefficients should be used as a means of comparison rather than simply modelling the resulting equation in the numerical analysis. The hemi-ellipsoidal surface should rather be modelled from the given rim dimensions and the target focal length.

Table 12: Resulting coefficients of the fitted elliptical paraboloid

Coefficients	Value
a_1	82.18
a_2	76.75
b_1	26.64
b_2	-5.60
b_3	-24.97

Table 13: Resulting coefficients of the fitted hemi-ellipsoid

Coefficients	Value
a_1	1438.07
a_2	1345.85
a_3	-602.65
b_1	26.74
b_2	-5.72
b_3	577.73

3.4 Lunar flux mapping

A lunar flux mapping analysis was carried out to determine the optical performance of the solar collector. Based on the results of the lunar flux mapping, an optical analysis was performed on the solar receiver to determine the intercept factor at the aperture for varied aperture sizes. The size of the aperture of the receiver cavity is important as it determines the amount of solar radiation that can pass through into the receiver. It also influences the heat loss from the receiver, such as radiation and convective heat loss through the aperture. Using the normalised flux map, the dish reflectivity determined in Section 3.2, and a theoretical solar DNI, a scaled solar flux distribution was produced. The solar flux map was used to show how the peak solar concentration ratio at the target surface could be determined.

Many methods have been investigated to determine the solar flux distribution on a target surface positioned at the focal point of a CSP plant. The methods are broadly classified as direct or indirect techniques. Direct techniques involve the direct measurement of the solar radiation flux using sensors distributed throughout the target surface or moved over the target surface during capturing [97-99]. Complicated and costly equipment such as calorimeters and flux gauges are typically used as the sensors in direct measurement techniques [98-100]. Often, a cooling system is required in order to preserve the sensors when exposed to high radiation heat flux [101]. Indirect methods do not directly measure the radiation heat flux distribution on the target surface, but rather the radiation reflected off of the target surface. This is generally performed using a CCD (charge coupled device) camera and a Lambertian target surface in photographic flux mapping (PHLUX). The camera captures the diffuse

light flux distribution reflected off the target surface, after which the pixel data is scaled to represent the solar radiation flux distribution at the target surface.

The scaling is achieved through multiple methods. Often, one or two radiation flux measurement sensors are placed on the target surface during testing to provide a positional radiation flux reference to which the captured light flux distribution can be scaled [102-104]. To mitigate the use of expensive and inaccurate measurement sensors, Ulmer et al. [105] assumed that the total radiation flux captured on the target surface equated to the total flux reflected by the reflector. Thus, only the reflectivity of the reflector and the direct normal irradiance was required to determine the scaling factor. Ho and Khalsa [106] used the reflectivity of the target surface, the direct normal irradiance during testing and a captured image of the sun to determine the scaling factor. Using the sun image as a reference standard to the direct normal irradiance, the image flux on the target surface could be scaled to the equivalent solar thermal flux. Both the methods of Ulmer et al. [105] and Ho and Khalsa [106] required light attenuation filters to be used on the camera lenses in order to mitigate light saturation in the image.

Researchers at the Australian National University investigated an indirect flux mapping method that is carried out using a full moon as the light source rather than the sun [107-109], referred to as photographic lunar flux mapping (PHLLUX). An advantage of lunar flux mapping is that the analysis may be performed during a full moon at night instead of in the midday sun since the moon is considered to produce a flux distribution that is comparable to that of the sun due to their similar angular widths [107]. This minimises the possibility of image saturation, allows for less complex materials to be considered for the target surface, and it mitigates the need for light attenuation filters to be placed over the camera lens due to the decreased irradiance. The method was also previously implemented at the University of Pretoria in characterising the optical performance of a previous parabolic dish design [27].

For these reasons, the PHLLUX method was used in the current research. The light from the full moon was concentrated onto a near-Lambertian target surface that was positioned at the focal point of the reflector. The image projected onto the target surface was captured using a digital camera. The camera processes the image into pixel values that relate to the flux intensity present on the target surface. From this, a flux map was produced. Based on the work of Ho and Khalsa [106], an arbitrary voltage unit of V/px^2 was used to represent the camera sensor data of the image taken, where the voltage represents the average pixel value, and px^2 represents the respective area of the pixel. A Python code (see Appendix A.2) was then used to process the pixel data of the captured image and normalise the

image between the maximum pixel value and minimum pixel value expected to be found along the boundary of the target surface.

An important assumption must be made with this analysis. It is assumed that the solar flux distribution at the target surface ($I_{TS,i}$), normalised by its peak solar flux value, is equal to the normalised flux distribution ($E_{img,i}/E_{img,max}$) presented in the digital image captured of the moonlight concentrated onto the target surface [106]. The relationship is presented in Equation 3-6.

$$\frac{I_{TS,i}}{I_{TS,max}} = \frac{E_{img,i}}{E_{img,max}} \tag{3-6}$$

3.4.1 Experimental setup

For the setup of the lunar flux mapping analysis, a near-Lambertian target surface was placed at the focal point of the dish reflector. The target surface was mechanically mounted onto the focal arm of the two-axis tracker. In the new modular dish design, six reflector facets were mounted onto the central hub of the solar tracker. A digital camera was placed at the base of the dish reflector, directly normal to the target surface to capture the flux distribution on the target surface when the tracker is orientated towards the moon. A schematic of the experimental test setup is presented in Figure 19.

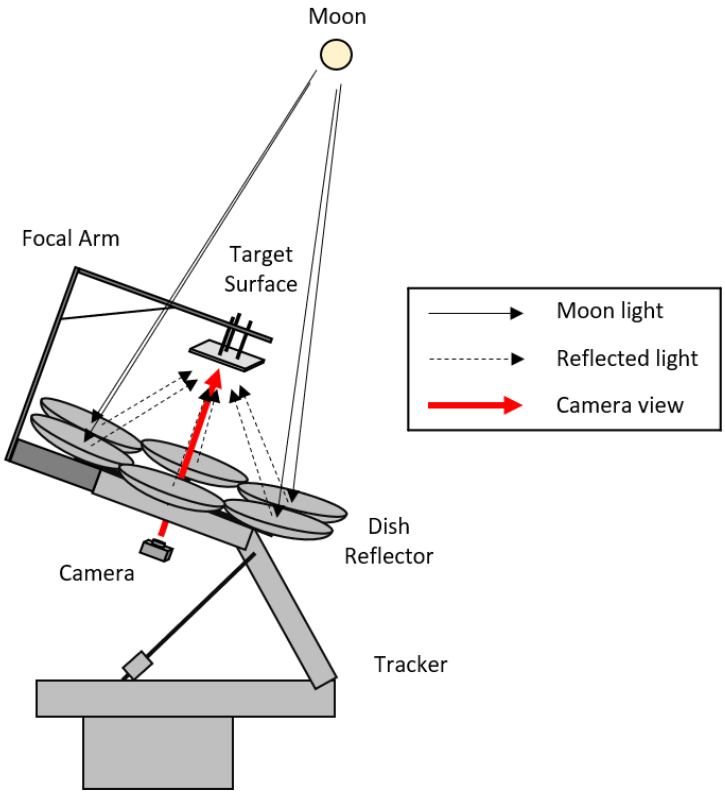

Figure 19: Lunar flux mapping test setup

The elliptical rim of the satellite dish had a width, or minor axis length, of 760 mm, and a length, or major axis length, of 825 mm, which is equivalent to the facet dimensions. A pneumatic valve, comprising a 1/4 inch, threaded nipple, a quarter-turn valve and an 8 mm hose nipple, inserted into the back of the dish, through which a vacuum could be drawn. All the connections at the back of the dish, including the dish mount and the pneumatic valve, were sealed with general-purpose silicone to prevent leaks. The 50 µm thick Mylar sheet was cut from an 8 x 1.2 m Mylar roll using a 780 x 845 mm fabricated elliptical template. Sixteen steel couplets were inserted along the Mylar sheet's perimeter at equal angles, through which a tensioning nylon rope would pull the sheet into equal tensions using a tensioning frame, as shown in Figure 20. A generous amount of SikaTack windscreen silicone was run along the rim of the satellite dish, which was pressed onto the tensioned Mylar sheet, allowing the windscreen silicone to form an airtight seal between the Mylar sheet and the satellite dish. The dish's weight was the only force pushing down on the sheet, which resulted in an evenly tensioned reflector facet that had no wrinkling in the non-vacuum state. It was important to ensure that the Mylar sheet was tensioned evenly to negate wrinkling once the satellite dish was applied. Uneven tensioning of the Mylar sheet would mean that the resulting image at the receiver aperture would be distorted and inaccurate.

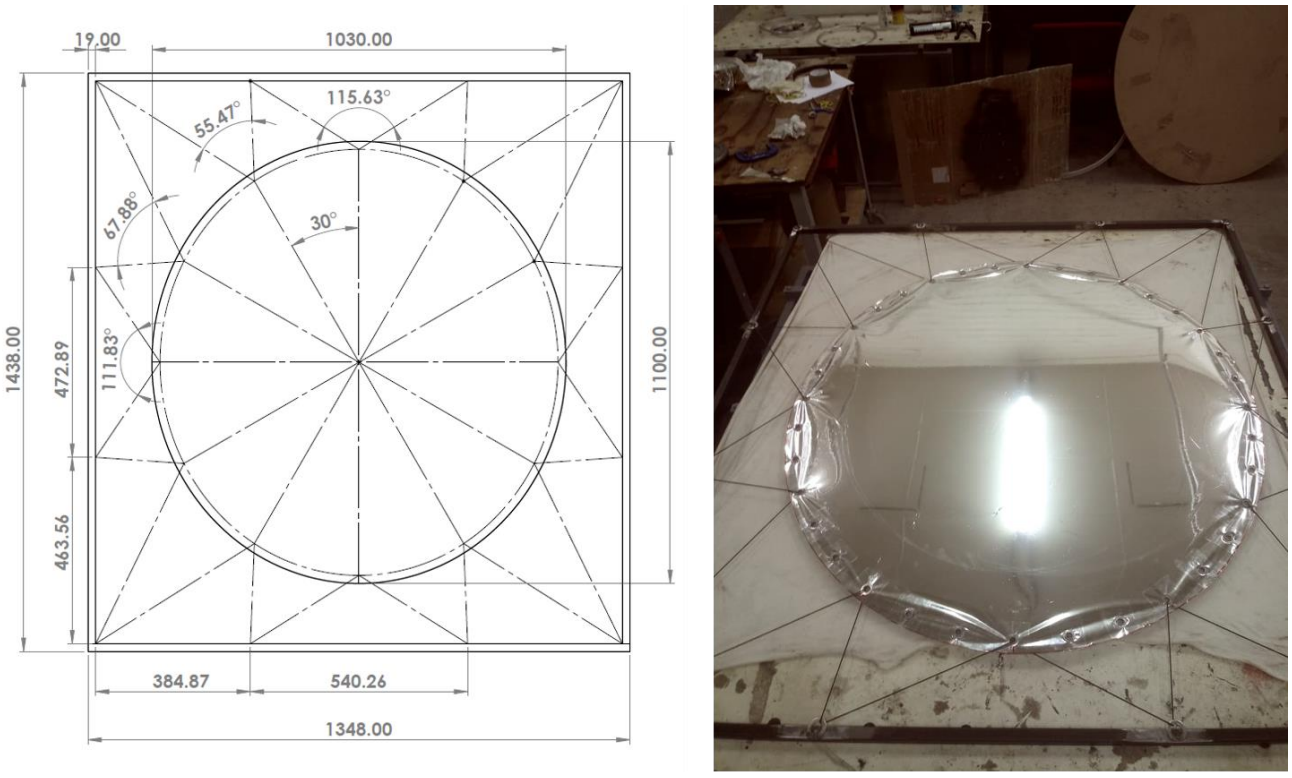

Figure 20: Mylar sheet tensioning frame: (a) schematic; and (b) experimental model

The six reflector facets were mounted onto arms that were subsequently connected to the central hub of the solar tracker. Each arm was tilted roughly 15° towards the central axis of the modular reflector. The facets were then tilted a further 7.5° towards the central axis of the modular reflector, resulting in a total tilt angle of 22.5° for each facet. This was done to obtain an effective rim angle of 45° where the direct normal irradiance from the sun would be reflected off the centroid of each facet at an angle of 45° towards the focal point, assuming ideal specular reflectance. The effective dimensions of the faceted dish represent the equivalent parabolic dish that the faceted dish approximates. The centroids of the reflector facets were positioned 800 mm from the central axis, which allowed the reflector to have an effective diameter of 1.6 m and a total diameter of 2.36 m, as presented in Figure 21. Due to the 45° effective rim angle, the focal point is positioned 800 mm above the horizontal plane of the centroids for the dish facets.

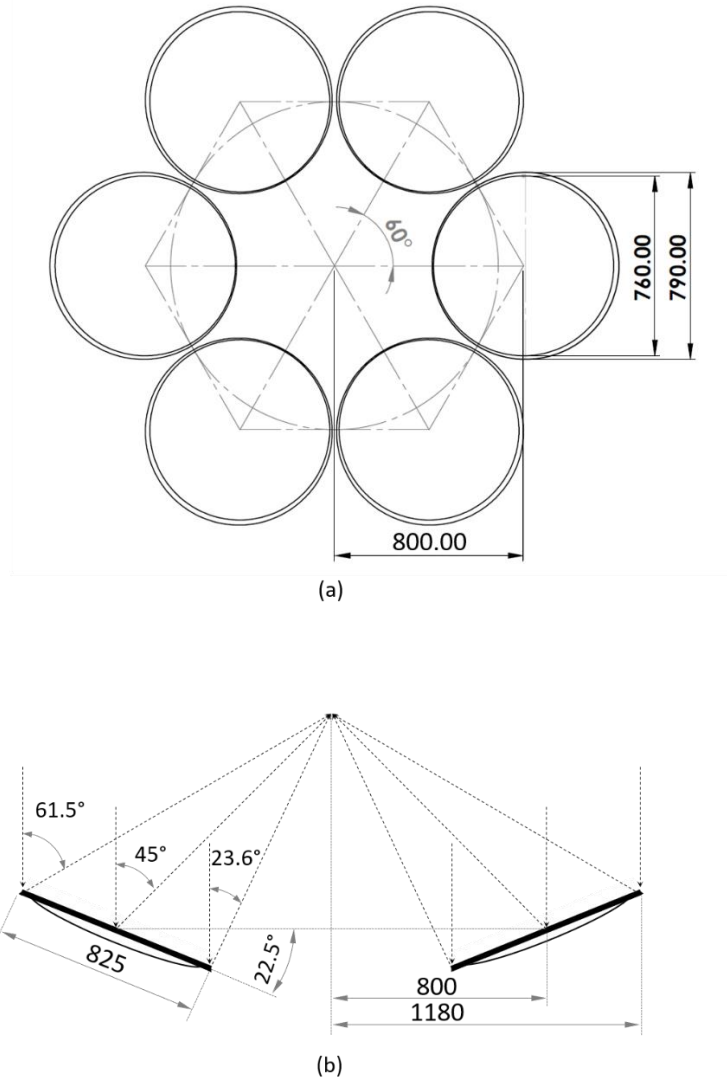

Figure 21: Dish layout and dimensions with (a) a top view; and (b) a sectioned front view with facet rim angles, respectively

The effective focal length was determined to be 965.7 mm, using Equation 2-1.

$$f = \frac{R_{dish}}{2\tan\left(\frac{\psi_{rim}}{2}\right)}$$

$$f = \frac{0.8}{2\tan\left(\frac{45°}{2}\right)}$$

$$f = 0.9657\ m$$

In considering the elliptical shape of the facet rims, the work of Zanganeh et al. [110] suggested that an elliptical facet is beneficial since the tilting of the reflector facet to face the receiver aperture results in a near-circular image being projected onto the receiver aperture plane due to the angularity between the incident solar rays and the tilted reflector facet. This more closely resembles an image projected by an ideal parabolic dish. When comparing the optical performance of elliptical facets to those of conventional circular facets, the elliptical facets performed better with a reported 6.6% increase in intercept factor and a 12% increase in concentration ratio. One obvious disadvantage of faceted dish reflectors is that the incident area off which irradiance may be reflected is smaller compared to a solid parabolic dish reflector with the same dish diameter. Larger reflectors would, therefore, have to be constructed to account for this.

The incident area of the elliptical facets tilted at 22.5° was determined using basic trigonometry. Since the minor axis length (B) of the elliptical facet does not change with the tilting of the facet, the incident area can be determined by calculating the new major axis length (A') and substituting the minor and major lengths into an equation for the area of an ellipse. The new major axis length was determined, according to Figure 22, to be $A' = 0.825\cos(22.5°) = 0.7622$ m. The incident area for a single dish facet was then determined to be $A_{facet} = \frac{\pi}{4}A'B = \frac{\pi}{4}(0.7622)(0.76) = 0.4550\ m^2$, and the total incident area of the reflector was determined by simply multiplying the facet incident area by 6. Thus, $A_{dish} = 2.73\ m^2$.

For comparison, a parabolic dish with an equivalent outer diameter would have an incident area of 4.37 m^2 if the shadow cast by the receiver was negated. The total heat flux reflected by a parabolic dish with an equivalent diameter and reflectance would be roughly 1.6 times larger than the current modular dish design due to this disparity in the incident area. However, the advantages of the current design, as stated in the introduction, are the low building costs and modularity, which allow for different dish shapes to be considered in a single experimental analysis. This is achieved by simply adjusting the reflector facets both in position and in facet concavity through the vacuum that is formed.

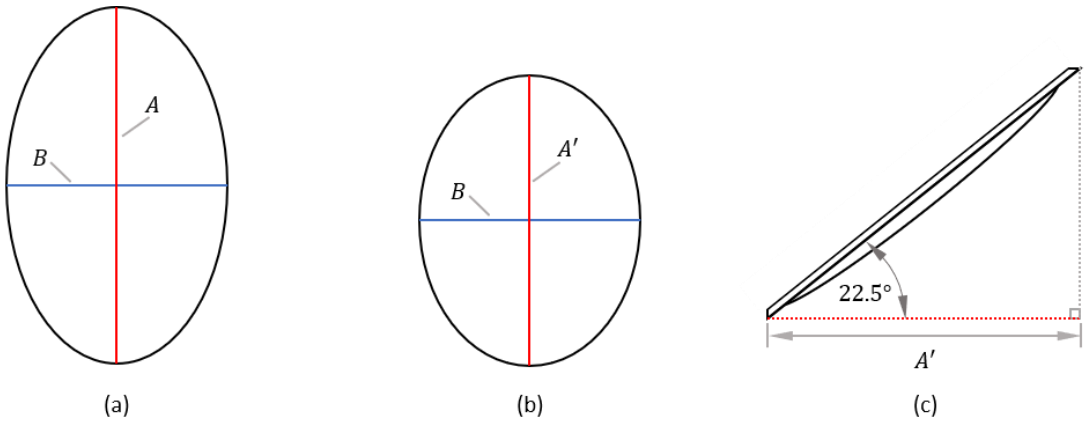

Figure 22: (a): Incident area of the elliptical facet without tilting; (b) incident area of the elliptical facet tilted at 22.5°; and (c) determining the new major axis length for the tilted facet

A near-Lambertian target surface, comprising a 540 x 540 mm chipboard backing was used in the lunar flux mapping experiments. White matt spray paint was used to coat the target side of the chipboard to estimate a Lambertian surface. The matt spray paint that was bought off the shelf is not a perfect Lambertian surface, but since the camera was aligned directly normal to the target surface throughout testing, the error imposed by non-diffuse reflectance was minimised.

In order to ensure that the centroid of the target surface was positioned directly in line with the central axis of the dish reflector, a plummet was used. Faint cross-hairs were drawn at the centroid of the target surface. The string of the plummet was positioned directly on the cross-hairs. The plummet itself was extended down towards the dish reflector. If the target surface was aligned with the dish reflector, the plummet would pass through the central aperture of the reflector. A spirit level was used to ensure that both the base of the reflector and the target surface were aligned with the horizontal plane before using the plummet.

The experimental analysis made use of a two-axis solar tracker that had been constructed on the roof of the University of Pretoria's Engineering II Building by Dr Willem Le Roux during earlier research. The solar tracker orientated the dish reflector towards the moon as it moved across the night sky in an arc. The solar tracker's elevation angle was adjusted using a linear actuator connected to the tracker's arm, and the azimuth angle was adjusted using a rotary actuator fixed at the tracker's base (see Figure 19).

A Canon EOS 700D was used to capture the digital images during testing. The camera settings are listed in Table 14. The photographer chose these settings to mitigate any light saturation that could be present on the image.

Table 14: Camera properties during moonlight test

Property	Value
Aspect ratio	5 184 x 3 456
ISO speed	ISO-100
F-stop	f/4
Exposure time	½ second

3.4.2 Experimental procedure

The lunar flux testing was carried out on a clear night of 14 September 2019 during a full moon. An image of the experimental setup is presented in Figure 23. The camera was fixed to the tracker with the lens aligned with the central axis of the reflector and directly normal to the target surface. Having the camera aligned with the target surface in this way mitigated any cosine errors that would occur during the testing [106].

(a) (b)

Figure 23: Images of the experimental setup during lunar flux testing

A vacuum was formed in each reflector facet to cause a concavity that concentrated the reflected moonlight onto the 540 x 540 mm target surface. The collector was aimed by observing the shadow cast onto the base of the reflector by the target surface and making sure that the centroid of the

shadow intercepted the central axis of the reflector. The dish facets were adjusted separately, both in position and in shape, to create an optimal image of the concentrated moonlight at the crosshairs of the target surface. The camera then took a set of images. A raw CR2 image and a JPEG image were taken of the lunar flux distribution on the target surface to analyse the effect of information loss between the raw image and a general JPEG file. The flux distribution represents the gradients of illumination present in the concentrated lunar image on the target surface. Figure 24 presents an enhancement of the JPEG image of the concentrated lunar image projected onto the target surface during testing. The JPEG image was enhanced using a flash for the purposes of determining the positioning and dimensions of the target surface in the pixel array.

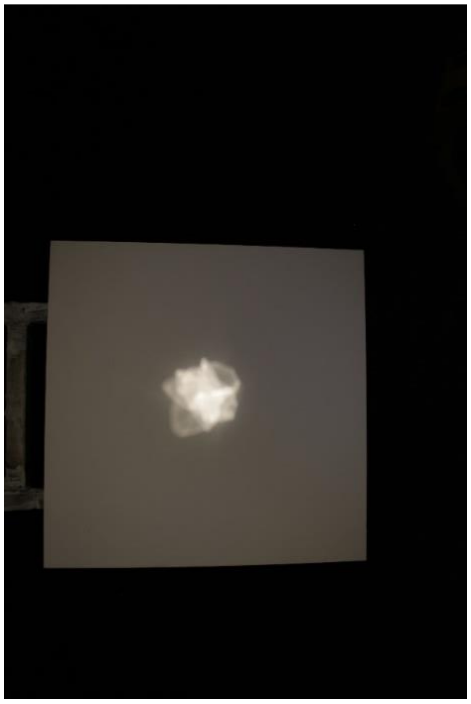

Figure 24: Enhanced JPEG image captured by Mr Vincent Good

3.4.3 Results

The images taken by the camera were processed using a Python code, developed in collaboration with Mr Roosendaal (see Appendix A.2), to produce a pair of resulting normalised flux maps. When processing the JPEG image, a greyscale image was produced by averaging the RGB pixel values over the entire image. This produced a pixel value flux distribution that ranged between 0 and 255 V/px^2. A pixel value of 255 V/px^2 indicates that light saturation occurred for the given pixel value. It is important to ensure that light saturation does not occur as gradient information will be lost, leading to an inaccurate representation of the flux distribution. The aspect ratio of the image file was then scaled to its respective distance values by determining the associated area per pixel.

This was done by dividing the total target surface area of 540 x 540 mm by the total number of pixels on the target surface. Based on the assumption that each pixel represents a square area on the target surface and that the area per pixel did not change, the length of the square pixel was determined by calculating the square root of the pixel area. For the JPEG normalised flux map presented in Figure 25a, the maximum and minimum pixel values were determined to be 251.33 and 0 V/px^2, respectively. The pixel values were normalised by the maximum pixel value to produce a normalised flux distribution scaled between 0 and 1.

A similar scaling was performed with the CR2 image file after post-processing using the "RawPy" module [111]. Using the "rawpy.postprocess" function, a numpy array was returned that contained a 14 bit, standard RGB array, which was then averaged and normalised by its maximum pixel value to produce a normalised flux distribution between 0 and 1. The pixel values outside the target surface boundary were set to 0 to negate the exposure to the night sky. The process code may be found in Appendix A. The resulting normalised flux map is presented in Figure 25b.

An interesting observation that may be made between the normalised flux maps in Figure 25 is that the normalised flux map of the CR2 image file appears to have notably less light on the boundaries of the target surface than that of the JPEG. This may be because of the pixel defeaturing that occurs during image compression when a JPEG file is developed from the raw sensor data within the camera. An algorithm was used to compress the sensor data over the pixel area and, in doing so, reduced the information per pixel contained in the JPEG image. The loss of information appears to have resulted in an over-representation of the light present on the boundaries of the target surface. No defeaturing occurred with the post-processing of the CR2 file, so the resulting normalised flux map is directly proportional to all the raw sensor data that was captured by the camera [112].

In order to account for light pollution, an average of the pixel values along the boundary of the target surface was calculated. The average was then subtracted from the entire normalised flux map. This average was determined to be 0.002 for the CR2 normalised flux distribution and 0.005 for the JPEG. The resulting normalised flux maps without light pollution are presented in Figure 26. The maximum normalised pixel values for the JPEG and the CR2 images were now 0.995 and 0.998, respectively.

Cuts were made along the vertical and horizontal planes intersecting the centre of mass of each normalised flux map, and their associated pixel values were plotted, to better define their respective distributions. The centre of mass for each distribution was determined by considering each pixel value as a discretised weighting value. The plots detailing the normalised pixel values along the vertical and

horizontal cuts of the JPEG and CR2 normalised flux maps are presented in Figure 27 and Figure 28 respectively.

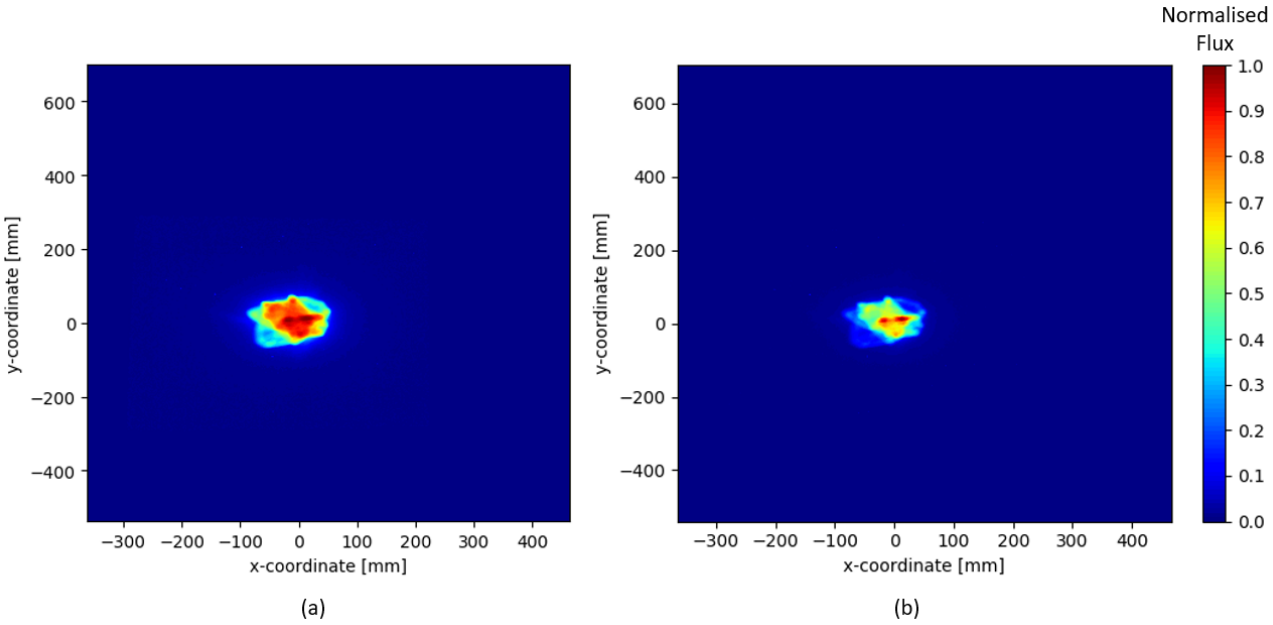

Figure 25: Normalised flux map (with pollution) of: (a) the processed JPEG flux distribution; and (b) the CR2 pixel flux distribution

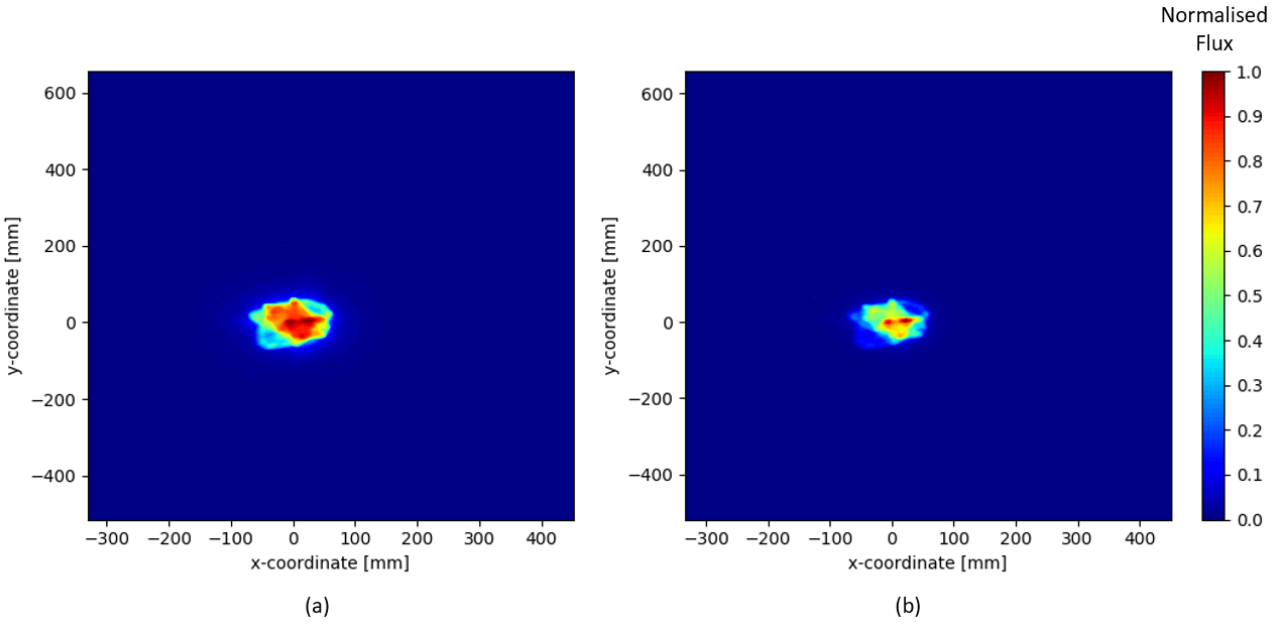

Figure 26: Normalised flux map (without pollution) of: (a) the processed JPEG flux distribution; and (b) the CR2 pixel flux distribution

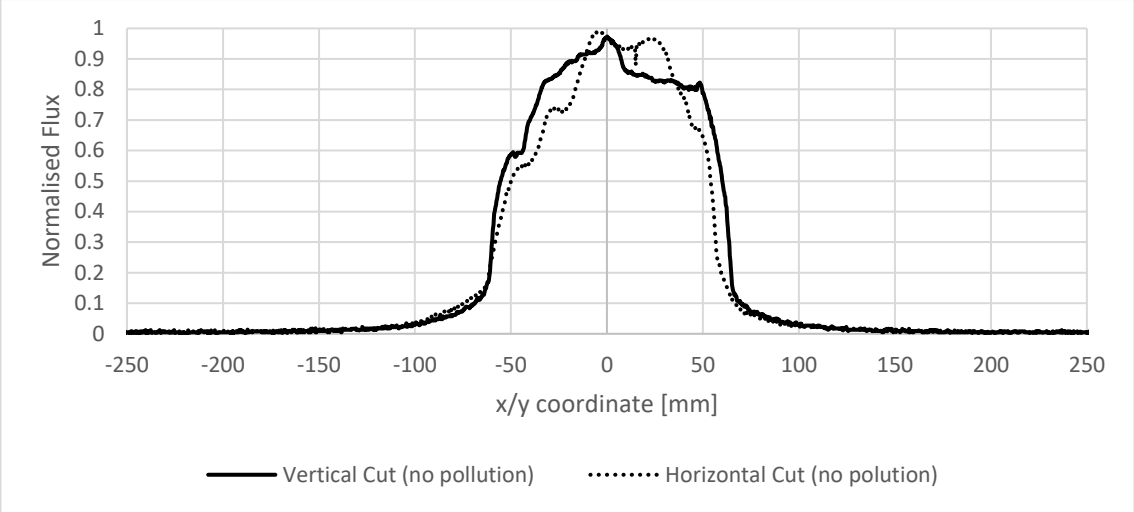

Figure 27: Vertical and horizontal cuts at the centre of mass of the no-pollution normalised flux distribution for the JPEG image

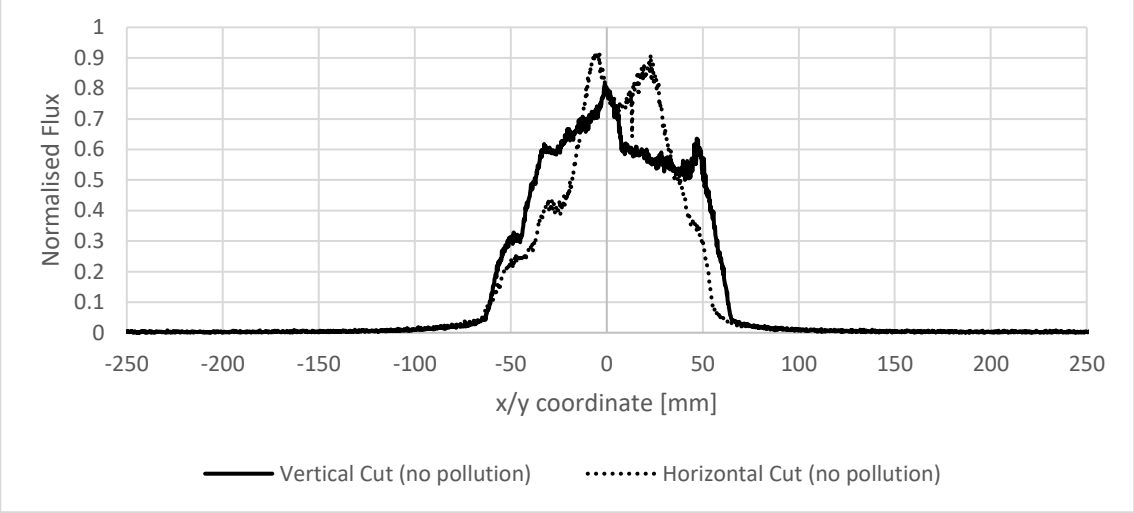

Figure 28: Vertical and horizontal cuts at the centre of mass of the no-pollution normalised flux distribution for the CR2 image

It is evident from the figures that the distribution of the CR2 image is marginally narrower than that of the JPEG. It is this discrepancy that is being analysed in its influence on the intercept factor trends. The CR2 cuts do not reach the maximum value of 0.998 at the centre of mass, which merely means that the maximum normalised pixel value is not located at the centre of mass. However, the centre of mass should still be considered as the origin point from which the aperture should be expanded as it will produce the optimum intercept factor trend.

3.4.4 Discussion

Some important analyses were made based on the normalised flux map results. These are presented and discussed in the following section. Firstly, the intercept factor was determined for a range of aperture diameters. The intercept factor trends of the JPEG and CR2 normalised flux maps are presented and discussed. A case was analysed where the incident solar flux was scaled to the normalised CR2 flux map, from which the maximum concentration ratio was determined.

3.4.4.1 Intercept factor

Based on the normalised flux maps that are presented in Figure 25 and Figure 26, the intercept factors of the varied aperture diameters were determined. The CR2 data was considered to be the reference measure as no information was lost due to image compression as in the case of the JPEG images. The reason for the comparison between the two image formats is to observe how much the JPEG intercept factor deviates from that of the CR2. A JPEG image is less memory intensive and is easier to process than its raw counterpart. It is thus justifiable to investigate how well the intercept factor of the JPEG compares to that of the CR2.

Since all pixels outside the target surface boundaries were set to 0, as stated in Section 3.4.3, the total normalised flux present on the target surface is simply a summation of the entire pixel array ($\sum E_{img,i} / E_{img,max}$). The intercept factor (IF) was determined by summating the normalised pixel values that fell within the aperture area ($E_{img,intercept}/E_{img,max}$) for a given diameter and dividing it by the total normalised flux present on the target surface, as presented in Equation 3-7. Using the distance scaling performed in Section 3.4.3, the aperture diameter was varied from 0 to 764 mm and expanded outwards from the centre of mass of the normalised flux distribution.

$$IF = \frac{\sum E_{img,intercept}/E_{img,max}}{\sum E_{img,i} / E_{img,max}} \times 100 \qquad (3\text{-}7)$$

From the intercept factor trends plotted in Figure 29, a notable difference can be observed between the pollution and the non-pollution trends. Although the pollution at the boundaries was almost negligible per pixel value, the accumulative effect is apparent where the intercept factor trends differ by a maximum of 10% at an aperture size of 181 mm for the JPEG's normalised flux distribution and 7% at an aperture size of 160 mm for the CR2. Furthermore, a notable deviation can be observed between the no-pollution JPEG and CR2 intercept factor trends between aperture diameters of 20 and 200 mm. A maximum deviation of 12% occurred at an aperture diameter of 100 mm between the CR2 (no-pollution) intercept factor and that of the JPEG. From this analysis, it is observed that the deviation only drops below 2% after an aperture diameter of 200 mm.

This deviation is too large for apertures ranging between 135 and 200 mm, which is the range that is being considered in the experimental receiver aperture design. The trend of the non-pollution CR2 intercept factor is thus considered further in the study. From the aperture range being considered, the experimental intercept factor will fall between 87 and 93%.

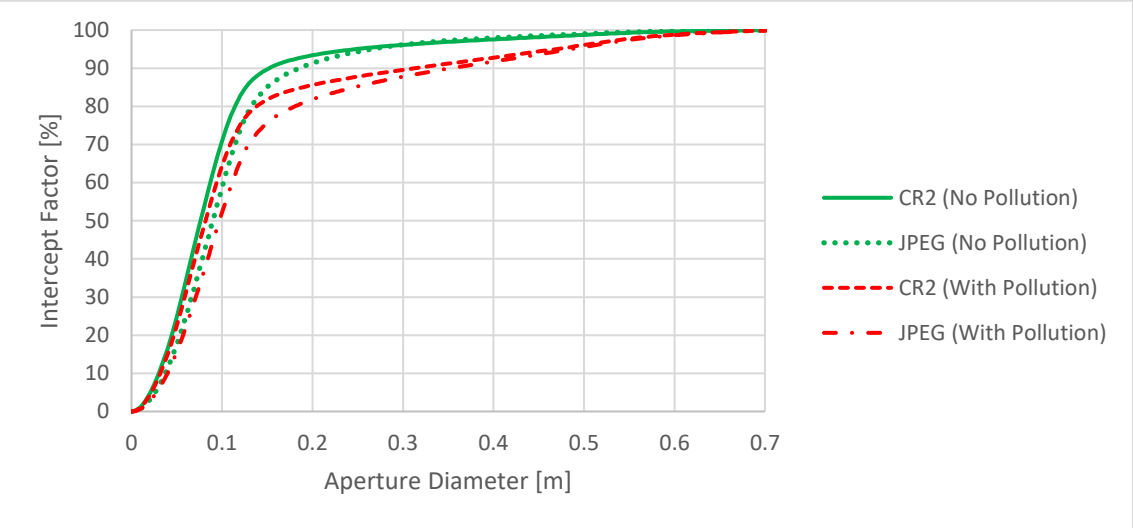

Figure 29: Intercept factor as a function of aperture sizing

3.4.4.2 Solar flux distribution

In this section, a theoretical test case is considered where the solar collector experiences a direct normal irradiance of 1 000 W/m^2. Using the normalised CR2 flux map, the concentrated radiation from the dish reflector may be scaled to the normalised flux map to produce an equivalent solar flux map that can be expected to occur at the focal length of the dish reflector during a normal day of testing.

Based on the work of Ho and Khalsa [106], the solar flux distribution on the target surface is approximated to be directly proportional to the normalised flux distribution on the flux map determined from the moonlight testing. The solar flux distribution ($I_{TS,i}$) can be determined by multiplying the normalised flux distribution by a thermal scaling factor (K) as shown in Equation 3-8. With reference to Equation 3-6, the peak solar flux is thus the scaling factor used to determine the solar flux distribution. In accordance with the work of Ulmer et al. [105] and the research at the Australian National University [108, 109], it is assumed that all reflected light is captured by the target surface. This means that the flux intensity along the boundaries of the target surface should be zero or close to zero, which can be checked during post-processing.

$$I_{TS,i} = K \times \frac{E_{img,i}}{E_{img,max}} \tag{3-8}$$

In order to scale the normalised flux map to represent the solar flux distribution, the total radiation incident on the target surface during midday testing must be determined. The incident solar radiation on the target surface can be defined as the sum of the discretised radiation pixel values that form the solar flux distribution on the target surface as shown in Equation 3-9.

$$\dot{Q}_{TS,approx} = \sum_{i}^{TS} I_{TS,i} \tag{3-9}$$

Another way of determining the total incident radiation on the target surface is by considering the DNI and the optical properties of the dish reflector. The solar radiation incident on the dish reflector ($\dot{Q}_{sun}$) is expressed in Equation 3-10, where I_{sun} is the DNI from the sun and A_{dish} is the incident area of the dish reflector.

$$\dot{Q}_{sun} = I_{sun} A_{dish} \tag{3-10}$$

Only a fraction of the incident radiation can be reflected from the dish reflector due to the optical properties of the reflector facets. Further attenuation of the incident light on the target surface may occur due to spillage. The reflected radiation incident on the target surface is thus a function of the dish reflector's optical efficiency (η_{op}) and dish reflectivity (η_{ref}), as expressed in Equation 3-11.

$$\dot{Q}_{TS} = \eta_{op} \eta_{ref} \dot{Q}_{sun} \tag{3-11}$$

Based on the analysis of the CR2 flux map, it is assumed that no spillage occurs from the target surface ($\eta_{op} = 1$). The reflectivity of the Mylar sheet was determined to be $\eta_{ref} = \rho_{mylar} = 0.97$ based on UV/VIS spectrometry testing. The total power incident on the target surface should equal the total power reflected by the dish reflector. This results in the summation of the discretised radiation pixel values relating to the irradiance from the sun, as expressed in Equation 3-12.

$$\dot{Q}_{TS} = \eta_{ref} I_{sun} A_d = \sum_{i}^{TS} I_{TS,i} \tag{3-12}$$

Using equations 3-8 and 3-12, a peak solar flux can be determined, resulting in a solar flux distribution that would be equivalent to the solar flux distribution expected during the day. When summated over the target surface, the total incident radiation would correlate to the given direct solar irradiance in Equation 3-12. The peak solar flux was determined using the Nelder-Mead optimisation algorithm [95] (see Appendix A). The resulting solar flux map is presented in Figure 30. The peak solar concentration ratio at the target surface may then be determined using Equation 3-13, which describes the degree to which the reflected solar radiation is concentrated.

$$C = \frac{I_{TS,max}}{\eta_{ref} I_{sun}} \tag{3-13}$$

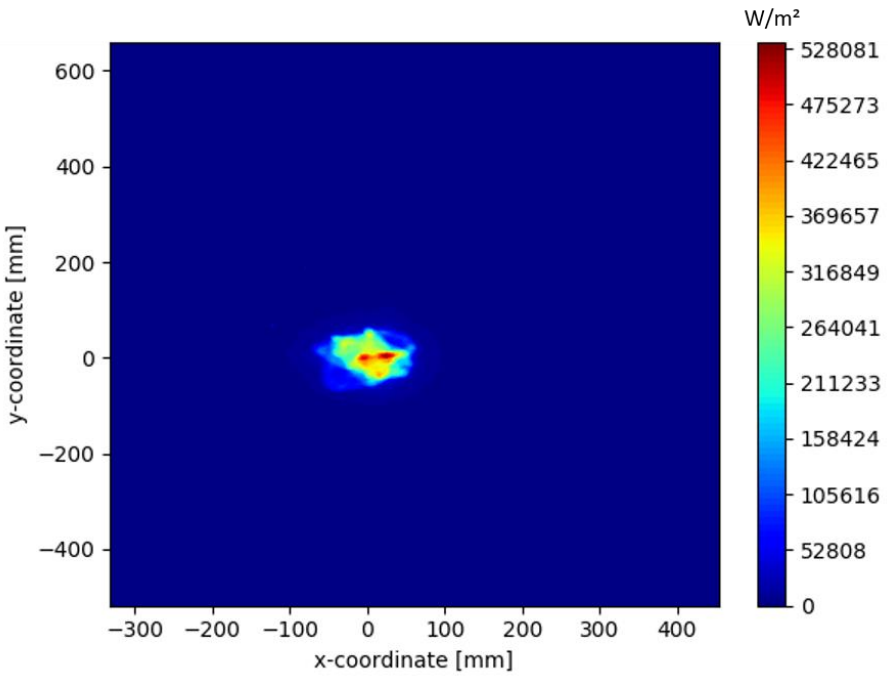

Figure 30: Resulting solar flux map for a DNI of 1 000 W/m^2

For a test case with a solar DNI of $I_{sun} = 1000\ W/m^2$ and a facet reflectivity of $\eta_{ref} = 0.97$, the optimiser determined the maximum solar flux to be 528 081.46 W/m^2. This resulted in a total incident radiation on the target surface that was accurate to $10^{-2}\ W$ when compared to the target surface radiation calculated by considering the DNI. Using Equation 3-13, the resulting peak concentration ratio was determined to be 544.41, which is comparable to the concentration ratios of heliostat fields presented in the literature study [37].

3.5 Conclusion

The optical performance of the novel modular reflector design was investigated. It was important to characterise the performance of the reflector. The primary objective of the analysis was to determine the amount of solar radiation that would be intercepted at the receiver aperture. The results could then be used to calculate the thermal efficiency of the receiver during solar testing.

Using UV/VIS spectroscopy, the spectral reflectivity of the Mylar facet was determined to be 97% within the visible light spectrum. This accounts for approximately half of the total solar spectrum present on the surface of the earth.

The shape of the facet concavity, produced by forming a vacuum in the cavity of the dish facet, was investigated using photogrammetry. The investigation would prove useful in future work by allowing for the concave shape to be accurately modelled in a numerical analysis. An elliptical paraboloid and a hemi-ellipsoid were fitted to the photogrammetry results, and it was determined that the hemi-ellipsoid most accurately resembled the concave shape.

The intercept factor at the receiver aperture was investigated through photographic lunar flux mapping. The analysis was performed in the clear light of a full moon, and pictures were taken of the concentrated image on a near-Lambertian target surface positioned at the focal point of the dish reflector. The normalised flux maps where light pollution was corrected, as well as the uncorrected normalised flux maps, were produced for the raw image, as well as an equivalent JPEG image, for the purpose of comparing the variation in the accuracies of the given methods. It was found that the JPEG image inaccurately represented the flux distribution on the target surface due to image compression.

The intercept factor trend for the raw normalised flux distribution with light pollution correction was considered to be the most accurate representation of the solar flux distribution on the target surface. This is because no pixel information is lost due to image compression. Based on the results, an intercept factor ranging between 87 and 93% was considered for the intended receiver design, with an aperture diameter ranging between 135 and 200 mm.

4. Thermal analysis

4.1 Introduction

The experimental model that was used to evaluate the performance of the solar collector in the Rankine cycle is presented in this section. It is important to analyse the performance of the solar collector as a step in determining the feasibility of implementing decentralised solar thermal power generation in rural areas, since the solar collector plays a crucial role in this. An analytical model is presented that will be used to characterise the performance of the solar collector. The developed experimental setup is presented, along with the method of testing. Based on the analytical model, the results will be discussed based on power generation, heat loss and generation efficiency.

4.2 Analytical model

The analysis model was used to determine the first- and second-law efficiency of the receiver. A heat-loss model is presented to define the components of heat loss in the receiver.

4.2.1 Fluid properties

The fluid thermodynamic properties were determined from temperature and pressure measurements, using the CoolProp add-on for Excel. The water properties were determined through partial derivatives of the Helmholtz energy formulations [34].

4.2.2 First-law analysis model

The heat transfer rate that is present at the receiver tubes must account for losses from the receiver in which there are conduction, convection and radiation heat losses. This is expressed in the energy balance given in Equation 4-1.

$$\dot{Q}_{net} = \dot{Q}_{ap} - \dot{Q}_{cond,loss} - \dot{Q}_{conv,loss} - \dot{Q}_{rad,loss} \quad (4\text{-}1)$$

If the components of heat loss are not estimated, the loss terms may be replaced by a single loss term, as expressed in Equation 4-2.

$$\dot{Q}_{net} = \dot{Q}_{ap} - \dot{Q}_{loss} \quad (4\text{-}2)$$

The net heat transfer rate captured by the working fluid in the coiled tubes is expressed in Equation 4-3.

$$\dot{Q}_{net} = \Delta H_w = \dot{m}_w(h_{w,out} - h_{w,in}) \quad (4\text{-}3)$$

Considering the incident solar radiation on the dish reflector, as described in Section 3.4.4.2, and the intercept factor (IF) of the collector and the reflectivity of the reflector facets (η_{ref}) determined in Chapter 3, the total radiation intercepted at the aperture of the receiver can be expressed using Equation 4-4.

$$\dot{Q}_{ap} = IF \times \eta_{ref} I_{sun} A_{dish} \tag{4-4}$$

The fundamental energy conservation equation is expressed using Equation 4-5. It describes how the net energy absorbed by the receiver changes the energy state of the working fluid that flows through the coils.

$$\dot{Q}_{net} = IF \times \eta_{ref} I_{sun} A_{dish} - \dot{Q}_{loss} = \dot{m}_w (h_{w,out} - h_{w,in}) \tag{4-5}$$

The thermal efficiency of the receiver is expressed as a fraction of the net heat transfer rate into the working fluid over the intercepted radiation that is reflected from the dish and expressed in Equation 4-6.

$$\eta_{th,rec} = \frac{\dot{Q}_{net}}{\dot{Q}_{ap}} = \frac{\dot{m}_w (h_{w,out} - h_{w,in})}{IF \times \eta_{ref} I_{sun} A_d} \tag{4-6}$$

The thermal efficiency of the collector is determined by considering Equation 4-7.

$$\eta_{th,col} = \frac{\dot{Q}_{net}}{\dot{Q}_{sun}} = \frac{\dot{m}_w (h_{w,out} - h_{w,in})}{I_{sun} A_d} \tag{4-7}$$

4.2.3 Heat loss model

It is important to estimate the components of heat loss in order to characterise the performance of the receiver. The fundamental components of heat loss in a cavity receiver were determined to be convection heat loss through the cavity aperture, radiation heat loss through the cavity aperture and conduction heat loss through the cavity insulation. These heat loss components are illustrated in Figure 31, which shows the heat loss mechanisms, as well as the intercepted radiation, through a receiver aperture.

4.2.3.1 Convection heat loss model

The convection heat loss model is divided into two components: the natural convection heat loss ($\dot{Q}_{loss,natural}$) and the forced convection heat loss ($\dot{Q}_{loss,forced}$). Natural convection heat loss occurs due to buoyancy forces from the air being heated within the cavity receiver and escaping through the aperture. The forced convection component occurs due to the effect of wind blowing over the receiver aperture, resulting in convection heat loss. Assuming that the two components are independent of

one another, they are summated, resulting in total convection heat loss from the aperture of the receiver, as shown in Equation 4-8 [71].

$$\dot{Q}_{conv,loss} = \dot{Q}_{loss,natural} + \dot{Q}_{loss,forced} \tag{4-8}$$

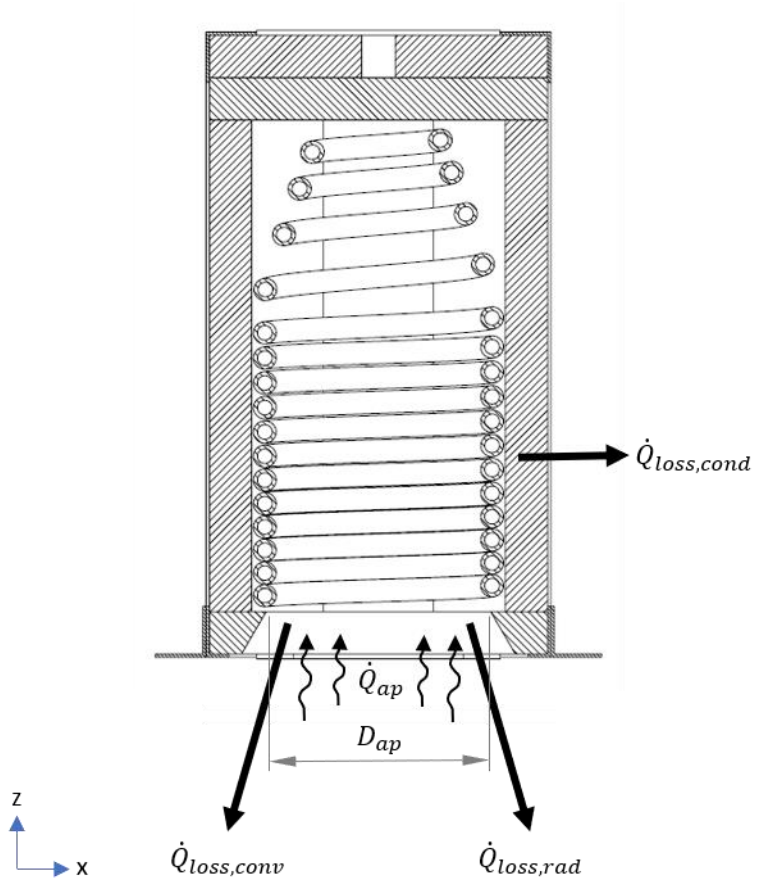

Figure 31: Schematic of heat losses present in a cavity receiver

As discussed in the literature study, empirical correlations have been determined to estimate the Nusselt number with regard to the natural convection heat transfer coefficient. The correlations considered in the current research are the correlation of Koenig and Marvin [68], presented in Equation 2-38, and the correlation of Stine and McDonald [43], presented in Equation 2-41.

Based on the literature, the forced convection heat transfer coefficient was determined by approximating the value to be twice that of the natural heat transfer coefficient at wind speeds below 4.5 m/s [72]. The correlation of Ma [71] in Equation 2-43 was not considered, since it was developed for a particular receiver geometry at a specific set of operating conditions, while only varying the wind speed.

The convection heat loss from the aperture may be calculated using Equation 4-9. The i-subscript denotes the forced and the natural convection components.

$$\dot{Q}_{loss,i} = \bar{h}_i A(T_s - T_\infty) \quad (4\text{-}9)$$

The area (A) was defined, in the correlation of Koenig and Marvin [68], to be the surface area of the exposed receiver tubing, whereas the correlation of Stine and McDonald [43] defined the area to be the total exposed surface area inside the receiver cavity. This includes the exposed cavity walls in the receiver [71]. The forced convection heat loss component was determined using the respective area considered in the natural convection heat loss correlations.

4.2.3.2 Radiation heat loss model

The radiation heat loss ($\dot{Q}_{rad,loss}$) was estimated by considering the reflected radiation from the receiver cavity, as well as the emitted radiation for the receiver coils, as presented in Equation 4-10. The reflected radiation component is a function of the optical properties of the receiver coil, as well as the receiver geometry. Without appropriate numerical simulation of the flux distribution within the cavity, some simplifying assumptions were made for the purpose of analysing the radiative properties of the receiver cavity. The assumptions were based on the fact that the radiation was only incident on the first seven coil turns within the receiver cavity, which were close to the receiver aperture. Firstly, it was assumed that the inner cavity reflected the incident radiation in a diffuse manner. Secondly, the inner cavity had optical properties that were comparable to those of the stainless steel coil tubes. Thus, the reflected radiation heat loss through the cavity aperture was dependent on the reflectivity of the coil tubes, as well as the view factor between the inner cavity and the surroundings. The view factor between the inner cavity and its surroundings was determined to be equivalent to the view factor between the inner cavity and the aperture, since the view factor between the aperture and its surroundings was approximately 1.

The aperture was considered to be a two-dimensional surface with a surface temperature equal to the average surface temperature of its surroundings and had an approximated emissivity of 1. The radiation heat loss was thus determined using equations 4-10 and 4-11.

$$\dot{Q}_{rad,loss} = \rho_{steel} F_{s-ap} \times \dot{Q}_{ap} + \dot{Q}_{emitted,s-ap} \quad (4\text{-}10)$$

$$\dot{Q}_{rad,loss} = \rho_{steel} F_{s-ap} \times IF\eta_{ref} I_{sun} A_d + \frac{\sigma(T_s^4 - T_{ap}^4)}{\left[\frac{1-\varepsilon_s}{A_s\varepsilon_s} + \frac{1}{A_s F_{s-ap}} + \frac{1-\varepsilon_{ap}}{A_{ap}\varepsilon_{ap}}\right]} \quad (4\text{-}11)$$

4.2.3.3 Conduction heat loss model

The conduction heat loss through the cavity insulation was modelled by considering the conduction mechanism through the insulation medium, as well as the convection mechanism present on the outside of the receiver cavity. This is evident in the thermal resistance (R_{tot}) presented in Equation 4-12.

$$\dot{Q}_{cond,loss} = \frac{T_s - T_\infty}{R_{tot}} = \frac{T_s - T_\infty}{\frac{t_{ins}}{k_{ins}A_{ins,in}} + \frac{1}{\bar{h}A_{ins,out}}} \quad (4\text{-}12)$$

The convection heat transfer coefficients on the outer surfaces of the receiver cavity were determined using the correlation for convection over a flat plate. The convection heat transfer coefficient is dependent on the orientation of the dish with respect to the wind. For that reason, the following correlations were considered:

For forced convection over surfaces that are parallel to the wind velocity, the correlations for laminar and turbulent flow over a flat plate, given in Cengel and Ghajar [48], were used and are presented in equations 4-13 and 4-14 respectively.

$$Nu = \frac{\bar{h}L}{k} = 0.664 Re_L^{0.5} Pr^{1/3} \quad (4\text{-}13)$$

$$Nu = \frac{\bar{h}L}{k} = 0.037 Re_L^{0.8} Pr^{1/3} \quad (4\text{-}14)$$

For forced convection on the front, back, and side walls, the Nusselt number is estimated using the correlation for cross-flow on a square tube perpendicular to the wind velocity in Equation 4-15 and the correlation for cross-flow on a square tube tilted 45° to the wind velocity in Equation 4-16 [113].

$$Nu = \frac{\bar{h}L}{k} = 0.094 Re_L^{0.675} Pr^{1/3} \quad (4\text{-}15)$$

$$Nu = \frac{\bar{h}L}{k} = 0.258 Re_L^{0.635} Pr^{1/3} \quad (4\text{-}16)$$

For natural convection from the outer surfaces of the receiver cavity, the tilt angle must be taken into account. The correlation, given in Cengel and Ghajar [48], is thus considered and presented in Equation 4-17. This expression describes the natural convection heat transfer rate for inclined plates with a laminar boundary layer that forms over the plate's surface.

This phenomenon typically occurs on the bottom surface of an inclined heated plate and is comparable to the natural convection heat transfer rate that occurs for vertical plates.

$$Nu = \frac{\bar{h}L}{k} = 0.59 {Ra_L}^{1/4} \cos^{1/4}(\varphi) \quad (4\text{-}17)$$

$$\varphi + \theta = 90° \quad (4\text{-}18)$$

The inclination angle (φ) of the surface is considered to be the angle between the vertical axis and the normal angle of the surface. The surface's inclination angle is considered to be the angular complement of the surface's elevation angle (θ), which is described in Section 2.4.4. Summation of the

surface's inclination angle and the surface's elevation angle would thus equate to 90°, as presented in Equation 4-18. The natural convection that occurs at the top surface of an inclined heated plate was investigated by Fujii and Imura [114], and the correlation – considering a 300 mm plate – was determined. It is presented in Equation 4-19.

$$Nu = \frac{\bar{h}L}{k} = 0.13\left[(Gr_L Pr)^{1/3} - (Gr_c Pr)^{1/3}\right] + 0.56(Gr_c\, Pr\, cos\varphi)^{1/4} \quad (4\text{-}19)$$

The characteristic Rayleigh number ($Gr_c Pr$) was used in the correlation to represent the transition regions along the plate where buoyancy forces caused boundary layer separation, resulting in the Nusselt number diverging from the characteristic of the laminar region. The transitional region was determined in the work of Vliet [115]. Fujii and Imura [114] illustrated this transition region on a graph that related the characteristic Rayleigh number to the respective inclination angle during experimental validation. The graph was digitised and is presented in Figure 32. For the current study, the characteristic Rayleigh number was determined by calculating an average value between the upper and lower intervals presented by Vliet [115] for the given angle of inclination.

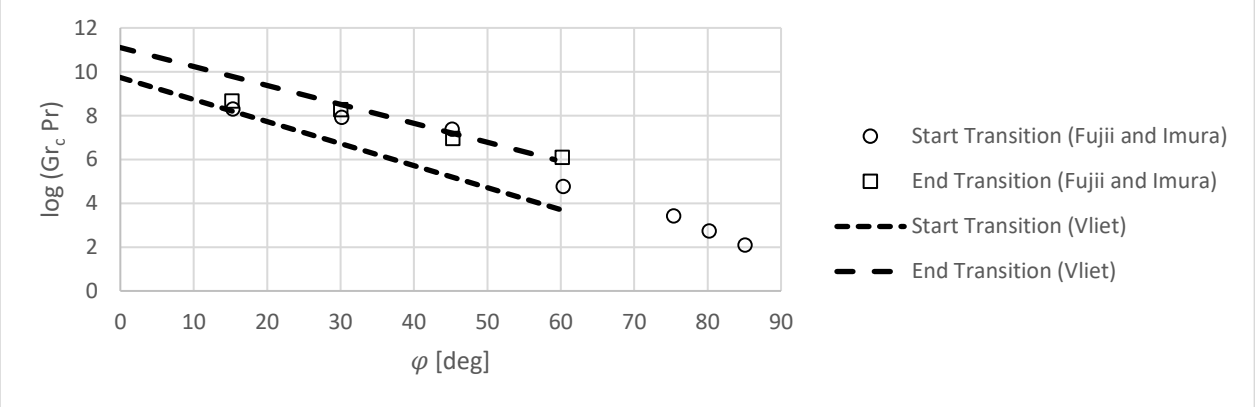

Figure 32: Relationship between the characteristic Rayleigh number and the inclination angle of an inclined heated plate

When considering the combined natural and forced convection components, the correlation, given in Cengel and Ghajar [48], is used and presented in Equation 4-20. The exponent n tends to be roughly 3 for vertical surfaces and 4 for horizontal surfaces in experimental data.

$$Nu_{combined} = \frac{\bar{h}L}{k} = \left(Nu_{forced}^{n} \pm Nu_{natural}^{n}\right)^{1/n} \quad (4\text{-}20)$$

The characteristic length differs, depending on the correlation used for natural and forced convection. For this reason, the characteristic length of the combined Nusselt number was determined by

considering the weighted average of the characteristic lengths used during the natural and forced convection Nusselt number calculations, as presented in Equation 4-21.

$$Lc_{combined,i} = \left[Lc_{forced,i} \times \frac{Nu_{forced,i}^{n}}{Nu_{forced,i}^{n} + Nu_{natural,i}^{n}} + Lc_{natural,i} \times \frac{Nu_{natural}^{n}}{Nu_{forced,i}^{n} + Nu_{natural,i}^{n}} \right] \quad (4\text{-}21)$$

4.2.4 Second-law analysis model

Exergy is simply the measure of how much a certain quantity of energy is worth, relative to its surroundings. It is described as the useful component of the given energy supply. Thermodynamic exergy can be divided into three primary components: the exergy of the working fluid, the available work of the heat transfer rate and the mechanical work from turbines and pumps. The exergy gained by the working fluid flowing through the receiver is described as the difference between the exergy state of the fluid at the outlet and the inlet. The expression for the exergy state of the working fluid is given in Equation 4-22 where the change in exergy of the working fluid is expressed using Equation 4-23.

$$\Psi_w = \dot{m}_w[(h_w - h_\infty) - T_\infty(s_w - s_\infty)] \quad (4\text{-}22)$$

$$\Delta\Psi_{\mathrm{w}} = \Psi_{\mathrm{w,out}} - \Psi_{\mathrm{w,in}} \quad (4\text{-}23)$$

The general expression of available work due to the heat transfer rate is defined using Equation 4-24.

$$\Phi = \dot{Q}\left[1 - \frac{T_\infty}{T_s}\right] \quad (4\text{-}24)$$

The available work due to solar radiation has been described in past works using the derivation of Petela [116], as presented in Equation 4-25.

$$\Phi_{sun} = \dot{Q}_{sun}\left[1 + \frac{1}{3}\left(\frac{T_\infty}{T_{sun}}\right)^4 - \frac{4T_\infty}{3T_{sun}}\right] \quad (4\text{-}25)$$

According to Onyegegbu and Morhenne [117], a more widely accepted expression is given in Equation 4-26, as research from Farahat et al. [118] suggests that Equation 4-25 violates the second law of thermodynamics.

$$\Phi_{sun} = \dot{Q}_{sun}\left[1 - \frac{4T_\infty}{3T_{sun}}\right] \quad (4\text{-}26)$$

The temperature T_{sun} is the black body temperature of the sun, which may be approximated to be between 6 000 and 5 762 Kelvin [119]. The apparent surface temperature of the sun is 75% of the sun's black body temperature, hence the 4/3 term added to the temperature ratio in Equation 4-28

[118, 120]. The second-law efficiency may then be determined using Equation 4-27, which provides an effective means of determining the performance of the receiver.

$$\eta_{2nd} = \frac{\Delta\Psi_{\mathrm{w}}}{\Phi_{sun}} \tag{4-27}$$

The associated irreversibility is defined as the negative of the summation of the changes in exergy as presented in Equation 4-28.

$$\bar{I} = -1 \times (\Delta\Psi + \Delta\Phi + \Delta\mathrm{W}) \tag{4-28}$$

4.3 Experimental setup

An experimental setup was constructed to test the performance of a cavity receiver under realistic environmental conditions. Since the solar receiver was the central focus of analysis, a test facility was designed to mimic the surrounding components of the Rankine power cycle.

A flow diagram that describes the layout of the test facility is presented in Figure 33, where the main components and measurement sensors of the test facility are numbered accordingly. In order to mimic the actual conditions of a Rankine cycle, the test facility comprises five sections: the pressure system, the solar tracker, the modular dish, the solar receiver and the measurement devices. As stated in Section 2.4, the combination of the modular dish reflector and the solar receiver is referred to as the solar collector.

Considering the flow diagram, the pressure and flow rate of the steam through the process tubing was controlled by the pressure system. All the process tubing on the solar tracker (including the receiver coil) had an outer diameter of 13.26 mm and an inner diameter of 8.6 mm. Municipal water was pressurised in the water reservoir by feeding compressed air into the top of the reservoir at a regulated pressure. This allowed for a degree of control over the supply pressure from the receiver. The flow rate of this steam was then controlled by expanding it through a needle valve.

The solar tracker orientated the solar collector towards the sun by adjusting its azimuth and elevation angles using rotary motors connected to a 24 V DC power supply. The modular dish comprises six smaller dish facets that work independently to concentrate the sun's direct normal irradiance towards a calibrated focal point. The solar receiver is the primary heat exchanger of the power cycle, where municipal water is heated and later superheated along the length of the receiver coil by the sun's concentrated rays. The receiver's aperture was positioned at the calibrated focal point of the modular dish to maximise the intercept factor at the aperture.

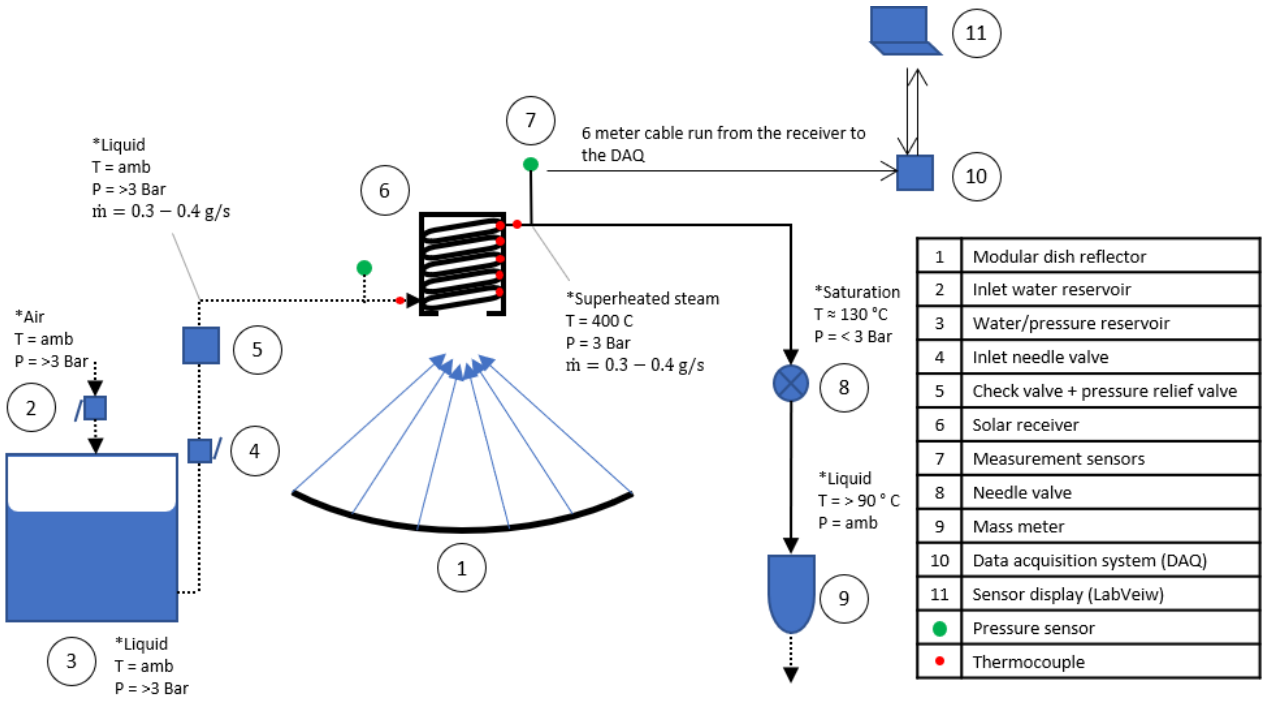

Figure 33: Schematic representation of the experimental test facility layout

An important aspect of this study is to ensure that superheated vapour leaves the receiver, since it would prove difficult to determine the quality of saturated steam, and thus the working fluid enthalpy and exergy at the outlet of the receiver. In addition, most commercial expansion units, such as axial and radial turbines, as well as piston generators, need the working fluid to be received in single-phase in order to prevent deterioration of the unit. This is with the exception of certain volumetric expanders, described in Chapter 2, that are able to operate without component deterioration when receiving two-phase working fluid.

4.3.1 Pressure system

A 12-bar compressed air line was used as the pressure supply for the experiments. An air regulator was connected between the air supply line and the water reservoir, using a pneumatic hose as presented in Figure 34. This was done to have tight control over the supply pressure of the superheated steam coming out of the receiver for the purpose of experimentation. Two 10-bar Honeywell pressure transmitters were placed in line at the inlet and outlet of the receiver coil to determine the pressure states of the water or steam at the inlet of the receiver and the superheated steam at the outlet.

The temperature of the superheated steam coming out of the receiver was far beyond the temperature limit of the pressure transmitter. Special attention was therefore paid to extend the pressure transmitter away from the primary flow. This was done using a U-shaped thermal syphon

that would capture the steam condensate and provide a static barrier between the outlet pressure transmitter and the process steam. This static barrier would function as a heat sink, whereby the heat being conducted from the process flow through the static condensate would be transferred to the environment through convection. An illustration of the U-shaped thermal syphon is presented in Figure 35. The process inlet and outlet pipes extend outwards from the figure.

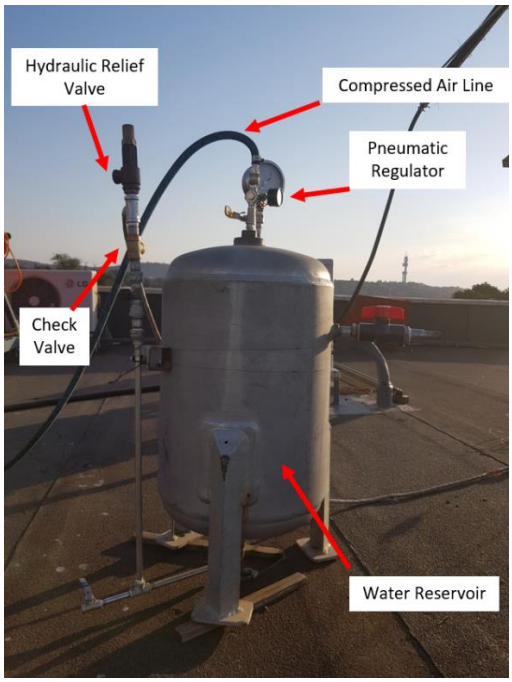

Figure 34: Water reservoir used during experimental testing

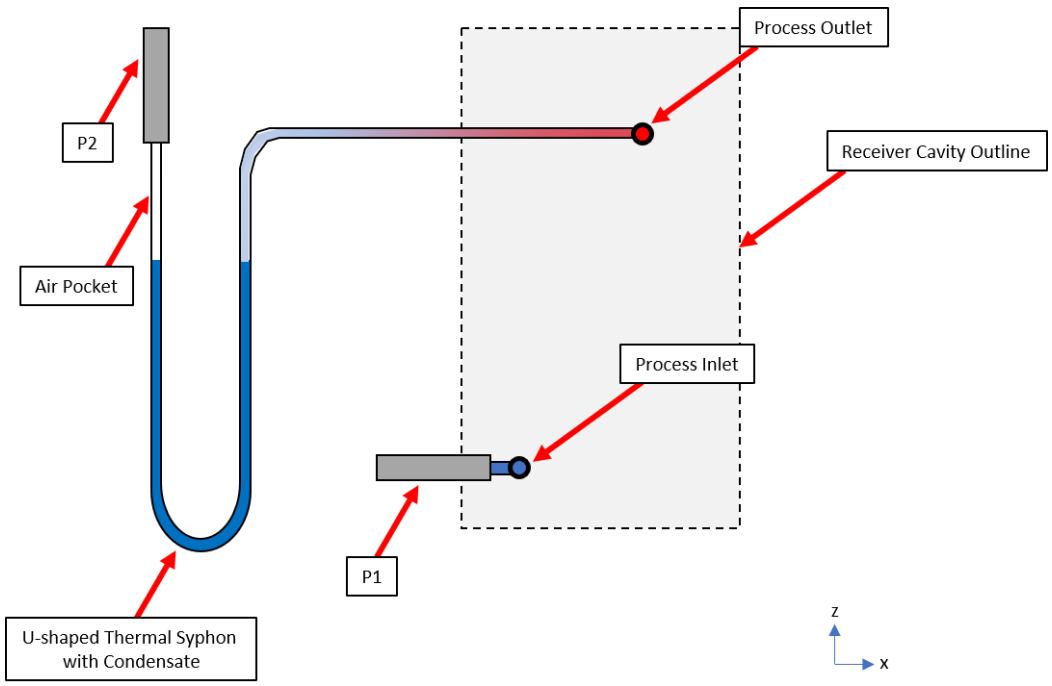

Figure 35: Schematic of the U-shaped thermal syphon and the inlet and outlet pressure transmitters

The steam was then expanded through a needle valve and passed into a hydraulic accumulator just above atmospheric pressure, as presented in Figure 36. The accumulator was a steel container with an inlet at the bottom and an overflow pipe with an aperture 200 mm above the inlet. As the steam bubbled through the water in the accumulator, it condensed into liquid, and the water level inside the accumulator rose until it flowed into the overflow pipe. As an added measure, a stainless steel mesh, placed above the accumulator, would capture any escaping steam and transfer it back into the contained water. The overflow pipe channelled the overflow into a mass meter container. The mass meter was a secondary container that was attached to a load cell. This ensured that shock from the collapsing steam bubbles was mitigated from the load cell readings, and the liquid mass accumulation over the testing period could be determined accurately.

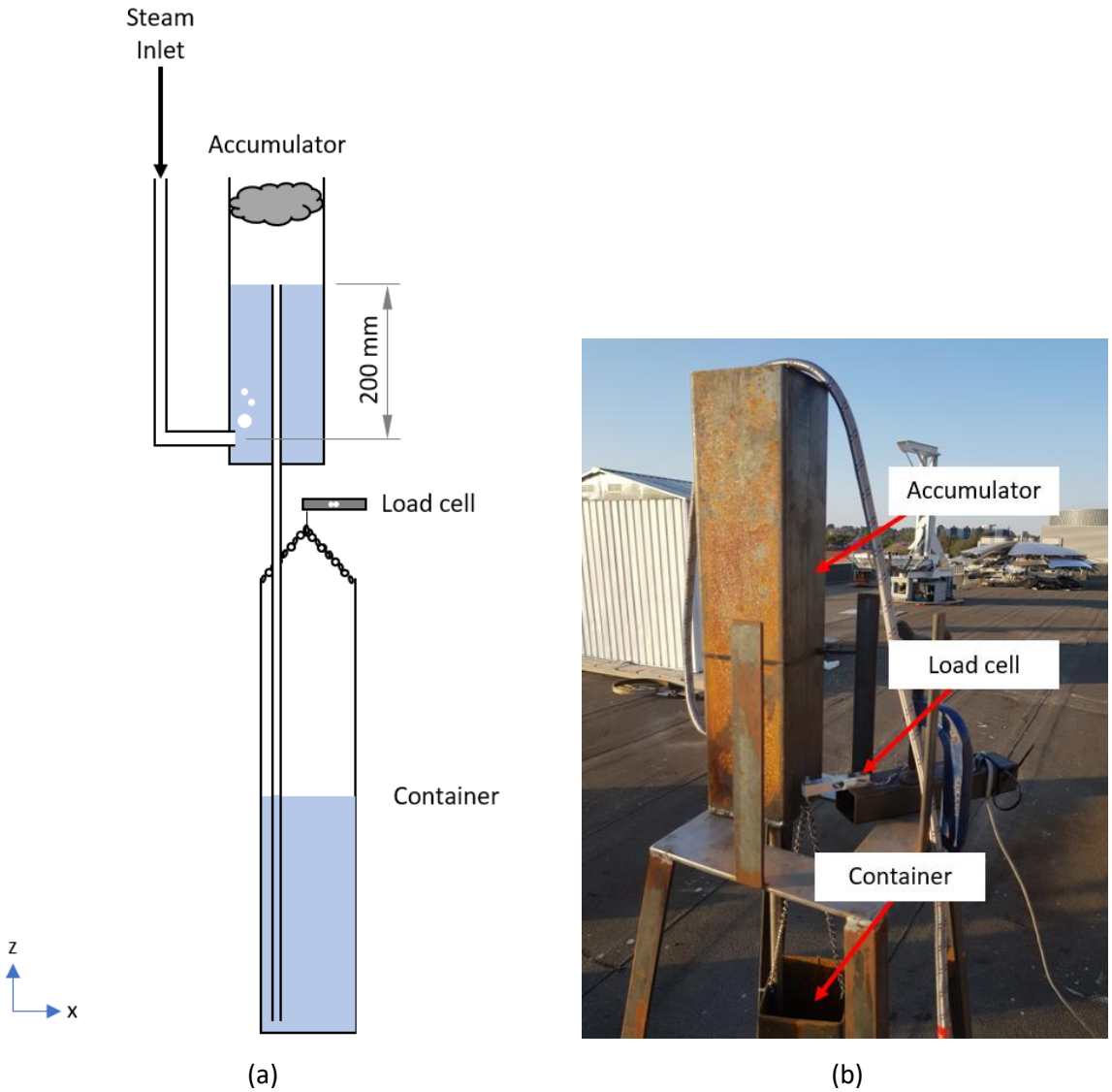

Figure 36: (a) Schematic of liquid mass meter; (b) Experimental liquid mass meter

4.3.2 Solar tracker

The solar tracker, described in Section 3.4.1, was used to orientate the solar collector towards the sun during the experimental testing days.

The tracking of the sun was performed manually for the purpose of the experiments, but an automatic tracking method could be implemented, as discussed in the literature study. A simple visual tracking technique was used, whereby a directional pinhole, attached to the tracker, let a finite amount of sunlight through it. This light was projected onto a flat, semi-transparent target surface with a calibrated centre point as shown in Figure 37. The pinhole light was kept within a certain radius from the centre point on the target surface in order to maintain a tracking accuracy below 1°.

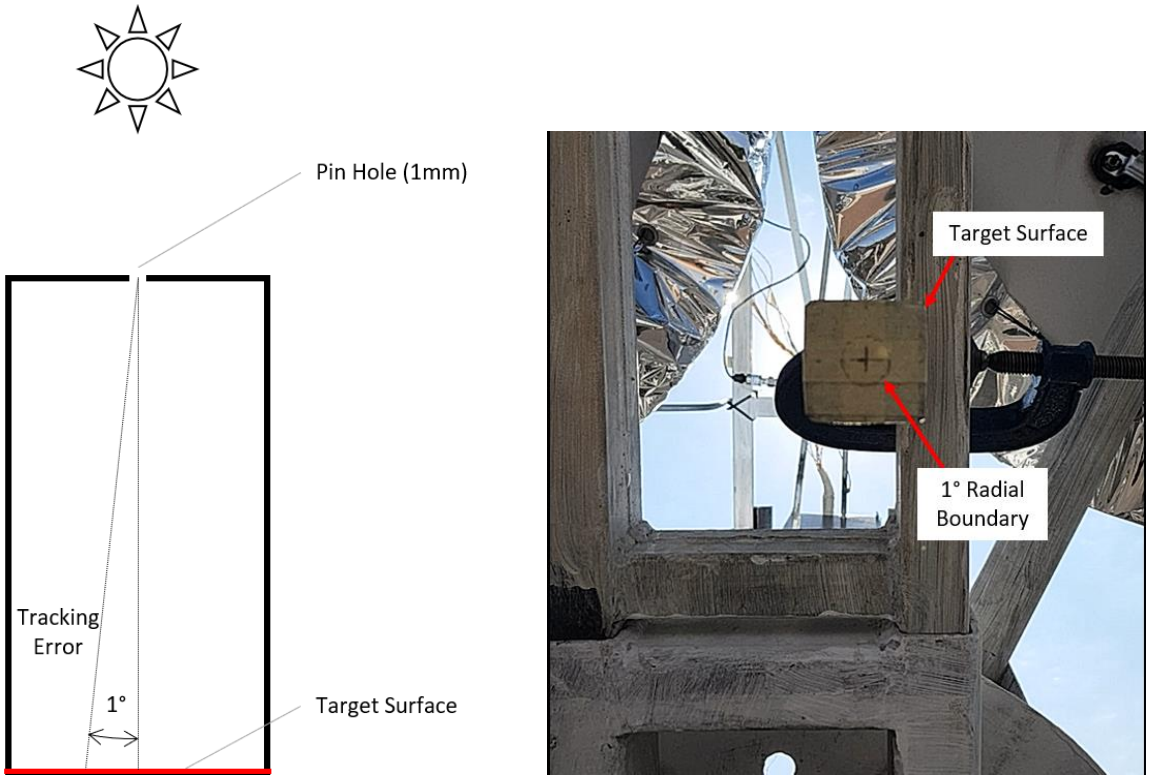

(a) (b)

Figure 37: (a) Schematic of the pinhole tracker used to track the sun within 1° of accuracy; (b) Pinhole sun tracker during testing.

Since the length of the tracking device was 300 mm, the projected pinhole light would have to be kept within a 5.24 mm circumference on the target surface for the tracker to have an accuracy below 1°. The tracking error is calculated using Equation 4-29 as

$$TrackError = \tan^{-1}(5.24/300) \approx 1° \quad (4\text{-}29)$$

Modular dish

The novel dish reflector described in Section 3.4.1 was used in the experimental analysis. Specific attention was paid to ensure that the facets kept their calibrated positioning and alignment from the moonlight tests to recreate the image at the aperture during the solar tests. It is important to note that the pressure within each facet cavity in its vacuum state was not recorded during the moonlight testing. The same pressure was therefore not achieved during the solar tests. Rather, an optimal image was projected onto the receiver by visual inspection.

4.3.3 Solar receiver

A receiver coil had already been constructed at the University of Pretoria. Its dimensions were considered appropriate for the current study. The receiver coil had a uniform helical section at its base and a conical section at its top, as presented in Figure 38.

The uniform helical section had an outer diameter of approximately 150 mm with a pitch of 13.26 mm and 12 coil turns along the helix. The conical section was welded onto the uniform helix, and the outer diameter reduced from 150 mm to approximately 90 mm in four coil turns. The conical section was expected to capture any intercepted radiation that was incident at the top of the cavity. The inlet and outlet process tubing extended from the outer diameter of the uniform helical section by 200 mm.

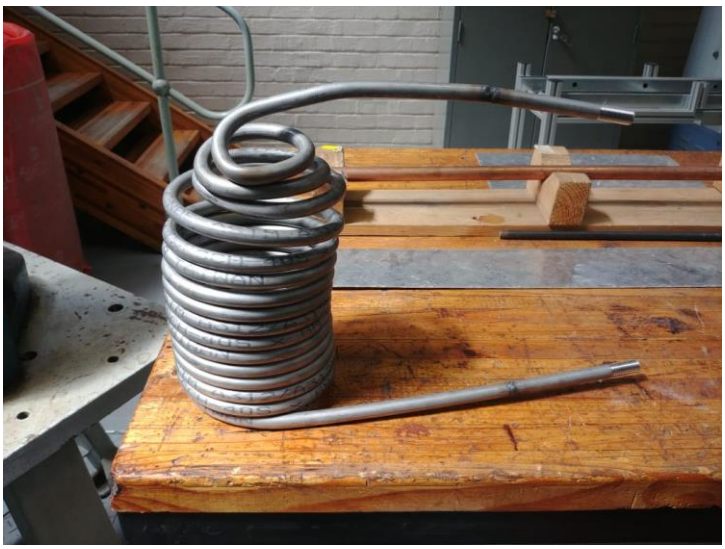

Figure 38: Constructed receiver coil

In order to measure the fluid temperature within the receiver, eight K-type thermocouple probes, with probe diameters of 3 mm each, were inserted at every second turn of the receiver coil, starting at the first turn located near the inlet. Two K-type thermocouple probes were also inserted at the inlet and outlet of the coil. The junctions of the thermocouples were positioned exactly at the centre of the coil

tube to obtain precise measurements relative to the flow at the centre of the coil tube. The probes were held and sealed using 1/8 inch stainless steel compression couplings that were welded onto the outer surface of the tube. K-type surface thermocouples were welded onto the inside and outside of the helical coil at the coil turns shown in Figure 39. The surface thermocouples estimated the temperature gradient over the diameter of the coil.

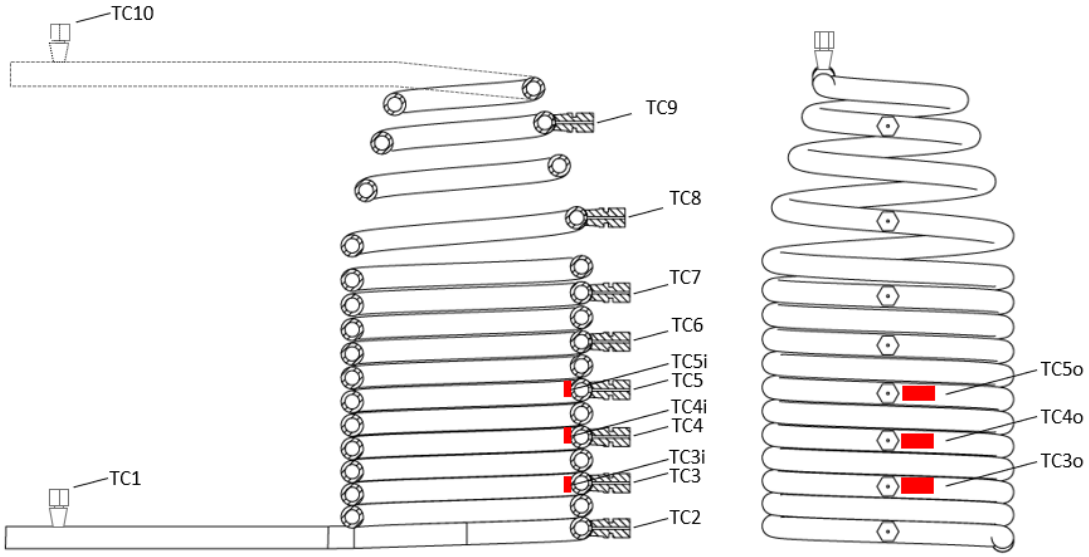

Figure 39: Thermocouple placement on the receiver coil

A hydraulic pressure test was performed on the receiver coil and the process piping described in Section 4.3.1, where the piping was filled with water and taken to a pressure of 8 bar for two hours to check for leaks. Furthermore, a pneumatic pressure test was conducted on the receiver and process piping, where the pressure was increased to 4 bar for two hours. Once all tests were passed, the receiver was determined to be ready for testing.

The receiver cavity comprised a rectangular prism-shaped, mild steel supporting frame with 0.5 mm aluminium sheeting adhered and riveted to the supporting frame to create an airtight seal. The receiver cavity was mounted to the receiver arm through the mounting holes located near the aperture of the receiver. Den Braven fire sealant was used to adhere the aluminium sheet to the supporting frame. The cavity aperture and the cavity lid were not sealed with the aluminium sheeting. The lid of the cavity receiver allowed for the insertion of the cavity insulation and the receiver coil. The lid was a 3 mm thick mild steel rectangular plate that could be screwed to the supporting frame using 5 mm butterfly screws. The cavity insulation comprised 25 mm ceramic fibreboard and ceramic wool fibre, used as a filler. In total, 25 mm of ceramic fibre board covered the receiver coil, with an added 25 mm at the back and top of the cavity to serve as a channel for the thermocouple leads. The cavity

aperture was 135 mm in diameter with a 60° chamfer that served as a wind guard. An illustration of the receiver cavity is presented in Figure 40.

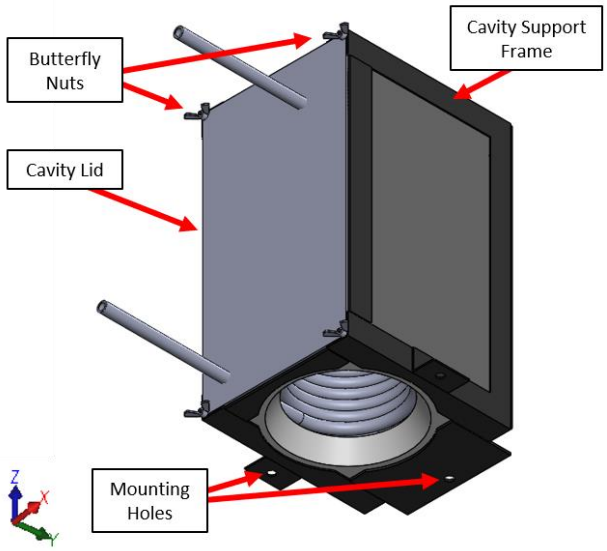

Figure 40: Illustration of the receiver cavity

The receiver cavity was constructed in such a way that two layers of 25 mm ceramic fibre insulation could be packed into the top and back sections, and a single layer could be packed into the remaining sections, as depicted in Figure 41.

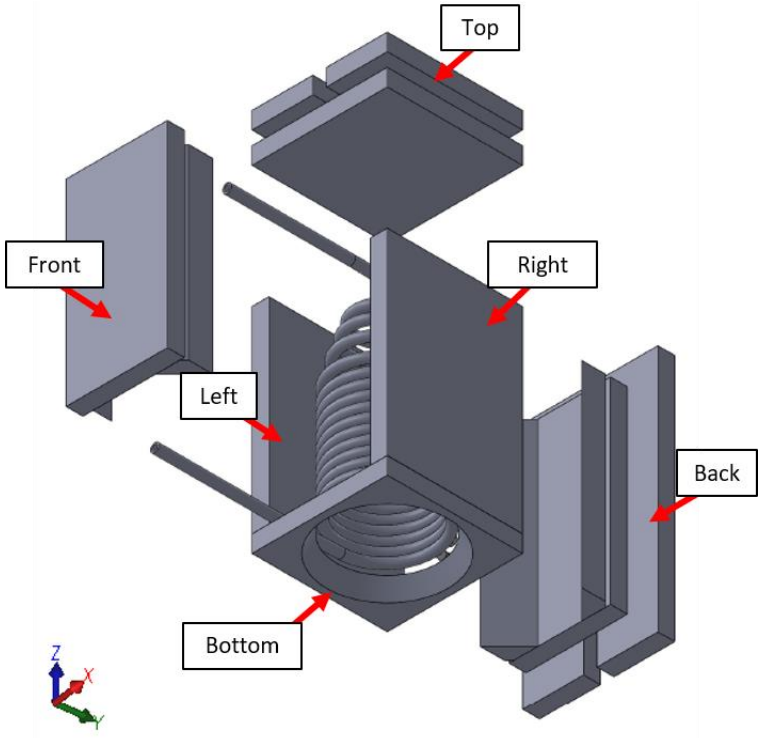

Figure 41: Exploded view of the receiver cavity depicting the sections of insulation

4.3.4 Weather and solar irradiance measurement

A crucial component of the experimental analysis was the measurement of the solar irradiance present during the period of testing. The irradiance and ambient temperature measurements were taken using a SOLYS 2 sun tracker, positioned on top of the Engineering Building I at the University of Pretoria as part of the SAURAN network [121]. The SOLYS tracker was estimated to have a measurement accuracy of 2% [122]. The wind direction and velocity at the experimental facility were measured using the Ambient Weather WS-100X-WiFi weather station, located adjacent to the solar collector.

4.4 Experimental method

The cavity receiver was tested on a clear, sunny day. The solar tracker was adjusted manually to follow the path of the sun. The solar collector was orientated towards the sun so that all the reflected images from the dish reflector's facets could intercept the aperture, as presented in Figure 42. This was determined to be the ideal orientation of the collector with respect to the sun's position. The pinhole tracker was then fixed in place on the solar tracker with the light from the pinhole projected onto the cross-hairs of the target. As the sun moved across the sky, light from the pinhole tracker showed the degree of misalignment between the solar collector and the sun. The solar collector was adjusted manually to keep the pinhole tracker within the $1°$ tracking boundary, as stated in Section 4.3.2. This resulted in the collector having a tracker error of less than 1° during testing.

Figure 42: Collector oriented towards the sun during testing

The municipal water contained within the pressure reservoir was pressurised using regulated, compressed air, which allowed for a degree of control over the supply pressure at the inlet of the receiver coil. The water was then heated using the concentrated radiation from the modular dish and turned into steam. Further along the coil, the steam was superheated and passed through the outlet of the receiver.

With the receiver aperture positioned at the focal point of the modular dish, a near steady-state period was observed during testing, where the inlet and outlet temperature readings became constant. The K-type thermocouples placed throughout the coil length measured the temperature of the steam. Pressure sensors positioned at the inlet and outlet of the receiver coil measured the steam pressure. Using the temperature and pressure measurements, the energetic and exergetic states of the steam could be determined. The surface K-type thermocouples that were welded onto the inside and outside of the coil measured the wall temperature gradient of the coil tube. Once a steady-state irradiance period was determined, the supply pressure was increased, and the flow rate decreased until steady-state superheated steam was produced in the receiver.

Due to erratic oscillations in pressure observed during testing, it was decided that the supply pressure should be set lower than the initial target pressure in Table 1. A target supply pressure of 3 bar was thus used in the experiments with a target flow rate of 0.32 g/s.

4.5 Experimental results

In order to analyse the performance of the solar receiver, a steady-state period is required where the DNI, receiver temperature and pressure, and mass flow rate through the system are constant. This is done to mitigate any transiency in the experimental setup. Transiency during testing would lead to an inaccuracy in determining the performance of the receiver, since the performance of the receiver is dependent on the mentioned parameters, which are always changing.

On the testing date of 20 September 2019, the day was sunny and clear, with low wind velocities. A near steady-state period of 91 minutes was obtained, between 13:19 and 14:50, when the DNI, the receiver inlet and exit temperature and the steam mass flow rate were maintained at constant values within a specific tolerance. The wind was measured to flow at speeds between 0 and 3.9 m/s, with the direction oscillating in a full 360° range. Due to the design of the experimental setup, the receiver pressures oscillated between the set supply pressure and a maximum, which meant that a true steady-state could not be reached. However, it was determined that an analysis could still be carried out for the given conditions, and the transiency during testing could be explained.

An observation was made during testing where only the first seven coil turns experienced incident radiation directly from the dish reflector. This is evident in Figure 43. From this observation, it is expected that thermocouple TC 5, which is positioned on the seventh coil turn, should have the highest average temperature of the 16 coil turns if the cavity temperature is lower than TC 5. This is because a net heat loss would begin to occur after the seventh coil turn, due to the temperature difference between the subsequent coil turns and the surroundings.

Figure 43: Incident solar radiation on the receiver coils during testing

4.5.1 Solar irradiance

The DNI had a slight negative gradient during the testing period, as shown in Figure 44. However, this was taken to be an acceptable decrement, since the irradiance only reduced by 12.5% over the entire period. An average reading of 757.13 W/m^2 was observed for the testing period.

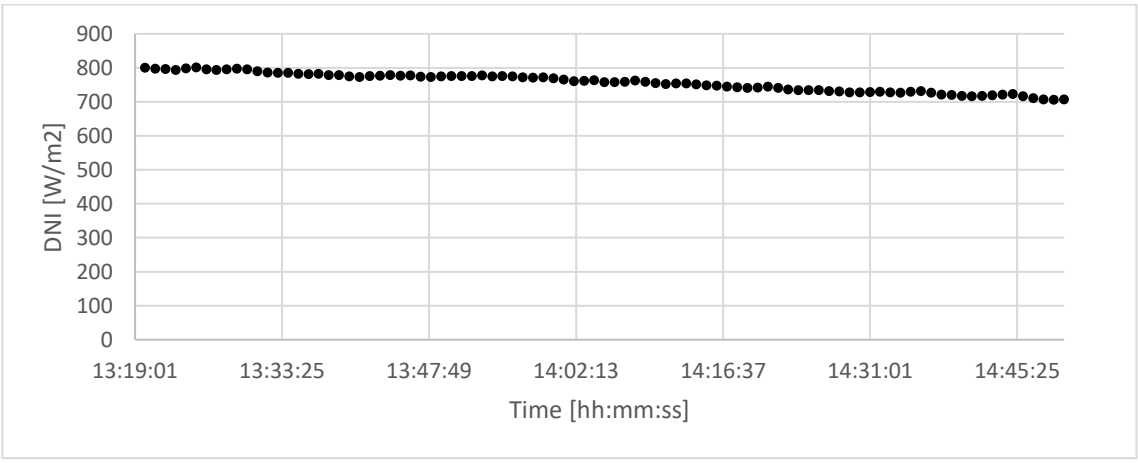

Figure 44: Direct normal irradiance measurements over the testing period

4.5.2 Mass flow rate

Figure 45 indicates that the mass accumulation of the condensate at the outlet over the 91 minutes followed a constant linear trend, with a gradient of 0.2938 g/s. The gradient of the linear trend represents the constant mass flow rate, with a 98% linear correlation.

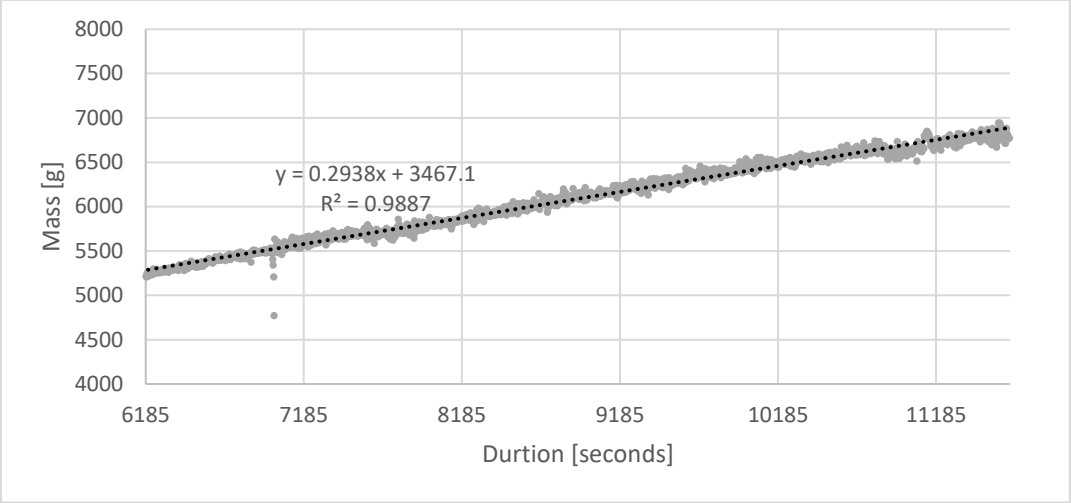

Figure 45: Mass accumulation at the outlet of the solar collector during the testing period

4.5.3 Pressure

A steady-state pressure condition could not be achieved during testing, as is evident in the plotted measurements in Figure 46. The pressure appeared to pulsate between the supply pressure at the minimum and a maximum of roughly 2.5 bar above the supply pressure. The period of pulsation ranged between 1.5 and 2 minutes. The supply pressure was set to 3 bar at the beginning of testing and then readjusted to 3.2 bar at 13:53:32, since a notable decrement was observed.

Another observation that can be made from these results is that the inlet pressure (P1) is slightly lower than the outlet pressure (P2). This is counter-intuitive, since a higher supply pressure is required to move the liquid through the coil towards the outlet, and the pressure transmitters were placed directly next to the inlet and outlet of the receiver. One could possibly attribute this trend to calibration error.

This does not necessarily nullify the measurements, since the pressure drop through the coil is expected to be negligible due to the low mass flow rate. An average pressure between P1 and P2 will be used to represent the pressure within the coil for the energy and exergy calculations. The average pressure between P1 and P2 oscillated between a maximum of 595 and 280 kPa. From these oscillations, the saturation temperature is expected to oscillate between a maximum of 158 and 131 °C.

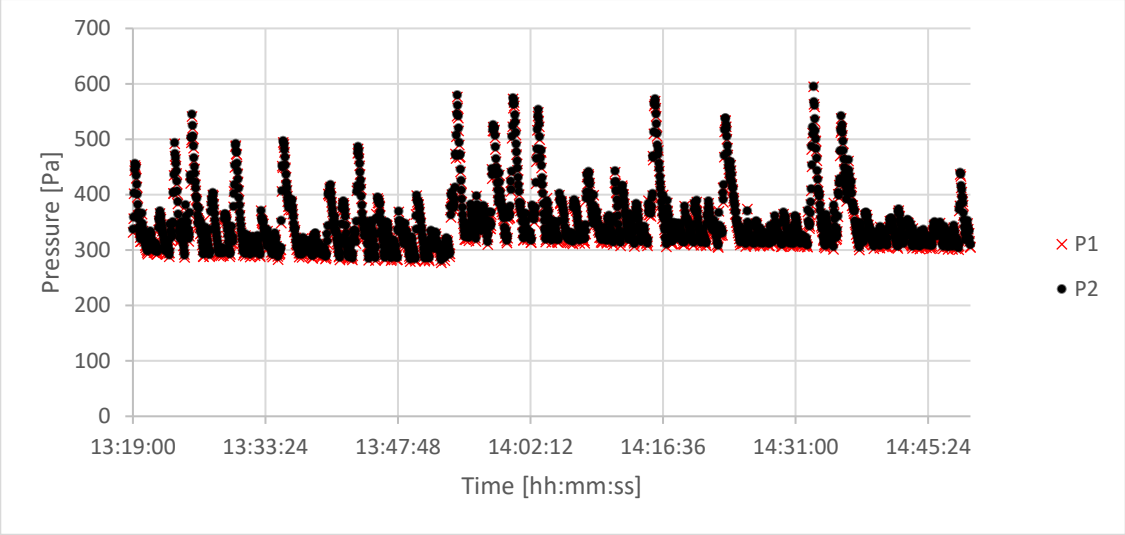

Figure 46: Pressure measurements taken over the testing period

4.5.4 Temperature

The temperature measurements taken during the testing period are graphically illustrated in the figures below. Some interesting observations were made of the results.

With regard to the measurement of the steam inside the receiver, the insertion thermocouple measurements, labelled TC 1 to TC 10, are plotted over the testing period in Figure 47. A summary of the results is presented in Table 15. A steady inlet temperature of 54 °C is observed at TC 1. As the water flows through the subsequent coil turns that are exposed to the concentrated solar radiation, the respective thermocouples measure an erratic oscillation in temperature. It may be observed that TC 3 primarily exists in the saturation region with an average temperature of 139 °C, after which the erratic oscillations continue until the temperatures stabilise after TC 7 to an average value of 355.17 °C between TC 7, TC 8 and TC 9.

Another interesting observation is that the average steam temperature after TC 6 decreases within the receiver until it reaches the outlet at TC 10, where the steam temperature rapidly decreases to an average temperature of 163.11 °C. The average coil surface temperature within the cavity was determined to be 315.80 °C by summating the time-averaged coil temperatures for TC 2 to TC 9 over their respective coil lengths.

The time-averaged temperatures of the steam are plotted along the coil length in Figure 48. Error bars show the 95th and 5th percentile of the measurement distribution around the given temperature averages. The plot shows the temperature oscillations that occur at TC 2, TC 4 and TC 5 and the sudden drop in temperature after TC 9.

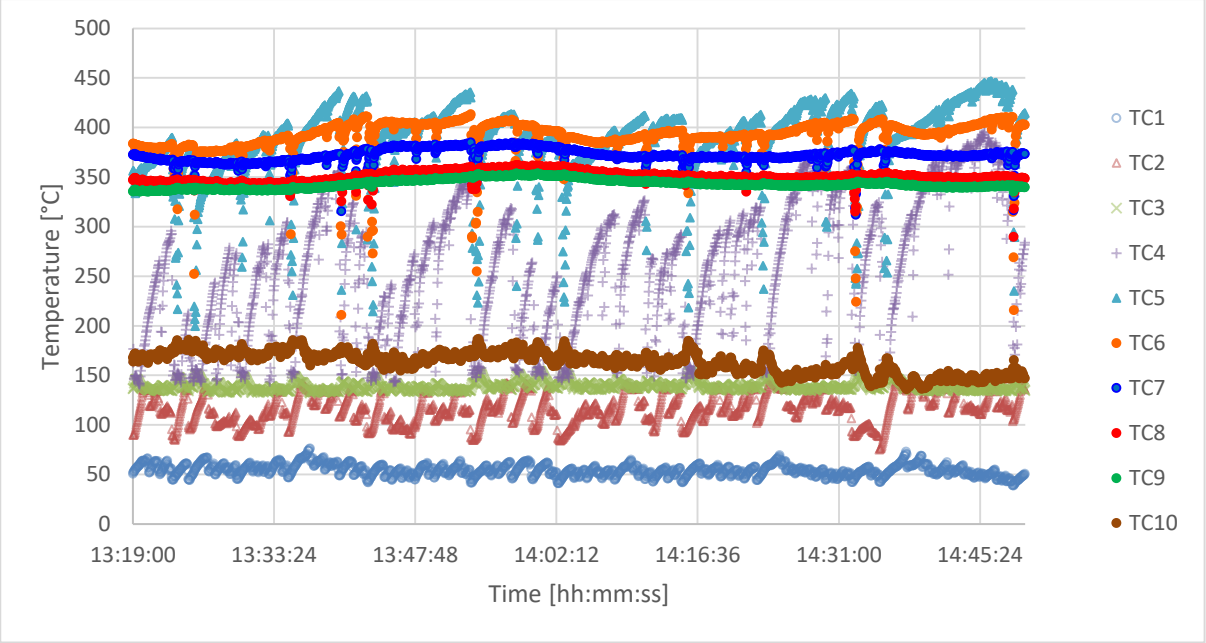

Figure 47: Insertion thermocouple measurements over the testing period

Table 15: Summary of insertion thermocouple measurements over the testing period

Thermocouple	Average (°C)	Maximum (°C)	Minimum (°C)	Standard deviation (°C)
TC 1	54.12	76.18	38.78	5.79
TC 2	117.00	147.61	75.00	15.00
TC 3	139.03	154.42	132.15	4.43
TC 4	258.10	395.69	139.72	68.72
TC 5	389.13	446.75	199.61	38.58
TC 6	391.54	413.47	211.01	17.64
TC 7	371.84	384.93	312.07	6.95
TC 8	350.56	362.01	289.60	5.54
TC 9	343.12	353.64	335.06	4.54
TC 10	163.11	186.47	135.87	10.91

Figure 49 presents the thermocouple readings of TC 4 and TC 5, and the average pressure reading between 14:10 and 14:30. The pressure appears to spike immediately after a temperature drop is measured in the thermocouples. The phenomenon is apparent in both the two large pressure pulsations, as well as in the smaller pressure oscillations.

The surface thermocouple measurements, along with their respective steam temperature measurements, are plotted in Figure 50 to Figure 52. A summary of the results is presented in Table 16. This was done to approximate the types of flow that were occurring in the coil turns.

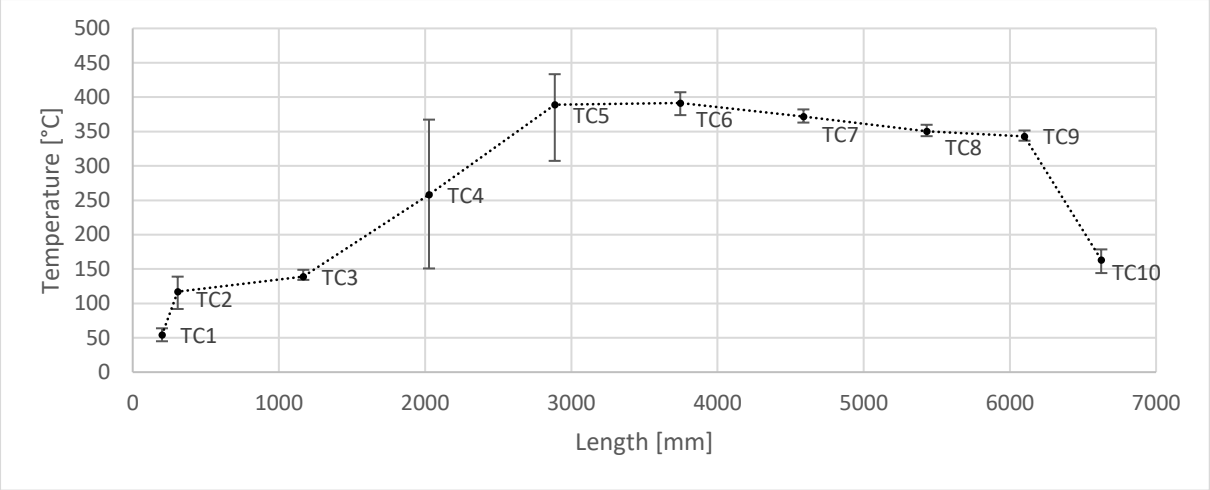

Figure 48: Time-averaged steam temperature readings along the length of the coil

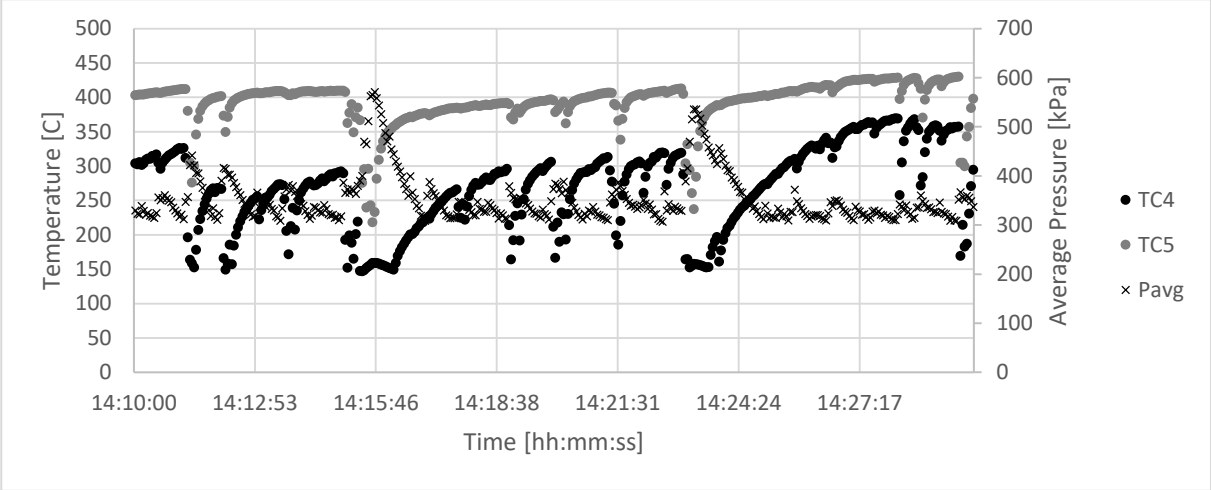

Figure 49: Temperature and pressure results between 14:10 and 14:30

Considering the surface temperature measurements in the third coil turn, illustrated in Figure 50, it may be observed that the inner coil wall temperature of TC 3i is notably larger than the outer coil wall temperature of TC 3o. A temperature difference of 89 °C between the inner and outer walls is observable from the averages in Table 16. The outer coil wall temperature is comparable to the fluid temperature of TC 3, which is at saturation temperature.

The temperatures in the fifth coil turn follow an erratic oscillation with the steam temperature frequently dropping towards saturation temperature and then spiking towards the measured wall temperatures. In certain instances, such as at 13:40:25, the temperature difference between the inner coil wall and the steam is roughly 180 °C. The temperatures of the inner and outer walls of the coil are grouped notably closer together when compared to the temperature in the third coil turn, and their average temperature difference is 30 °C.

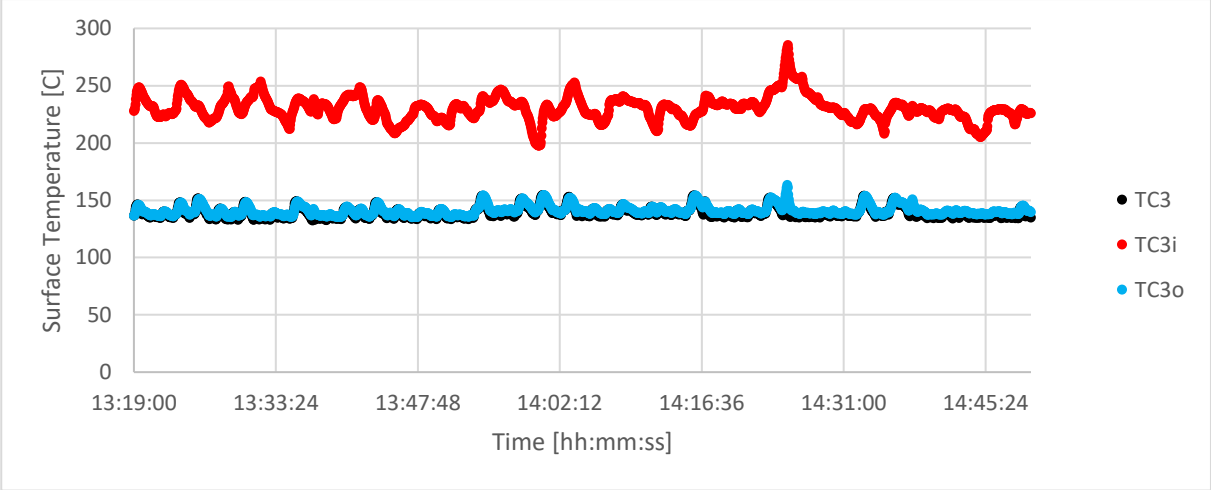

Figure 50: Steam and wall temperature measurements taken for the third coil turn

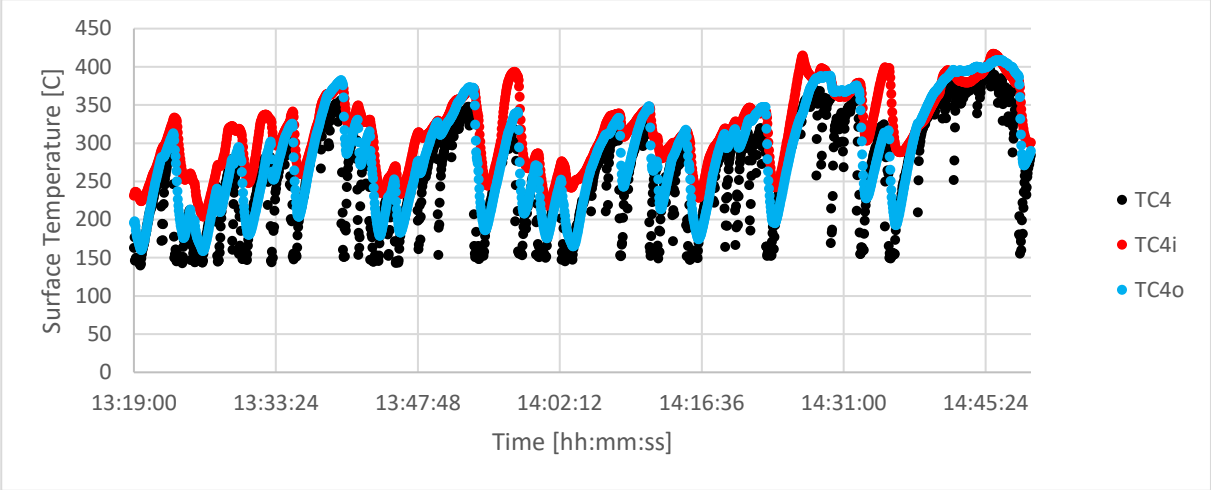

Figure 51: Steam and wall temperature measurements taken for the fifth coil turn

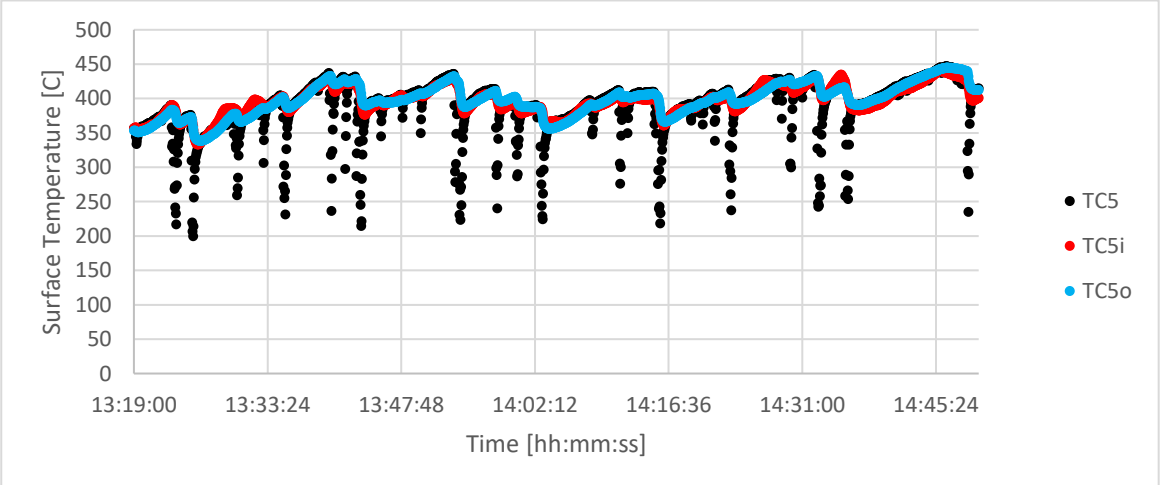

Figure 52: Steam and wall temperature measurements taken for the seventh coil turn

By the seventh coil turn, the oscillations in the inner and outer coil wall temperatures had begun to stabilise at average temperatures of 396 and 398 °C, respectively. There is now a negative difference of 2 °C between the inner and outer coil wall temperatures, which is counter-intuitive, since the inner wall is still receiving radiative heat from the concentrated solar radiation. However, the difference is so small that one could assume that the two walls are now uniform in temperature. There are still instances where the steam temperature drops towards saturation temperature. The maximum temperature difference between the steam and the walls is measured to be 177 °C.

Table 16: Time-averaged and statistical summary of the surface thermocouple measurements during the testing period

Thermocouples		Average (°C)	Maximum (°C)	Minimum (°C)	Standard deviation (°C)
TC 3	Inner	230.19	285.39	197.65	10.61
	Fluid	139.03	154.42	132.15	4.43
	Outer	140.74	163.42	135.19	4.16
TC 4	Inner	315.91	416.70	203.76	50.12
	Fluid	258.10	395.69	139.72	68.72
	Outer	286.05	408.40	158.48	67.07
TC 5	Inner	396.49	440.16	332.95	21.03
	Fluid	389.13	446.75	199.61	38.58
	Outer	397.62	444.71	338.35	23.36

4.6 Discussion

4.6.1 Flow within the coil

The pressure oscillations were determined to come from the rapid expansion of steam, since the pressure spikes occurred directly at the time that TC 4 and TC 5 measured a sudden drop in temperature towards saturation (see Figure 49). Based on the literature study conducted, this suggests that a slug type flow was occurring (see Figure 8). As a new slug of liquid passes into the fourth coil turn, a temperature drop towards saturation temperature is measured. As the liquid comes into contact with the higher temperature walls, it rapidly expands into steam. This rapid expansion causes a spike in pressure, which, in turn, closes the check valve at the inlet. Thus, the only way for the flow to escape is through the needle valve at the outlet, which is set at a constant aperture.

The temperature oscillations that are measured between TC 2 and TC 5 suggest that this coil region is dealing with two-phase flow. At TC 2, it is suspected that bubbly flow is occurring (see Figure 8), where the fluid temperature spikes towards saturation temperature as the water begins to boil. A vapour

bubble encapsulates the thermocouple junction, and then suddenly drops as the junction comes into contact with the fluid again. The oscillations become more erratic after TC 3 and then subside by TC 6, which suggests that superheated steam was being produced by the eleventh coil turn and the flow was mostly single phase.

Based on the observations made of the surface temperature readings in Figure 50 to Figure 52 and the literature study conducted on two-phase flow regimes in helically coiled tubes, a hypothesis may be made as to what type of flow is occurring in each coil turn at the point of measurement. Figure 53 to Figure 55 illustrate the author's estimation of the flow regimes that are occurring in the coil turns during the testing period.

In the third coil turn, a temperature difference of 89 °C was observed between the average temperatures of the inner and outer walls. The temperature of the fluid was comparable to that of the outer wall. This suggests that dryout was initiated before this point and the coil turn mostly experienced stratified flow where expanded steam passed through the inner coil wall nearest to the helical axis. Saturated liquid was in contact with most of the outer wall inside the coil tube and enveloped the thermocouple junction. The flow stratification is suspected to be a result of the rapid expansion of steam on the inner side of the coil tube due to the incidence of solar radiation. Since the flow rate is so low, at 0.29 g/s, it is suspected that centrifugal forces play a negligible role in this stratification. This would result in the notable temperature difference that was observed.

The fifth coil turn had an interesting phenomenon, where the steam temperature measurements oscillated between saturation and the inner coil wall temperature of TC 4i. Based on this observation, it is estimated that intermittent, slug-type flow was occurring. During such an oscillation, the drop in fluid temperature suggests that a slug of saturated liquid is in contact with the insertion thermocouple junction. The temperature difference between the saturated liquid and the inner wall of the coil tube was observed to be greater than 120 °C in certain instances. According to the literature study, this suggests that Leidenfrost boiling had been initiated by this point. This is why the flow pattern illustrates the liquid slug not being in contact with the walls of the coil tube.

By the seventh coil turn, it was suspected that Leidenfrost boiling had become fully initiated with both the inner and outer coil tube walls having a temperature difference of 177 °C in respect of the saturated liquid slugs. Thus, Figure 55 illustrates a flow pattern where wet steam accumulates on the insertion thermocouple junction, but does not come into contact with the coil tube walls due to the Leidenfrost effect. This explains the sudden drop in steam temperature, while the tube wall temperatures experience a negligible effect.

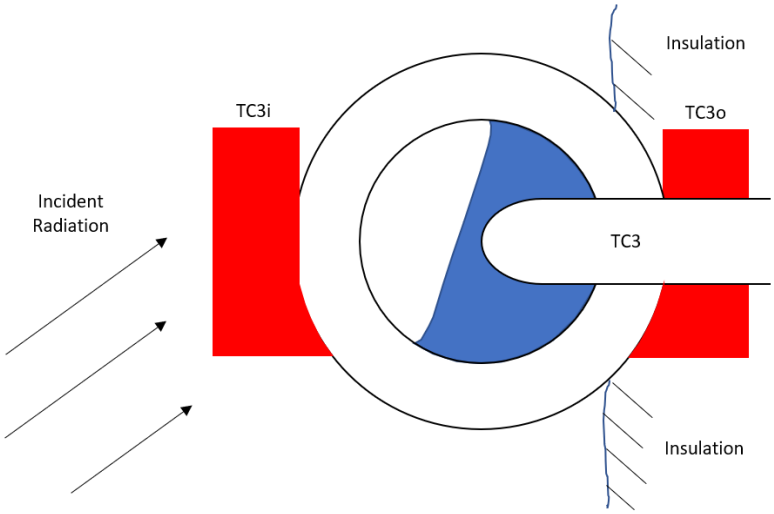

Figure 53: Cross-section of the third coil turn during the testing period

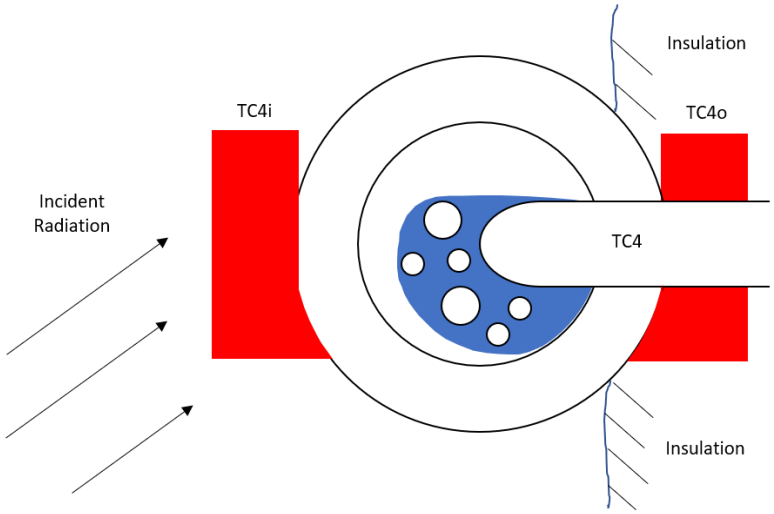

Figure 54: Cross-section of the fifth coil turn during the testing period

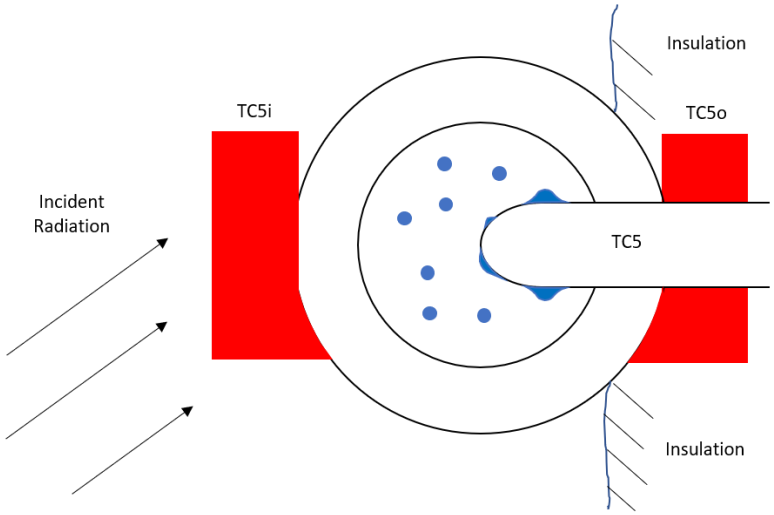

Figure 55: Cross-section of the seventh coil turn during the testing period

4.6.2 Power generation and first-law efficiency

The thermal efficiencies of the solar receiver and the solar collector were determined based on equations 4-6 and 4-7, and are plotted in Figure 56 and Figure 57. The inlet temperature to the receiver was taken to be at TC 1, while the outlet of the receiver was considered to be at TC 9, since TC 10 was not insulated. The slight decrement in temperature between TC 7 and TC 9 is considered to be the result of the intercepted radiation only being incident on the first seven coil turns, as was observed in Figure 43. The notable temperature drop between TC 9 and TC 10 is considered to be due to convection heat loss from the process piping outside the receiver cavity. The slight decrement in the DNI resulted in an increase in both thermal efficiencies, since the inlet and outlet steam temperatures were effectively constant over the 91-minute period. Considering the reflectivity of the reflector to be 97% (see Section 3.2) and the intercept factor at the 135 mm diameter aperture to be 87% (see Section 3.4.4.1), the collector was able to produce an average of 861 W from the incident solar radiation of 2 068 W. The average receiver and collector efficiencies were 49% and 42% respectively. This meant that, of the total solar radiation incident on the solar dish facets, 42% could be captured through the coils. Of the total concentrated radiation that was intercepted through the receiver aperture, 49% could be captured through the coils.

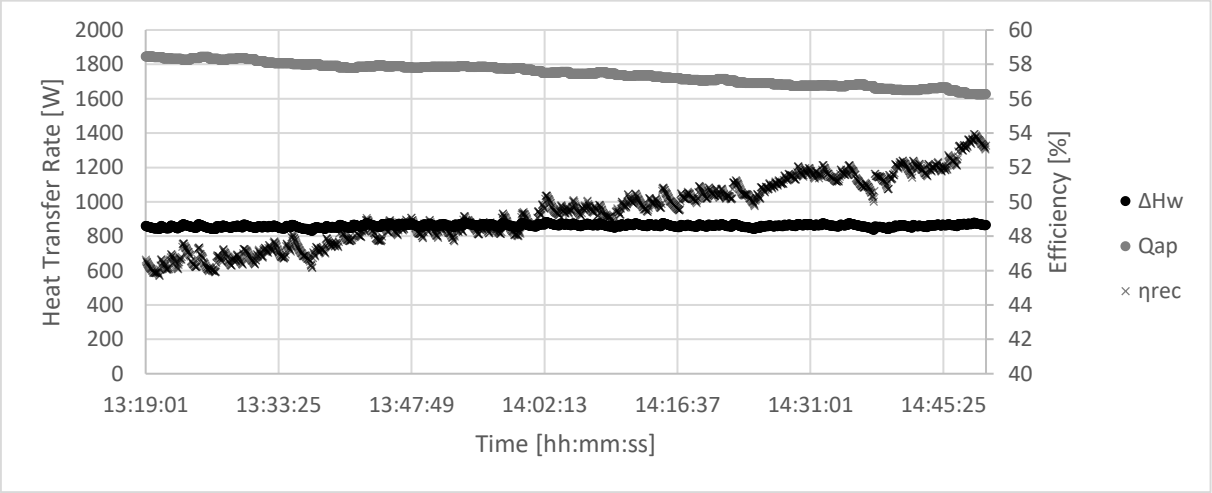

Figure 56: Power generation from the steam and receiver's first-law efficiency over the period of testing

It is suspected that the amount of intercepted radiation at the aperture, determined using Equation 4-4, does not equate to the total amount of radiation incident on the coils. This is because a wind skirt was used with a chamfer of approximately 60° (see Figure 31), which may have caused additional unforeseen spillage at the aperture. This means that an overestimation of the intercept factor may have occurred. It is therefore recommended that future tests should take this additional

mechanism of spillage into account when determining the intercept factor for the experimental receiver. This may be done by considering a smaller effective aperture for a given aperture size or developing a ray tracing numerical model that is validated by the moonlight tests, and then using it to better approximate the true intercept factor for the experimental receiver, modelled in the software.

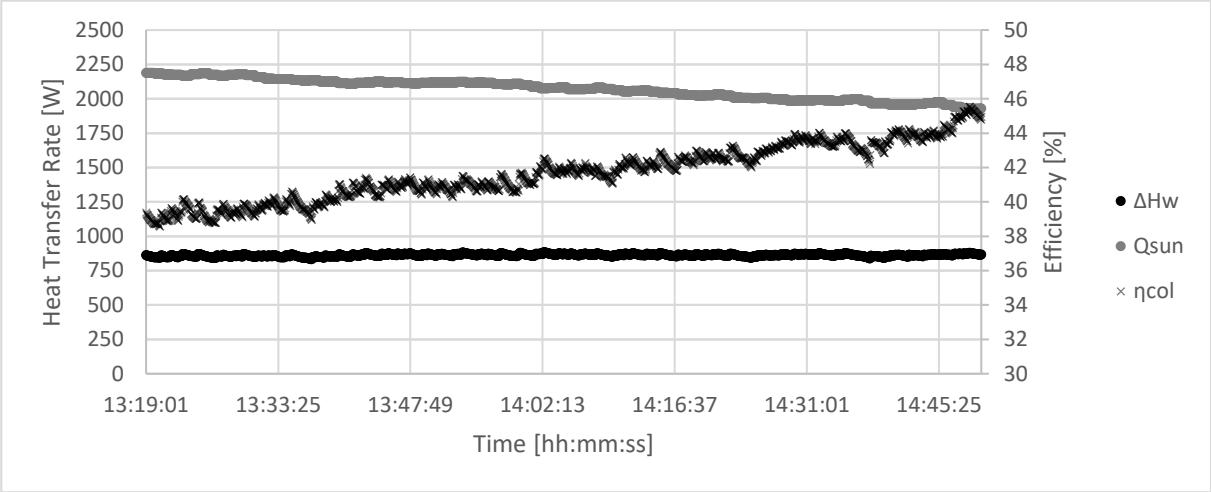

Figure 57: Power generation from the steam and collector's first-law efficiency over the period of testing

4.6.3 Heat loss

According to the results in Figure 56 and Figure 57, the thermal losses within the cavity contribute notably to the efficiency of the solar collector and the receiver. From the lunar flux analysis, it was determined that a larger receiver aperture would lead to an increased intercept factor, but conversely, a larger receiver aperture would also lead to an increase in thermal loss. Since the intercepted heat and the captured heat are known, the heat loss from the receiver was determined using Equation 4-2. This is plotted in Figure 58. The average heat loss from the receiver was determined to be 884.47 W over the testing period. Based on the heat loss model presented in Section 4.2.3, the heat loss was broken down into its fundamental components to aid in characterising the performance of the receiver.

4.6.3.1 Convection heat loss

The natural convection heat loss through the aperture was modelled by considering the Nusselt number correlations of Koenig and Marvin [68] and Stine and McDonald [43], presented in equations 2-38 and 2-41, respectively. The solar collector's elevation angle was measured to be 40° on average during the testing period. The average ambient temperature was measured to be 29.64 °C during the testing period, with a measured average wind velocity of 1.71 m/s. Considering the receiver aperture diameter to be 135 mm with a cavity inner diameter of approximately 150 mm and a cavity

average surface temperature of 315.80 °C, the convection heat loss was determined. The results are presented in Table 17.

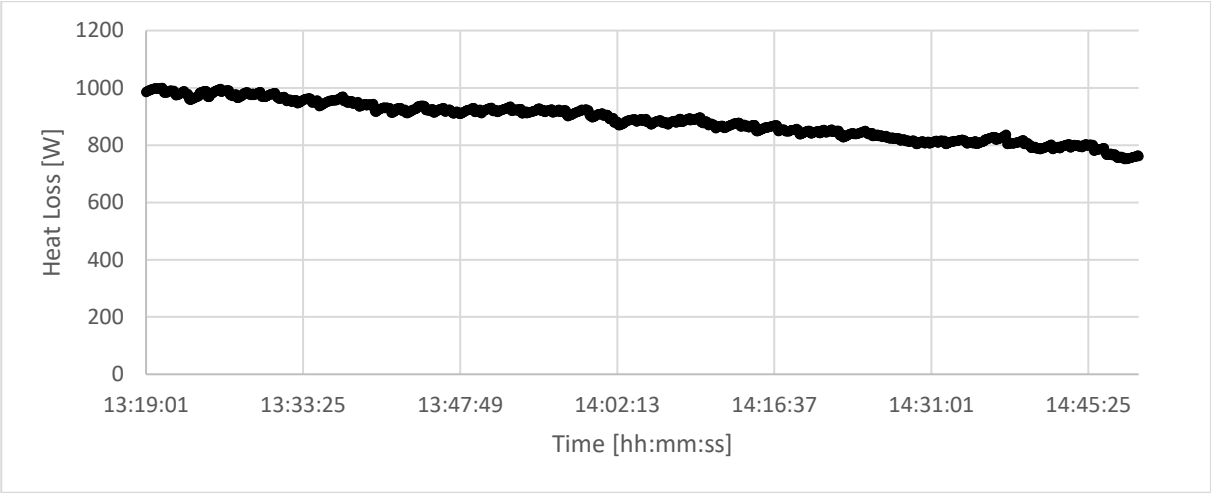

Figure 58: Heat loss from the receiver over the period of testing

Table 17: Results of the Nusselt number calculations for natural convection heat loss through the receiver aperture

Parameter	**Value Equation 2-38**	**Value Equation 2-41**	**Units**
Characteristic length (L_c)	9.55E-02	0.2	m
Property temperature (T_{prop})	461.68	302.79	K
Grashof number (Gr)	3.44e6	2.11e8	-
Prandtl number (Pr)	0.70	0.71	-
Coefficient (ϑ)	0.43	-	-
Coefficient (s)	-	0.46	-
Nusselt number ($Nu_{natural}$)	4.39	25.54	-
Convection coefficient ($\bar{h}_{natural}$)	1.72	3.40	W/m^{2}K

There is a notable discrepancy between the correlations of Koenig and Marvin [68] and Stine and McDonald [43]. This discrepancy becomes even more apparent when considering the fact that the natural convection heat loss for the Stine and McDonald correlation is calculated using a larger surface area than that of Koenig and Marvin (see Section 4.2.3.1). Since the Koenig and Marvin correlation was modelled for cavity receivers with surface temperatures higher than 550 °C, the heat transfer coefficient from the Stine and McDonald correlation, presented in Equation 2-41, was considered.

Since the wind speeds were below 4.5 m/s, the forced convection heat transfer coefficient was approximated to be twice that of the natural convection heat transfer coefficient, based on the work

of Harris and Lenz [72]. The correlation of Ma [71] was not considered, since it was modelled for a specific set of operating and geometric conditions.

4.6.3.2 Radiation heat loss

The view factor between the inner cavity and the aperture was determined by approximating the inner cavity as a cylinder with a conical top. A schematic of the simplified inner cavity is presented in Figure 59. The inner cavity diameter was adjusted to be the inner coil diameter rather than the diameter of the insulation walls. This better approximates the view factor between the exposed coil tube and the aperture. The view factor between the inner cavity and the aperture was determined to be $F_{s-ap} \approx F_{2,4-1} = 0.17$.

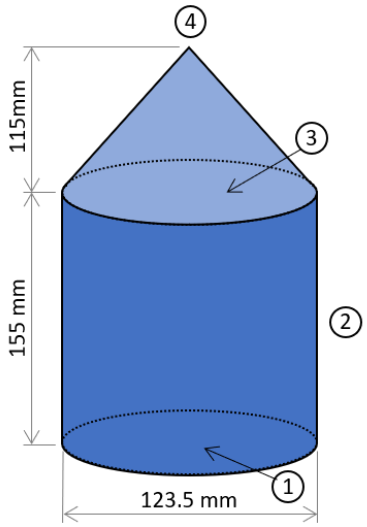

Figure 59: Simplified inner cavity surface for determining view factors

The radiation heat loss from the aperture was determined using Equation 4-11. The temperature of the surroundings was approximated to be equivalent to the ambient temperature. The emissivity of the surroundings was estimated to be 1. The average emissivity and absorptivity of the receiver cavity were estimated to be equivalent to that of the stainless steel coil in the receiver. This assumption was considered to be appropriate since the concentrated solar radiation was only incident on the first seven coil turns closest to the receiver aperture. However, the approximation is expected to over-predict the reflected radiation. This is because it does not account for the directional reflectance of the incident radiation within the cavity. The coil tubes were considered to have the optical properties of thermally oxidised stainless steel (oxidised for 10 minutes at 1 043 K under atmospheric conditions), which has a solar absorptivity of 0.85 [123]. The emissivity of the coil tubes was estimated using the work of Cengel and Ghajar [48]. For lightly oxidised stainless steel at 326.85 °C, which is comparable to the surface temperature of the coil tube in the experimental cavity, the emissivity was reported to

be 0.3. At the average surface temperature of 315.80 °C, the total reflected radiation and emitted radiation were determined to be 262.39 W and 65.30 W, respectively.

4.6.3.3 Conduction heat loss

The total conduction heat loss was broken up into heat loss components for each wall of the cavity (see Figure 41) according to Equation 4-30.

$$\dot{Q}_{cond,loss} = \dot{Q}_{loss,front} + \dot{Q}_{loss,back} + \dot{Q}_{loss,top} + \dot{Q}_{loss,bottom} + \dot{Q}_{loss,left} + \dot{Q}_{loss,right} \quad (4\text{-}30)$$

The thermal conductivity of the ceramic fibre board insulation was provided by the manufacturers as a function of temperature and is presented in Figure 60 [124].

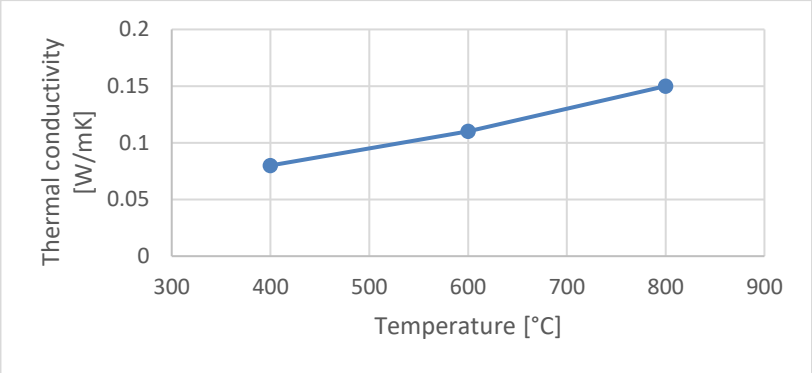

Figure 60: Thermal conductivity of ceramic fibre as a function of temperature [124]

The conduction heat loss was determined through an iterative process presented in Figure 61. The inner cavity temperature ($T_{ins,in}$) was approximated to be equivalent to the average coil surface temperature. An initial estimate of the outer cavity temperature ($T_{ins,out}$) was made, being the average temperature between the inner cavity temperature and the ambient temperature.

Using the outer cavity temperature and the ambient temperature, the film temperature was determined, which was then used to determine the properties of the air near the outer cavity surface. Using the correlations described in Section 4.2.3.3, the Nusselt number for natural and forced convection on each of the sides of the outer cavity wall was determined. Due to the solar collector being orientated roughly at 45° to the wind direction for most of the testing period, Equation 4-16 was used to describe the forced convection heat loss from the cavity sides. The total heat loss was then determined for each of the outer cavity sides using the combined Nusselt numbers for forced and natural convection. Using the total heat loss rate, a new iteration of the outer cavity surface temperature was determined for each outer surface using Equation 4-31. The process was repeated

until an iteration change of 0.001 °C was noted for the surface temperature of the outer cavity. A summary of the solution to the conduction heat loss analysis is presented in Table 18.

$$T_{ins,out} = T_{ins,in} - \dot{Q}_{cond,loss} \times \frac{t_{ins}}{k_{ins} A_{ins,in}} \quad (4\text{-}31)$$

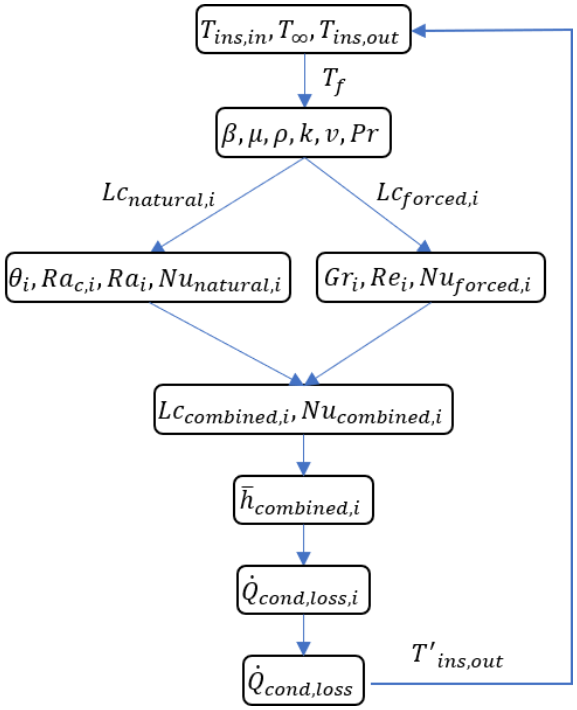

Figure 61: Conduction heat loss solution methodology

4.6.3.4 Discussion of heat loss

The heat loss modes are summarised in Table 19 and Figure 62. It is evident from the summary that convection heat loss is the dominant mode present for the given receiver design, with 45% relative heat loss. This is expected, since the aperture of the receiver, with an aperture diameter of 135 mm, was larger than the inner diameter of the uniform helical coil section (123.5 mm). This meant that the receiver experienced the maximum convection loss possible for its given elevation angle. A smaller aperture diameter would have led to a decrease in convection heat loss. This larger aperture also led to a notable amount of incident radiation being reflected from the receiver aperture. The reflected radiation is notable, due to the fact that concentrated radiation was only incident on the first seven coil turns and was primarily incident on the lower surfaces of the tube sections due to the incident angle of the intercepted radiation. This was the basis on which the simplifying analytical assumptions were made in Section 4.2.3.2.

Table 18: Results of conduction heat loss analysis

Description	Symbol	Value						
		Front	Back	Left	Right	Top	Bottom	Unit
Conduction heat loss								
Insulation surface temperature	$T_{ins,out}$	358.13	333.35	350.80	350.80	322.87	335.84	K
Film temperature	T_f	330.46	318.07	326.80	326.80	312.83	319.32	K
Surface area (inner cavity)	$A_{ins,in}$	0.04	0.04	0.04	0.04	0.02	0.01	m^2
Surface area (outer cavity)	$A_{ins,out}$	0.07	0.07	0.08	0.08	0.05	0.02	m^2
Insulation thickness	t_{ins}	0.025	0.05	0.025	0.025	0.05	0.025	m
Forced convection								
Characteristic length (forced)	$Lc_{forced,i}$	0.28	0.28	0.28	0.28	0.2	0.2	m
Grashof number	Gr	2.01E+08	2.39E+08	2.11E+08	2.11E+08	9.10E+07	8.29E+07	-
Reynolds number	Re	2.21E+04	2.36E+04	2.25E+04	2.25E+04	1.72E+04	1.66E+04	-
Nusselt number	$Nu_{forced,i}$	82.26	85.65	83.24	83.24	77.57	76.14	-
Convection coefficient (forced)	$\bar{h}_{forced,i}$	8.32	8.39	8.34	8.34	10.60	10.58	W/m^2K
Natural convection								
Elevation angle	θ	40	40	90	90	60	60	deg
Angle of inclination	φ	50	50	0	0	30	30	deg
Characteristic Rayleigh number	$GrcPr$	7.22E+07	-	-	-	3.00E+08	-	-
Characteristic length (natural)	$Lc_{natural,i}$	0.37	0.37	0.37	0.37	0.25	0.25	m
Grashof number	Gr	1.67E+08	1.10E+08	1.52E+08	1.52E+08	2.49E+07	3.74E+07	-
Rayleigh number	Ra	1.17E+08	7.72E+07	1.07E+08	1.07E+08	1.76E+07	2.64E+07	-
Nusselt number	$Nu_{natural,i}$	55.73	47.00	56.97	56.97	17.89	38.70	-
Convection coefficient (natural)	$\bar{h}_{natural,i}$	4.37	3.57	4.42	4.42	1.96	4.30	W/m^2K
Total heat loss								
Combined Nusselt number	$Nu_{comb,i}$	87.80	88.53	89.03	89.03	77.70	78.11	-
Combined characteristic length	$Lc_{comb,i}$	0.30	0.29	0.30	0.30	0.20	0.20	m
Combined convection coefficient	$\bar{h}_{comb,i}$	8.38	8.41	8.41	8.41	10.60	10.63	W/m^2K
Conduction heat loss rate	$\dot{Q}_{cond,loss}$	32.14	17.79	33.15	33.15	9.58	6.63	W

The total heat loss using the analytical model was estimated to be 841.96 W. The average experimental heat loss was determined to be 884.47 W, as stated in the introduction. When comparing the heat loss model to the experimental results, the heat loss model underpredicts the experimental heat loss by 5%. This is considered sufficiently accurate for analysis.

Table 19: Heat loss breakdown using the convective heat loss correlation of Stine and McDonald [43]

Description	**Symbol**	**Heat loss rate (W)**	**Relative heat loss**
Convection heat loss	$\dot{Q}_{loss,conv}$	**381.83**	45.35%
Natural convection loss through aperture	$\dot{Q}_{conv,natural}$	127.28	
Forced convection loss through aperture	$\dot{Q}_{conv,forced}$	254.55	
Radiation heat loss	$\dot{Q}_{loss,rad}$	**327.69**	38.92%
Radiation emitted from the coils	$\dot{Q}_{rad,emit}$	65.30	
Radiation reflected from the cavity	$\dot{Q}_{rad,ref}$	262.39	
Conduction heat loss	$\dot{Q}_{loss,cond}$	**132.44**	15.73%
Conduction loss from the front of the cavity	$\dot{Q}_{cond,front}$	32.14	
Conduction loss from the back of the cavity	$\dot{Q}_{cond,back}$	17.79	
Conduction loss from the left of the cavity	$\dot{Q}_{cond,left}$	33.15	
Conduction loss from the right of the cavity	$\dot{Q}_{cond,right}$	33.15	
Conduction loss from the top of the cavity	$\dot{Q}_{cond,top}$	9.58	
Conduction heat loss from the bottom cavity	$\dot{Q}_{cond,bottom}$	6.63	
Total theoretical heat loss	$\dot{Q}^{*}_{loss}$	**841.96**	**100%**
Experimental heat loss	$\dot{Q}_{loss}$	**884.47**	**-**

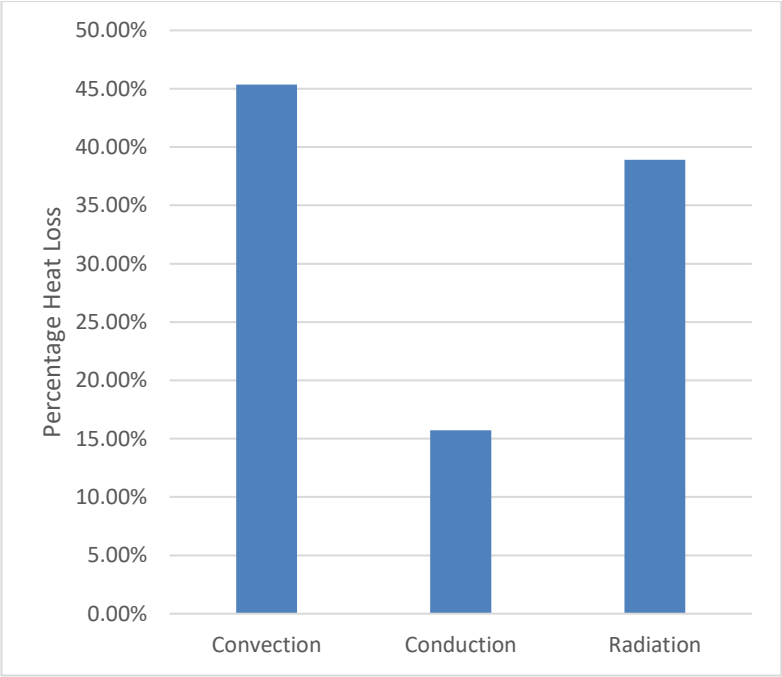

Figure 62: Relative heat loss from the receiver

Some of the heat loss components could easily be mitigated by improving the collector design. The reflected radiation can be minimised by increasing the focal length of the dish reflector or modifying the optical properties of the receiver shape and coil surface. The aperture diameter could be reduced to minimise the convection and radiation heat loss through the aperture. The conduction heat loss through the receiver walls could be minimised by increasing the insulation thickness. This can be done without decreasing the incident area of the dish reflector due to the spacing of the dish facets (see Figure 21a).

4.6.4 Aperture sizing

Since Table 19 shows that the total heat loss rate through the aperture accounted for roughly 84% of the total heat loss rate, it is important to determine how these losses could be minimised. The components of heat loss through the aperture were determined to be the radiation heat loss and the convection heat loss through the aperture. As mentioned in Section 4.6.3, one solution to reduce heat loss through the aperture is to modify the shape of the receiver. In this section, an analysis was carried out to determine the correlation between aperture size and heat loss through the aperture for the current set of operating conditions. An optimum aperture size is determined by identifying the turning point in the net heat transfer rate through the aperture for a given aperture size.

The heat loss model is considered to be valid for an intercepted radiation within a range of 1 625.69 W and 1 845.06 W since this was the total range of intercepted radiation that was present during the testing period. It is thus assumed that the conditions within the cavity remain constant for the given range. The intercepted radiation is determined by considering the average reflected radiation from the dish reflector during the experiments and the intercept factor trend determined in Section 3.4.4.1.

Figure 63 illustrates the correlation between the net heat transfer rate through the aperture as a function of the aperture size. The receiver aperture size was varied between a diameter of 0.12 m and a diameter of 0.175 m, which accounts for the valid intercepted radiation range. It is evident from the plot that the variation of the aperture does not produce an optimum since the net heat transfer rate levels out with the increase in aperture size. The levelling out of the net heat transfer rate is defined as the point where the absolute gradient drops below 0.5 W/mm. The net heat transfer rate is observed to level out at approximately 0.16 m. This means that no effective change will occur in the net heat transfer rate at the aperture for aperture sizes between 0.16 and 0.175 m. It also means that aperture size adjustments between 0.16 and 0.175 m will result in an increase of approximately 1% in the net heat transfer rate at the aperture when compared to the net heat transfer rate for an aperture size of 0.135 m, which is a negligible amount. The aperture optimisation method performed above was simply used to gauge whether the initial aperture design was adequate for the experiment. From

the analysis, it may be concluded that no adjustment of the aperture is required to notably optimise the net heat transfer rate through the aperture.

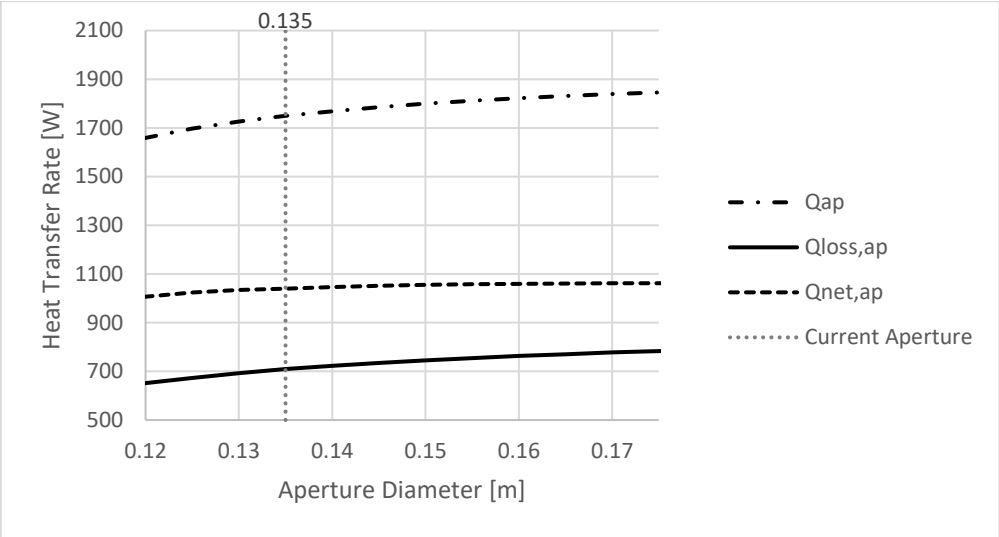

Figure 63: Aperture optimisation considering the net heat transfer rate through the aperture

4.6.5 Second-law analysis

An exergy analysis was performed on the receiver where the second-law efficiency was determined for the steady-state period. The results were plotted in Figure 64. The exergy of the steam at the inlet and outlet of the receiver was determined from Equation 4-23. The available work from the intercepted radiation was determined from Equation 4-26. The ambient temperature and ambient pressure measurements were taken using the SOLYS 2 Sun Tracker [121]. The sun's temperature was taken to be 5 762 K [48]. The average second-law efficiency was determined to be 12% over the testing period.

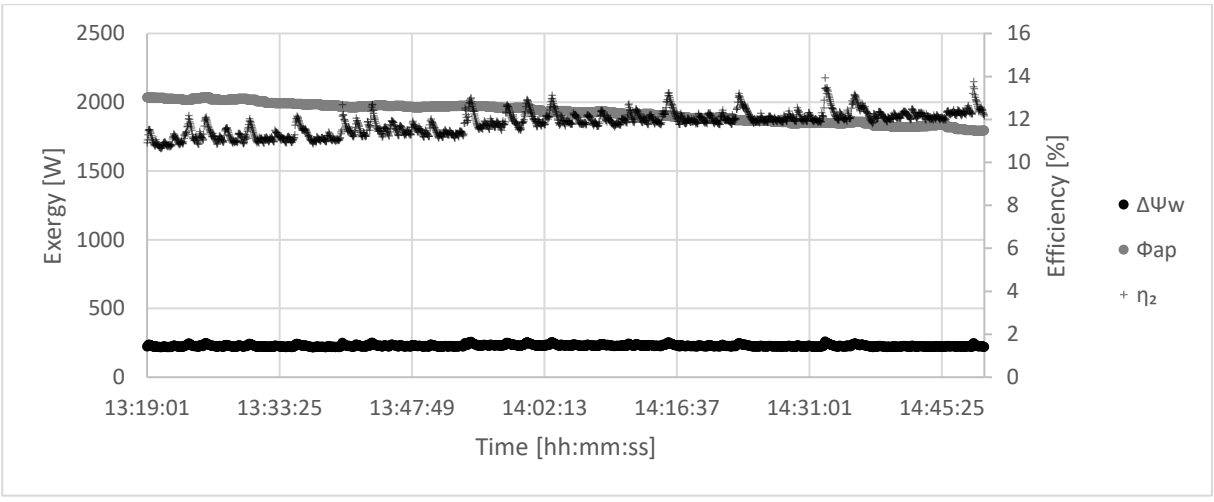

Figure 64: Second-law analysis of the solar receiver for the steady-state period

It is important to consider the irreversibility breakdown of the test facility in order to define the main contributors of irreversibility in the system. Figure 65 illustrates the different contributors of irreversibility that are considered in the current study.

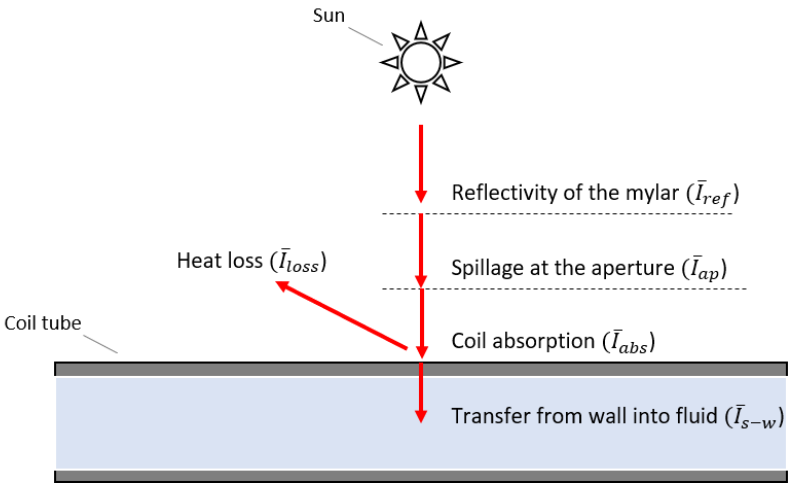

Figure 65: Contributors to irreversibility with the solar collector

The analysis can be further broken down into its first-law energy components and its respective second-law exergy components, as presented in Figure 66. As is evident in Figure 66a, the reflected radiation heat loss component is handled separately from the total heat loss from the receiver coil since the reflection occurs before the heat is absorbed by the coil. Once the heat has been absorbed by the coil, it is either transferred to the working fluid, causing a change in enthalpy, or it is released as convection, conduction or emitted radiation heat loss, which are dependent on the surface temperature of the coil. The exergy terms were determined using the second-law analysis model and are presented in Table 20, along with their respective equations used to determine the values. The dish reflectivity was taken to be 97% for the analysis, according to the UV/VIS spectroscopy test presented in Section 3.2. The intercept factor was taken to be 87% according to the results of the lunar flux testing presented in Section 3.4.4.1.

The main contributors to the irreversibility of the solar collector were then determined using Equation 4-30. The results are presented in **Error! Reference source not found.**. The total irreversibility of the solar collector was first determined to ensure that the irreversibility breakdown accounted for all possible component irreversibilities.

$$\bar{I}_{total} = -1 \times (\Delta\Psi + \Delta\Phi + \Delta W) \tag{4-28}$$

$$\bar{I}_{total} = -1 \times (\Delta\Psi_{w} - \Phi_{sun})$$

$$\bar{I}_{total} = -1 \times (227.12 - 1923.23)$$

$$\bar{I}_{total} = 1696.11\, W$$

The irreversibility contributions were determined by considering the specific components within the solar collector as control volumes and defining the exergy transfer in and out of each control volume. The equations used to calculate the irreversibilities are presented in equations 4-32 to 4-37.

$$\bar{I}_{ref} = -1 \times (\Phi_{\mathrm{ref}} - \Phi_{sun}) \quad (4\text{-}32)$$

$$\bar{I}_{ap} = -1 \times (\Phi_{ap} - \Phi_{ref}) \quad (4\text{-}33)$$

$$\bar{I}_{ap,ref} = \Phi_{ap,ref} \quad (4\text{-}34)$$

$$\bar{I}_{abs} = -1 \times (\Phi_{abs} + \Phi_{ap,ref} + \Phi_{loss} - \Phi_{ap}) \quad (4\text{-}35)$$

$$\bar{I}_{loss} = \Phi_{loss} \quad (4\text{-}36)$$

$$\bar{I}_{s-w} = -1 \times (\Delta\Psi_{\mathrm{w}} - \Phi_{abs}) \quad (4\text{-}37)$$

Table 20: Summary of the second-law exergy components

Exergy components	**Symbol**	**Surface temperature (T_s)(K)**	**Heat transfer rate ($\dot{Q}$)(W)**	**Exergy (W)**	**Equation**
Available work from the sun	Φ_{sun}	5 762	2 068.13	1 923.23	4-28
Available work from the reflected radiation	Φ_{ref}	5 762	2 006.09	1 865.53	4-28)
Available work intercepting the aperture	Φ_{ap}	5 762	1 745.30	1 623.01	4-28
Available work being reflected by the coil and lost through the aperture	$\Phi_{ap,ref}$	5 762	275.63	256.32	4-28
Available work being absorbed by the coil tube wall	Φ_{abs}	588.95	860.83	418.26	2-26
Available work being lost by the receiver	Φ_{loss}	588.95	608.83	295.82	2-26
Change in exergy of the steam	$\Delta\Psi_{\mathrm{w}}$	-	-	227.12	2-25

It is evident in **Error! Reference source not found.** that, along with the reflection loss and the heat loss irreversibilities contributing to 32.55% of the total irreversibility of the solar collector, the heat absorption in the coil makes the largest contribution to the total irreversibility, at a 38% contribution. This is due to the significant difference in surface temperature between the sun and the receiver coil. This irreversibility can be addressed by shifting the entire power cycle up in pressure and in temperature. However, this will conversely increase the heat loss irreversibility that is present.

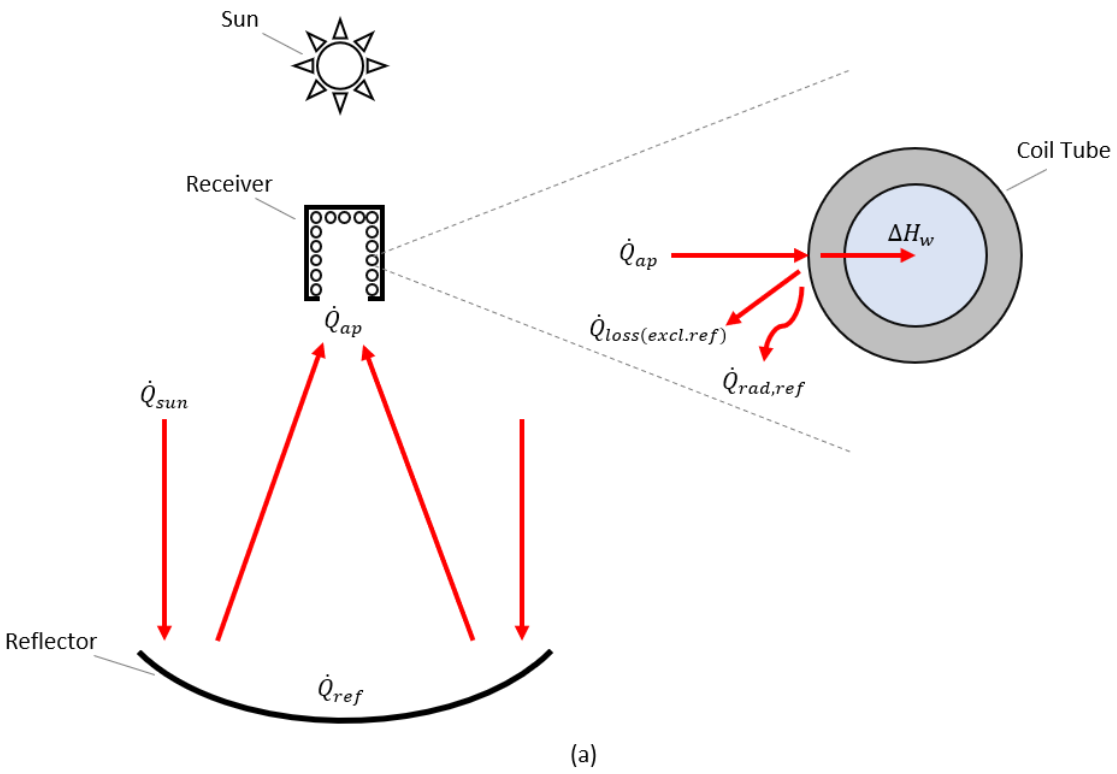

(a)

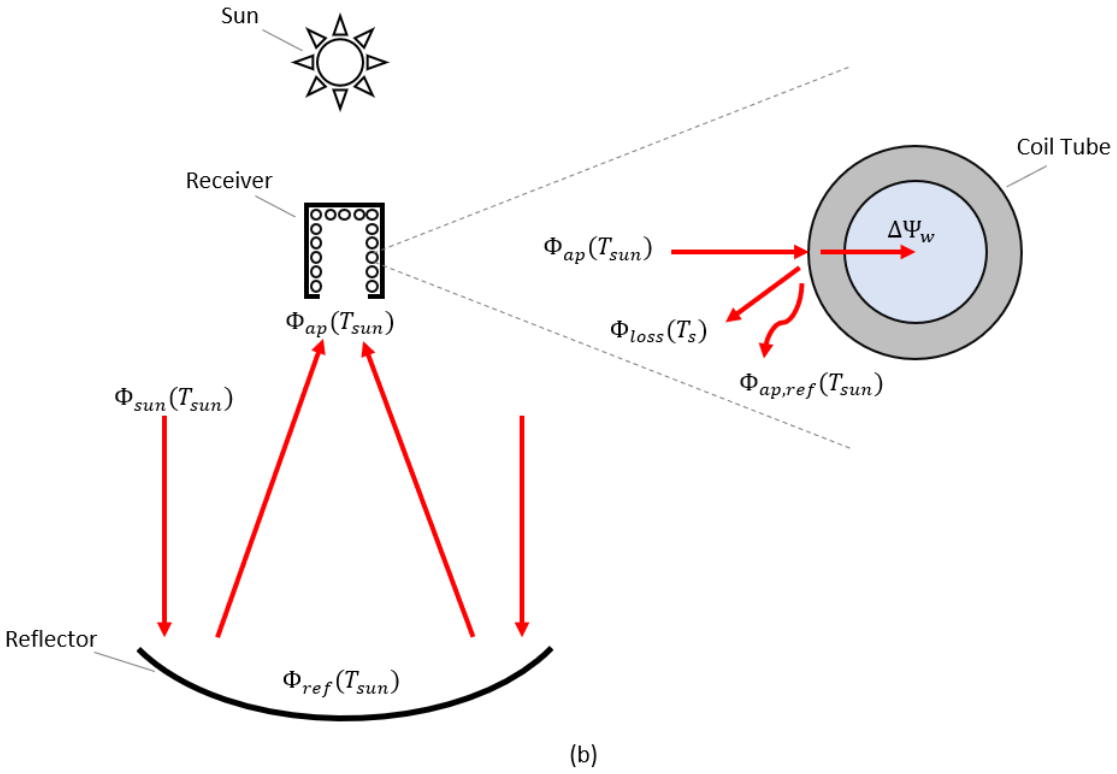

(b)

Figure 66: (a): First-law energy components; and (b) second-law exergy components

An optimum set of operating conditions can thus be determined with enough empirical information. Since the testing was only conducted for a single set of operating conditions, the optimum could not

be accurately determined. A parametric analysis, where the solar collector is analysed for varying operating conditions, is thus recommended for future work. The heat loss irreversibility can be addressed by optimising the collector design, as mentioned in Section 4.6.3.

Table 21: Irreversibility breakdown for the solar collector

Irreversibility contributors	**Symbol**	**Irreversibility (W)**	**Contribution**
The reflectivity of the Mylar sheet	$\bar{I}_{ref}$	57.70	3.40%
Spillage at the aperture	$\bar{I}_{ap}$	242.52	14.30%
Reflected radiation loss from the coil	$\bar{I}_{ap,ref}$	244.00	15.11%
Coil absorption	$\bar{I}_{abs}$	658.49	38.48%
Transfer from tube wall to working fluid	$\bar{I}_{s-w}$	191.14	11.27%
Thermal heat loss	$\bar{I}_{loss}$	302.26	17.44%
Total breakdown	$\boldsymbol{\bar{I}_{total}}$	**1 696.11**	**100%**

4.7 Conclusion

A thermal investigation of the designed solar collector was conducted on a clear, sunny day in order to characterise its thermal performance. It is important to determine the amount of heat that can be captured at certain operating conditions of the receiver in order to estimate the power potential of the associated micro-scale Rankine cycle. The solar receiver was positioned at the focal point of the solar reflector and the collector followed the sun throughout the testing period using the solar tracker.

During the testing period, steady inlet and outlet steam temperatures were achieved with municipal water being run through the receiver at 0.29 g/s at a supply pressure of 3 bar. The inlet temperature at TC 1 was kept steady at 54 °C and the outlet temperature at TC 9 was kept steady at 343.12 °C. The target supply pressure was determined to be 6 bar in Table 1, but the unforeseen pulsations that occurred caused the pressure in the receiver to rise by as much as 2.85 bar above the supply pressure. This resulted in the supply pressure being lowered during the experiments in the interest of safety.

With an average solar irradiance of 757 W/m^2 measured over the testing period and a reflector incident area of 2.73 m^2, the solar collector was able to capture 861 W of heat in the working fluid. The thermal efficiency of the collector was thus determined to be 42%, which is far from an ideal collector efficiency. It was suspected that additional spillage was not accounted for when determining the intercepted radiation at the aperture since a wind skirt was used, which may have interfered with the incident radiation. Thus, not all the radiation that was modelled to have intercepted the aperture would have been incident on the coils in the receiver. This would result in an overestimation of the total heat loss from the cavity. This should be addressed in future work by performing a numerical analysis using ray-tracing software. The numerical model can be validated by the moonlight tests and

should then be used to better approximate the intercept factor and the reflected radiation heat loss from the experimental receiver.

According to the results, a total heat loss rate of 884 W was determined. A heat loss model was developed that could predict the heat loss within 5%. According to the heat loss model, the main contributor to the heat loss rate in the receiver was the convection and radiation heat losses through the aperture. These components formed 84% of the total heat loss in the receiver. The loss components must be addressed in future work. Using the heat loss model and the intercept factor trend determined in Section 3.4, the aperture sizing was analysed. It was determined that an adjustment in the aperture diameter would produce a negligible change in the captured heat. The focus should rather be shifted towards adjusting the effective rim angle and focal length of the solar collector so that a more uniform radiation heat flux would be incident along the coil surface and less heat lost due to reflected radiation.

A second-law analysis was performed on the solar collector to determine the main contributors to irreversibility in the system. The total irreversibility of the solar collector was determined to be 1 696 W over the testing period. It was found that the temperature difference between the surface temperature of the sun and the surface temperature of the coils caused the largest irreversibility to occur. The total irreversibility from the incident solar radiation heat absorption into the receiver coil accounted for 38% of the total irreversibility. This can be addressed by shifting the power cycle up in pressure. This would lead to an increase in the average surface temperature of the coils, thus reducing the large temperature difference between the sun and the receiver coils. However, it would also increase the heat loss from the receiver. An optimum set of operating conditions can be determined for the solar collector by comparing the irreversibility of coil absorption and the irreversibility of heat loss for a given change in surface temperature. This can be achieved through parametric experimental analysis at different operating conditions, which is recommended for future work. Since the current research only reported on a single set of operating conditions, the optimum could not be accurately predicted.

The designed solar collector performed rather poorly during the thermal tests, since the reflector shape was not optimised for the receiver design. Specific attention should be given to this in future work in order to better determine the optimum power potential of the solar collector. It should also be noted that the operating conditions of the associated steam turbine should be taken into account to better determine the optimum operating conditions of the entire power cycle.

5. Uncertainty analysis

The uncertainties associated with the measurement devices used in the current research are summarised in Table 22. The standard uncertainty is statistically representative of 1 standard deviation from the mean, assuming normal distribution. The total uncertainty considered in the current research accounted for 2 standard deviations from the mean, or a 95% confidence level. The measurement uncertainties were either determined from the calibration process (see Appendix C) or they were determined from the manufacturer's equipment specifications.

Table 22: Summary of measurement uncertainties

Parameter	Measurement uncertainty	Relative uncertainty (%)
Temperature (K)		
TC 1	3.05	0.93
TC 2	2.66	0.68
TC 3	3.10	0.75
TC 4	2.43	0.46
TC 5	2.69	0.41
TC 6	2.51	0.38
TC 7	2.66	0.41
TC 8	2.58	0.41
TC 9	2.79	0.45
TC 10	2.50	0.57
T_∞	0.98	0.28
Pressure (kPa)		
$P1$	0.78	0.23
$P2$	0.70	0.20
P_∞	0.25	0.29
Mass (kg)		
m_w	1.1e-2	0.2
Time (seconds)		
t	0	0
Length (m)		
L	1.15e-3	-
Area (m^2)		
A_{dish}	0.04	1.47
DNI (W/m^2)		
I_{sun}	17.49	2.31
Reflector efficiency (-)		
η_{ref}	0.032	3.30
Optical efficiency (-)		
IF	0.077	8.79

The combined uncertainties for the fundamental output parameters defined in Section 3 and Section 4 are summarised in Table 23. The combined uncertainty of an output parameter is defined as the propagation of the measurement uncertainties on which the output parameter is dependent. Each measurement uncertainty carries a weighting, otherwise referred to as a sensitivity, which is further explained and calculated in Appendix D.

Table 23: Combined standard uncertainty for important output parameters

Parameter (units)	**Symbol**	**Expanded uncertainty**	**Relative uncertainty (%)**
Mass flow rate (kg/s)	$\dot{m}_w$	2.92e-6	1.00
Captured heat (W)	ΔH_w	9.67	1.12
Heat incident at aperture (W)	$\dot{Q}_{ap}$	170.64	9.78
First-law efficiency (receiver) (-)	η_{rec}	0.049	9.85
Change in exergy (W)	$\Delta\Psi_w$	10.23	4.33
Available work at aperture (W)	Φ_{ap}	158.68	9.78
Second-law efficiency (-)	η_{2nd}	0.016	10.70

The uncertainty analysis was performed to give a range within which the fundamental parameters that were considered in the analysis could fall. The measurement uncertainties were determined for every measurement device that was effectively used. The measurement and expanded uncertainties accounted for a 95% confidence level. Considering the propagation of uncertainty, the expanded uncertainties were calculated for the fundamental output parameters in the analysis. The analysis showed that the prominent propagator of uncertainty came from the intercept factor that was determined from the lunar flux mapping analysis. The uncertainties involved in this analysis influenced the results of the thermal analysis, particularly in the calculation of the intercepted radiation at the aperture. The maximum uncertainty came from the first-law and second-law efficiencies with a relative uncertainty of 10% and 11%, respectively. This can be expected since the efficiencies were effectively a function of all variables involved in this research.

6. Summary, conclusions and recommendations

6.1 Summary

Sub-Saharan Africa has an under-utilised solar resource that is available to provide distributed power generation to rural communities that are not reached by the current grid systems that are in place. Renewable power generation systems are typically infeasible for this purpose, due to their high manufacturing and maintenance costs. This research proposed to address this by experimentally investigating the performance of a micro-scale, solar thermal Rankine cycle with direct steam generation using an affordable facetted reflector design. The intended power-generation range was between 0.1 and 1 kW, which could be used for direct mechanical pumping for rural irrigation systems or municipal water supply. In this way, mechanical-to-electrical conversion efficiencies are mitigated, and the power cycle becomes competitive with current PV technologies to suit this purpose. Micro-scale solar thermal Rankine cycles have not been investigated extensively since there is a gap in the steam turbine market at this scale due to their current inability to efficiently convert low mass flux steam to useful mechanical power. However, with recent studies of volumetric expanders showing promise for micro-scale power production, particularly with scroll expanders, it is appropriate to investigate the power potential of this cycle.

The current research focused on experimentally investigating the performance of the solar collector (the dish reflector and the helical coil solar receiver) for sub-Saharan African solar thermal conditions. A novel stretched-membrane, faceted dish design was developed in collaboration with Mr Roosendaal, which was affordable and could easily be adjusted to suit a given receiver design.

An optical analysis was performed on the dish reflector to characterise its performance. A UV/VIS spectroscopy analysis was performed to determine the facet's spectral reflectivity. A photogrammetry analysis was performed to determine the shape of the facet concavity that occurred when a vacuum was pulled within the facet cavity. This was done so that the facet may be accurately modelled in future numerical analyses. A photographic lunar flux analysis was performed to determine the intercept factor of the given dish design for different receiver aperture sizes. The lunar flux analysis also allowed for the maximum concentration ratio at the aperture to be determined by scaling the normalised flux distribution to the incident solar thermal radiation at the aperture.

An experimental thermal analysis was conducted on the solar collector to characterise its performance under realistic environmental conditions. A first-law analysis was conducted to determine the total energy potential of the receiver and to characterise the heat losses that occurred. A second-law

analysis was conducted to determine the second-law efficiency of the system and to determine the main contributors of irreversibility in the collector.

6.2 Conclusion

It was important to characterise the optical performance of the reflector, since the results could then be used to calculate the thermal efficiency of the receiver during solar testing. The primary objective of the analysis was to determine the amount of solar radiation that would be intercepted at the receiver aperture. Using UV/VIS spectroscopy, the spectral reflectivity of the Mylar facet was determined to be 97% within the visible light spectrum. This accounts for approximately half of the total solar spectrum present on the earth's surface. The shape of the facet concavity produced by forming a vacuum in the cavity of the dish facet was investigated using photogrammetry. An elliptical paraboloid and a hemi-ellipsoid were fitted to the photogrammetry results. It was determined that the hemi-ellipsoid most accurately resembled the concave shape. The intercept factor at the receiver aperture was investigated through photographic lunar flux mapping. The analysis was performed during a clear night of a full moon, and a picture was taken of the concentrated image on a near-Lambertian target surface, positioned at the focal point of the dish reflector. Normalised flux maps were produced with light pollution correction, as well as uncorrected light pollution for a raw image, and an equivalent JPEG image to compare the variation in the accuracies of the given methods. It was found that the JPEG image inaccurately represented the flux distribution on the target surface due to image compression. The intercept factor trend for the raw normalised flux distribution with light pollution correction was considered to be the most accurate representation of the solar flux distribution on the target surface. This is because no pixel information is lost due to image compression, and the effect of light pollution is mitigated. Based on the results, an intercept factor ranging between 87 and 93% was considered for the intended receiver design with an aperture diameter ranging between 135 and 200 mm.

For the thermal analysis of the solar collector, the solar receiver was positioned at the focal point of the solar reflector, and the collector followed the sun throughout the testing period using a solar tracker. During the testing period, steady inlet and outlet steam temperatures were achieved with municipal water run through the receiver at 0.29 g/s at a supply pressure of 3 bar. The inlet temperature at TC 1 was kept steady at 54 °C, and the outlet temperature at TC 9 was kept steady at 343.12 °C. The target supply pressure was determined to be 6 bar in Table 1, but unforeseen pressure pulsations caused the pressure in the receiver to rise by as much as 2.85 bar above the supply pressure. This resulted in the supply pressure being lowered to 3 bar during testing in the interest of safety.

With an average solar irradiance of 757 W/m^2 measured over the testing period and a reflector incident area of 2.73 m^2, the solar collector was able to capture 861 W of heat in the working fluid. The thermal efficiency of the collector was thus determined to be 42%, which is far from an ideal collector efficiency. According to the experimental results, a total heat loss rate of 884 W was determined. A heat loss model was developed that could predict the heat loss rate to within 5%. According to the heat loss model, the main contributors to the heat loss from the receiver were the convection and radiation heat losses through the aperture. These components formed 84% of the total heat loss in the receiver. Using the heat loss model and the intercept factor trend determined in Section 3.4, the aperture sizing was analysed. It was determined that an adjustment in the aperture diameter would produce a negligible change in the captured heat. The focus should rather be shifted to optimising the shape of the dish reflector in conjunction with the receiver shape in order to minimise the total heat loss through the aperture and maximise the heat gained by the working fluid. From the second-law analysis, the total irreversibility of the solar collector was determined to be 1 696 W over the testing period. It was found that the large temperature difference between the surface temperature of the sun and the surface temperature of the coils caused the largest irreversibility to occur. Irreversibility from the incident solar radiation heat absorption into the receiver coil accounted for 38% of the total irreversibility.

The designed solar collector performed rather poorly during the thermal tests since the reflector shape was not optimised for the receiver design. However, this investigation is considered to be successful in that that important aspects of the collector design were highlighted from the losses and irreversibilities involved during testing. The research has laid a foundation from which the micro-scale, direct steam generation solar thermal Rankine cycle design can be optimised more effectively by considering important design aspects that became evident in this study.

6.3 Recommendations

Based on the results of the thermal analysis, some recommendations can be made with regard to future research.

Firstly, specific attention should be paid to the collector design, as the reflector shape should directly influence the shape of the receiver cavity and vice versa. This was not necessarily taken into account in the current study, since a receiver cavity with a cavity aspect ratio of approximately 2.23 was assumed to be appropriate for a parabolic dish with a 45° rim angle. Furthermore, the specific shape of a faceted dish reflector with an effective rim angle of 45° at the centroid of each facet would have an extreme rim angle of 61.5° at the outer diameter of the reflector, as is evident in Figure 21.

The receiver's aspect ratio should be characterised as a function of the effective rim angle of the facetted reflector by considering the major and minor rim angles associated with the reflector shape. In doing so, a more uniform incident radiation flux is expected to be present within the receiver cavity. Adding to this, the effective rim angle should be reduced in the current design, thereby increasing both the focal length and the required receiver aspect ratio so that less radiation is reflected from the receiver cavity.

When considering the intercept factor results from the optical analysis, a numerical model should be developed that may be validated by the lunar flux mapping results and, in turn, validate the resulting intercept factor trend at the given experimental receiver aperture. For the sake of time, the numerical model was not considered in the current study. Since the intercept factor trend was developed for a circular aperture on a flat target surface, it was assumed that no external geometry would interfere with the incident radiation at the aperture. However, the experimental receiver included a wind guard that may have resulted in additional spillage at the aperture, which was not accounted for in the intercept factor results. The additional receiver geometry may be modelled in numerical software, which would allow for a better approximation of the intercept factor for the given aperture size. Furthermore, the numerical model could also be used to better approximate the reflected radiation heat loss from the aperture, since a crude approximation was used in the current study.

The pressure pulsations that occurred during the thermal analysis were determined to come from the constant aperture needle valve that was used as an expansion valve at the outlet of the receiver (see Figure 33). As steam rapidly expanded within the coil from a slug of water passing over a heated section of the coil surface, the pressure would increase within the coil. This phenomenon was observed and explained in Section 4.5 and Section 4.6.1. A realistic expander would be expected to run quicker, increasing the mass flow rate, to relieve the pressure. Since the needle valve was kept at a constant aperture area, nothing was done to mitigate the pressure pulsation. To better approximate an expansion device, a constant pressure condition should be imposed at the outlet of the collector by means of a steam valve. The steam valve would better approximate a turbine expansion device by adjusting its aperture to ensure a constant set pressure.

Future optimisation studies should focus on a parametric analysis of the operating conditions of the solar collector. The mass flow rate and pressure should be adjusted to parametrise the temperature conditions within the receiver. The solar irradiance would have to remain constant in order for the analysis to be carried out, or an intercepted radiation condition could be mimicked in a lab using an artificial heat supply. With these results, an optimum set of operating conditions could be determined from a second-law analysis, as suggested in Section 4.6.5.

Municipal tap water was used as the working fluid since one of the purposes of the study was for the solar thermal Rankine cycle to be used at a decentralised scale. It was considered that these areas may not have access to systems that could demineralise the water. This would add to maintenance costs and work against the feasibility of the design being investigated. However, the use of municipal water means that solids would accumulate within the receiver from the boiling process, which would negatively impact on the receiver's performance, thus, also negatively affecting the feasibility of the solution. It is recommended that future investigations should consider the use of demineralised water or an alternative working fluid that can easily be sourced at a decentralised scale.

7. References

[1] International Energy Agency, "World energy outlook special report – Africa energy outlook," Paris, France, 2014.

[2] G. Legros, I. Havet, N. Bruce, and S. Bonjour, "The energy access situation in developing countries: A review focusing on the least developed countries and sub-Saharan Africa," New York, NY, United States, 2009.

[3] S. Baurzhan, and G. P. Jenkins, "Off-grid solar PV: Is it an affordable or appropriate solution for rural electrification in sub-Saharan African countries?," *Renewable and Sustainable Energy Reviews,* vol. 60, pp. 1405–1418, 2016.

[4] International Energy Agency, "World energy outlook special report – energy access outlook," Paris, France, 2017.

[5] C. Kende-Robb, K. Watkins, P. da Costa, B. B. Kassaye, A. Johnston, and T. Minney, "Lights, power, action – electrifying Africa," African Progress Panel, 2017.

[6] Lighting Global, Dalberg Advisors, and GOGLA, "Off-grid solar market trends report 2018," vol. 4, Washington, DC, United States, 2018.

[7] S. Sivasanker, A. Lane, and M. A. Smith, "Sub-Saharan Africa power trends – power disruption in Africa," Deloitte, 2017.

[8] Department of Energy, "Non-grid electrification policy guidelines," South Africa, 2012, available at: http://www.energy.gov.za/files/policies_frame.html. [accessed on: 05/05/2018].

[9] P. A. Trotter, and S. Abdullah, "Re-focusing foreign involvement in sub-Saharan Africa's power sector on sustainable development," *Energy for Sustainable Development,* vol. 44, pp. 139–146, 2018.

[10] F. Boamah, and E. Rothfuß, "From technical innovations towards social practices and socio-technical transition? Re-thinking the transition to decentralised solar PV electrification in Africa," *Energy Research and Social Science,* vol. 42, pp. 1–10, 2018.

[11] A. Belward, B. Bisselink, K. Bodis, A. Brink, and J. F. Dallemand, "Renewable energies in Africa – current knowledge," European Commission and Joint Research Centre, Luxembourg, 2011.

[12] SOLARGIS, 2016. "*Solar resource maps of Africa,"* available at: https://solargis.com/maps-and-gis-data/download/africa. [accessed on: 06/06/2018].

[13] Jinko Solar Co Ltd, 2019. "*Jinko Solar – Build your trust in solar,"* available at: https://www.jinkosolar.com/. [accessed on: 15/03/2019].

[14] Trina Solar, 2018. "*Trina Solar,"* available at: http://www.trinasolar.com/us. [accessed on: 17/06/2018].

[15] Canadian Solar, 2018. "*Canadian Solar,"* available at: https://www.canadiansolar.com/. [accessed on: 30/07/2018].

[16] G. Knier, 2008. "*How do photovoltaics work?,"* available at: https://science.nasa.gov/science-news/science-at-nasa/2002/solarcells. [accessed on: 15/03/2019].

[17] D. A. Quansah, M. S. Adaramola, and L. D. Mensah, "Solar photovoltaics in sub-Saharan Africa – addressing barriers, unlocking potential," *Energy Procedia,* vol. 106, pp. 97–110, 2016.

[18] G. Alva, Y. Lin, and G. Fang, "An overview of thermal energy storage systems," *Energy,* vol. 144, pp. 341–378, 2018.

[19] Y. W. Wong, and K. Sumathy, "Solar thermal water pumping systems: a review," *Renewable and Sustainable Energy Reviews,* vol. 3, no. 2, pp. 185–217, 1999.

[20] B. Ali, "Comparative assessment of the feasibility for solar irrigation pumps in Sudan," *Renewable and Sustainable Energy Reviews,* vol. 81, pp. 413–420, 2018.

[21] S. Mohammed Wazed, B. R. Hughes, D. O'Connor, and J. Kaiser Calautit, "A review of sustainable solar irrigation systems for sub-Saharan Africa," *Renewable and Sustainable Energy Reviews,* vol. 81, pp. 1206–1225, 2018.

[22] J. Zhu, K. Wang, H. Wu, D. Wang, J. Du, and A. G. Olabi, "Experimental investigation on the energy and exergy performance of a coiled tube solar receiver," *Applied Energy,* vol. 156, pp. 519–527, 2015.
[23] S. Pavlovic, E. Bellos, W. G. Le Roux, V. Stefanovic, and C. Tzivanidis, "Experimental investigation and parametric analysis of a solar thermal dish collector with spiral absorber," *Applied Thermal Engineering,* vol. 121, pp. 126–135, 2017.
[24] J. L. Bouvier, G. Michaux, P. Salagnac, T. Kientz, and D. Rochier, "Experimental study of a micro combined heat and power system with a solar parabolic trough collector coupled to a steam Rankine cycle expander," *Solar Energy,* vol. 134, pp. 180–192, 2016.
[25] K. E. Dellar, W. G. Le Roux, and J. P. Meyer, "Experimental testing of a small-scale solar thermal Brayton cycle recuperator," in *Proceedings of the International Heat Transfer Conference (IHTC 2018)*, Beijing, China: Begel House, pp. 4815–4822, 2018.
[26] W. G. Le Roux, "Thermodynamic optimisation and experimental collector of a dish-mounted small-scale solar thermal Brayton cycle (Thesis)," University of Pretoria, Pretoria, South Africa, 2015.
[27] T. M. Wolff, W. G. Le Roux, and J. P. Meyer, "Analysis of a parabolic dish solar collector via lunar flux mapping," in *Proceedings of the 5th Southern African Solar Energy Conference (SASEC 2018)*, Durban, South Africa, pp. 25–27, 2018.
[28] O. Aboelwafa, S. E. K. Fateen, A. Soliman, and I. M. Ismail, "A review on solar Rankine cycles: Working fluids, applications, and cycle modifications," *Renewable and Sustainable Energy Reviews,* vol. 82, pp. 868–885, 2018.
[29] A. Giovannelli, "State of the art on small-scale concentrated solar power plants," *Energy Procedia,* vol. 82, pp. 607–614, 2015.
[30] B. F. Tchanche, G. Papadakis, G. Lambrinos, and A. Frangoudakis, "Fluid selection for a low-temperature solar organic Rankine cycle," *Applied Thermal Engineering,* vol. 29, no. 11, pp. 2468–2476, 2009.
[31] R. Loni, A. B. Kasaeian, E. Askari Asli-Ardeh, B. Ghobadian, and S. Gorjian, "Experimental and numerical study on dish concentrator with cubical and cylindrical cavity receivers using thermal oil," *Energy,* vol. 154, pp. 168–181, 2018.
[32] R. Loni, A. B. Kasaeian, E. Askari Asli-Ardeh, and B. Ghobadian, "Optimizing the efficiency of a solar receiver with tubular cylindrical cavity for a solar-powered organic Rankine cycle," *Energy,* vol. 112, pp. 1259–1272, 2016.
[33] R. Loni, A. B. Kasaeian, E. Askari Asli-Ardeh, B. Ghobadian, and W. G. Le Roux, "Performance study of a solar-assisted organic Rankine cycle using a dish-mounted rectangular-cavity tubular solar receiver," *Applied Thermal Engineering,* vol. 108, pp. 1298–1309, 2016.
[34] I. H. Bell, J. Wronski, S. Quoilin, and V. Lemort, "Pure and pseudo-pure fluid thermophysical property evaluation and the open-source thermophysical property library CoolProp," *Industrial and Engineering Chemistry Research,* vol. 53, no. 6, pp. 2498–2508, 2014.
[35] S. A. Kalogirou, "Solar thermal collectors and applications," *Progress in Energy and Combustion Science,* vol. 30, no. 3, pp. 231–295, 2004.
[36] A. M. Delgado-Torres, "Solar thermal heat engines for water pumping: An update," *Renewable and Sustainable Energy Reviews,* vol. 13, no. 2, pp. 462–472, 2009.
[37] B. F. Tchanche, G. Lambrinos, A. Frangoudakis, and G. Papadakis, "Low-grade heat conversion into power using organic Rankine cycles – a review of various applications," *Renewable and Sustainable Energy Reviews,* vol. 15, no. 8, pp. 3963–3979, 2011.
[38] C. Y. Lee, P. C. Chou, C. M. Chiang, and C. F. Lin, "Sun tracking systems: A review," *Sensors,* vol. 9, no. 5, pp. 3875–3890, 2009.
[39] B. Stafford, M. Davis, J. Chambers, M. Martínez, and D. Sanchez, "Tracker accuracy: Field experience, analysis, and correlation with meteorological conditions," in *Proceedings of the 34th IEEE Photovoltaic Specialists Conference*, Philadelphia, PA, United States, pp. 002256–002259, 2009.

[40] A. Giostri, and E. Macchi, "An advanced solution to boost sun-to-electricity efficiency of parabolic dish," *Solar Energy,* vol. 139, pp. 337–354, 2016.
[41] W. Reinalter, S. Ulmer, P. Heller, T. Rauch, J. M. Gineste, A. Ferriere, and F. Nepveu, "Detailed performance analysis of a 10kW dish/Stirling system," *Journal of Solar Energy Engineering,* vol. 130, no. 1, p. 011013, 2007.
[42] W. B. Stine, and R. W. Harrigan, "Solar energy fundamentals and design : With computer applications," in: *Alternate energy*, New York, NY, United States: Wiley, pp. 0735–8210, 1985.
[43] W. B. Stine, and G. G. McDonald, "Cavity receiver convection heat loss," in *Proceedings of the International Solar Energy Society – Solar World Congress (SWC)*, Japan, vol. 1318, 1989.
[44] P. R. Fraser, "Stirling dish system performance prediction model (Thesis)," University of Wisconsin, Madison, WI, United States, 2008.
[45] S. Paitoonsurikarn, and K. Lovegrove, "Effect of paraboloidal dish structure on the wind near a cavity receiver," in *Proceedings of the 44th Annual Conference of the Australian and New Zealand Solar Energy Society (ANZSES 2006)*, Canberra, Australia, pp. 1–7, 2006.
[46] M. Uzair, "Wind induced heat losses from solar dish-receiver systems (Thesis)," Auckland University of Technology, Auskland, New Zealand, 2018.
[47] A. Z. Hafez, A. Soliman, K. A. El-Metwally, and I. M. Ismail, "Design analysis factors and specifications of solar dish technologies for different systems and applications," *Renewable and Sustainable Energy Reviews,* vol. 67, pp. 1019–1036, 2017.
[48] Y. A. Cengel, and A. J. Ghajar, *Heat and mass transfer: Fundamentals and applications*, 5th ed., New York, NY, United States: McGraw-Hill Education, 2014.
[49] W. M. Rohsenow, "A method of correlating heat transfer data for surface boiling of liquids," MIT Division of Industrial Cooporation, Cambridge, MA, United States, No. 5, 1951.
[50] N. Zuber, "Hydrodynamic aspects of boiling heat transfer (Thesis)," University of California, Los Angeles, CA, United States, 1959.
[51] W. Davidson, "Studies of heat transmission trough boiler tubing at pressures from 500 to 3,300 pounds," *Trans. ASME,* vol. 65, pp. 553-591, 1943.
[52] W. R. Dean, "XVI. Note on the motion of fluid in a curved pipe," *The London, Edinburgh, and Dublin Philosophical Magazine and Journal of Science,* vol. 4, no. 20, pp. 208–223, 1927.
[53] S. Kakac, H. Liu, and A. Pramuanjaroenkij, *Heat exchangers: Selection, rating, and thermal design*, Bacon Raton, FL, United States: CRC press, 2002.
[54] R. Lockhart, and R. Martinelli, "Proposed correlation of data for isothermal two-phase, two-component flow in pipes," *Chem. Eng. Prog,* vol. 45, no. 1, pp. 39-48, 1949.
[55] K. Ishida, "Two-phase flow with heat transfer in helically-coiled tubes (Thesis)," Empirical College, London, United Kingdom, 1981.
[56] H. Zhu, Z. Li, X. Yang, G. Zhu, J. Tu, and S. Jiang, "Flow regime identification for upward two-phase flow in helically coiled tubes," *Chemical Engineering Journal,* vol. 308, pp. 606–618, 2017.
[57] W. Cui, L. Li, M. Xin, T. C. Jen, Q. Liao, and Q. Chen, "An experimental study of flow pattern and pressure drop for flow boiling inside microfinned helically coiled tube," *International Journal of Heat and Mass Transfer,* vol. 51, no. 1, pp. 169–175, 2008.
[58] G. Berthoud, and S. Jayanti, "Characterization of dryout in helical coils," *International Journal of Heat and Mass Transfer,* vol. 33, no. 7, pp. 1451–1463, 1990.
[59] A. M. Elsayed, "Heat transfer in helically coiled small diameter tubes for miniature cooling systems (Thesis)," University of Birmingham, Birmingham, United Kingdom, 2011.
[60] A. Owhadi, K. J. Bell, and B. Crain, "Forced convection boiling inside helically-coiled tubes," *International Journal of Heat and Mass Transfer,* vol. 11, no. 12, pp. 1779–1793, 1968.

[61] M. Kozeki, H. Nariai, T. Furukawa, and K. Kurosu, "A study of helically-coiled tube once-through steam generator," *Bulletin of JSME,* vol. 13, no. 66, pp. 1485–1494, 1970.
[62] V. E. Schrock, and L. M. Grossman, "Forced convection boiling in tubes," *Nuclear Science and Engineering,* vol. 12, no. 4, pp. 474–481, 1962.
[63] R. A. Seban, and E. F. McLaughlin, "Heat transfer in tube coils with laminar and turbulent flow," *International Journal of Heat and Mass Transfer,* vol. 6, no. 5, pp. 387–395, 1963.
[64] L. Zhao, L. Guo, B. Bai, Y. Hou, and X. Zhang, "Convective boiling heat transfer and two-phase flow characteristics inside a small horizontal helically coiled tubing once-through steam generator," *International Journal of Heat and Mass Transfer,* vol. 46, no. 25, pp. 4779–4788, 2003.
[65] W. Cui, L. Li, M. Xin, T. C. Jen, Q. Chen, and Q. Liao, "A heat transfer correlation of flow boiling in micro-finned helically coiled tube," *International Journal of Heat and Mass Transfer,* vol. 49, no. 17, pp. 2851–2858, 2006.
[66] V. V. Klimenko, "A generalized correlation for two-phase forced flow heat transfer," *International Journal of Heat and Mass Transfer,* vol. 31, no. 3, pp. 541–552, 1988.
[67] A. Cioncolini, L. Santini, and M. E. Ricotti, "Subcooled and saturated water flow boiling pressure drop in small diameter helical coils at low pressure," *Experimental Thermal and Fluid Science,* vol. 32, no. 6, pp. 1301–1312, 2008.
[68] A. A. Koenig, and M. Marvin, "Convection heat loss sensitivity in open cavity solar receivers," Department of Energy, Oak Ridge, TN, United States, DOE Contract EG77-C-04-3985, 1981.
[69] K. S. Reddy, G. Veershetty, and T. S. Vikram, "Effect of wind speed and direction on convective heat losses from solar parabolic dish modified cavity receiver," *Solar Energy,* vol. 131, pp. 183–198, 2016.
[70] K. S. Reddy, T. S. Vikram, and G. Veershetty, "Combined heat loss analysis of solar parabolic dish – modified cavity receiver for superheated steam generation," *Solar Energy,* vol. 121, pp. 78–93, 2015.
[71] R. Y. Ma, "Wind effects on convective heat loss from a cavity receiver for a parabolic concentrating solar collector," Sandia National Laboratories, Albuqerque, NM, United States, SAND-92-7293, 1993.
[72] J. A. Harris, and T. G. Lenz, "Thermal performance of solar concentrator/cavity receiver systems," *Solar Energy,* vol. 34, no. 2, pp. 135–142, 1985.
[73] S. Quoilin, S. Declaye, and V. Lemort, "Expansion machine and fluid selection for the organic Rankine cycle," in *Proceedings of the 7th International Conference on Heat Transfer, Fluid Mechanics and Thermodynamics (HEFAT 2010)*, Antalya, Turkey, 2010.
[74] V. Pethurajan, S. Sivan, and G. C. Joy, "Issues, comparisons, turbine selections and applications – An overview in organic Rankine cycle," *Energy Conversion and Management,* vol. 166, pp. 474–488, 2018.
[75] M. Imran, M. Usman, B. S. Park, and D. H. Lee, "Volumetric expanders for low grade heat and waste heat recovery applications," *Renewable and Sustainable Energy Reviews,* vol. 57, pp. 1090–1109, 2016.
[76] O. Badr, S. D. Probert, and P. O'Callaghan, "Performances of multi-vane expanders," *Applied Energy,* vol. 20, no. 3, pp. 207–234, 1985.
[77] O. Badr, S. D. Probert, and P. O'Callaghan, "Multi-vane expanders: Vane dynamics and friction losses," *Applied Energy,* vol. 20, no. 4, pp. 253–285, 1985.
[78] M. Farrokhi, S. H. Noie, and A. A. Akbarzadeh, "Preliminary experimental investigation of a natural gas-fired ORC-based micro-CHP system for residential buildings," *Applied Thermal Engineering,* vol. 69, no. 1-2, pp. 221–229, 2014.
[79] B. Carey, "Total flow power generation from geothermal resources using a helical screw expander," in *Proceedings of the 5th New Zealand geothermal workshop*, Auckland, New Zealand, pp. 127–132, 1983.
[80] Y. Q. Zhang, Y. T. Wu, G. D. Xia, C. F. Ma, W. N. Ji, S. W. Liu, K. Yang, and F. B. Yang, "Development and experimental study on organic Rankine cycle system with single-

screw expander for waste heat recovery from exhaust of diesel engine," *Energy,* vol. 77, pp. 499–508, 2014.
[81] V. Krishna Avadhanula, and C. S. Lin, "Empirical models for a screw expander based on experimental data from organic Rankine cycle system testing," *Journal of Engineering for Gas Turbines and Power,* vol. 136, no. 6, p. 062601, 2014.
[82] D. Seher, T. Lengenfelder, J. Gerhardt, N. Eisenmenger, M. Hackner, and I. Krinn, "Waste heat recovery for commercial vehicles with a Rankine process," in *Proceedings of the 21st Aachen Colloquium on Automobile and Engine Technology*, Aachen, Germany, pp. 7–9, 2012.
[83] N. Zheng, L. Zhao, X. D. Wang, and Y. T. Tan, "Experimental verification of a rolling-piston expander that applied for low-temperature organic Rankine cycle," *Applied Energy,* vol. 112, pp. 1265–1274, 2013.
[84] M. Li, Y. Ma, and H. Tian, "A rolling piston-type two-phase expander in the transcritical CO2 cycle," *HVAC&R Research,* vol. 15, no. 4, pp. 729–741, 2009.
[85] H. J. Kim, J. M. Ahn, I. Park, and P. C. Rha, "Scroll expander for power generation from a low-grade steam source," *Proceedings of the Institution of Mechanical Engineers, Part A: Journal of Power and Energy,* vol. 221, no. 5, pp. 705–711, 2007.
[86] B. Aoun, and D. Clodic, "Theoretical and experimental study of an oil-free scroll type vapor expander," in *Proceedings of the 19th International Compressor Engineering Conference*, West Lafayette, IN, United States: Perdue University, p. 1188, 2008.
[87] N. Zhou, X. Wang, Z. Chen, and Z. Wang, "Experimental study on organic Rankine cycle for waste heat recovery from low-temperature flue gas," *Energy,* vol. 55, pp. 216–225, 2013.
[88] H. Wang, R. B. Peterson, and T. Herron, "Experimental performance of a compliant scroll expander for an organic Rankine cycle," *Proceedings of the Institution of Mechanical Engineers, Part A: Journal of Power and Energy,* vol. 223, no. 7, pp. 863–872, 2009.
[89] Green Turbine, 2018. "*Technical description Green Turbine 1.5 kW,"* available at: http://www.greenturbine.eu. [accessed on: 12/08/2019].
[90] Agilent, 2019. "*Cary 100 UV-Vis,"* available at: https://www.agilent.com. [accessed on: 23/06/2019].
[91] D. L. Pavia, G. M. Lampman, G. S. Kriz, and J. A. Vyvyan, *Introduction to spectroscopy*, 5th ed., Bellingham, WA, United States: Cengage Learning, 2014.
[92] C. Gueymard, *SMARTS2: A simple model of the atmospheric radiative transfer of sunshine: algorithms and performance assessment*, Cocoa, FL, United States: Florida Solar Energy Center, 1995.
[93] ASTM G173-03(2012), "Standard tables for reference solar spectral irradiances: Direct normal and hemispherical on 37° tilted surface," ASTM International, West Conshohocken, PA, United States, 2012, available at: www.astm.org. [accessed on: 20/07/2019].
[94] GOM, 2019. "*ARAMIS Adjustable, The modular measuring system for 2D and 3D analyses,"* available at: https://www.gom.com/metrology-systems/aramis/aramis-adjustable.html. [accessed on: 30/07/2019].
[95] J. A. Nelder, and R. Mead, "A simplex method for function minimization," *The Computer Journal,* vol. 7, no. 4, pp. 308–313, 1965.
[96] M. J. D. Powell, "A direct search optimization method that models the objective and constraint functions by linear interpolation," in: S. Gomez, and J. P. Hennart (Eds.) *Advances in Optimization and Numerical Analysis*, Dordrecht, Netherlands: Springer, pp. 51–67, 1994.
[97] P. Kuhn, and A. Hunt, "A new solar simulator to study high temperature solid-state reactions with highly concentrated radiation," *Solar Energy Materials,* vol. 24, no. 1, pp. 742-750, 1991.
[98] J. Ballestrin, "A non-water-cooled heat flux measurement system under concentrated solar radiation conditions," *Solar Energy,* vol. 73, no. 3, pp. 159-168, 2002.

[99] J. Ballestrín, and R. Monterreal, "Hybrid heat flux measurement system for solar central receiver evaluation," *Energy,* vol. 29, no. 5, pp. 915-924, 2004.
[100] E. Guillot, I. Alxneit, J. Ballestrin, J. L. Sans, and C. Willsh, "Comparison of 3 Heat Flux Gauges and a Water Calorimeter for Concentrated Solar Irradiance Measurement," *Energy Procedia,* vol. 49, pp. 2090-2099, 2014.
[101] J. W. Strachan, and R. M. Houser, "Testing and evaluation of large-area heliostats for solar thermal applications," Sandia National Labs, Albuquerque, NM, United States, SAND-92-1381, 1993, available at: https://www.osti.gov/servlets/purl/10177805.
[102] J. B. Blackmon, "Development and performance of a digital image radiometer for heliostat evaluation at Solar One," *Journal of Solar Energy Engineering,* vol. 107, no. 4, pp. 315–321, 1985.
[103] C. L. Mavis, "10 MWe solar thermal central receiver pilot plant heliostat and beam characterization system evaluation November 1981–December 1986," Sandia National Laboratories, Livermore, CA, United States, SAND87-8003, 1988.
[104] B. L. van Bakel, M. J. Brooks, and J. F. P. de la Beaujardiere, "Developement of a high cocncetration solar flux mapping system (Thesis)," University of KwaZulu-Natal, Durban, South Africa, 2018.
[105] S. Ulmer, W. Reinalter, P. Heller, E. Lupfert, and D. Martinez, "Beam characterization and improvement with a flux mapping system for dish concentrators," *Journal of Solar Energy Engineering,* vol. 124, no. 2, pp. 182–188, 2002.
[106] C. K. Ho, and S. S. Khalsa, "A photographic flux mapping method for concentrating solar collectors and receivers," *Journal of Solar Energy Engineering,* vol. 134, no. 4, p. 041004, 2012.
[107] P. Siangsukone, G. Burgess, and K. Lovegrove, "Full moon flux mapping the 400m^2 "Big Dish" at the Australian National University," in *Proceedings of the 42nd Annual Conference of the Australian and New Zealand Solar Energy Society (ANZSES 2004)*, Perth, Australia, pp. 1-3, 2004.
[108] G. Burgess, J. Zapata, R. Chauvin, M. Shortis, J. Pye, and J. Preston, "Three-dimensional flux prediction for a dish concentrator cavity receiver," in *Proceedings of SolarPACES 2012*, Marrakech, Morocco, 2012.
[109] J. Pye, J. Coventry, F. Venn, J. Zapata, E. Abbasi, C. A. Asselineau, G. Burgess, G. Hughes, and W. Logie, "Experimental testing of a high-flux cavity receiver," in *AIP Conference Proceedings – SolarPACES 2016*, Abu Dhabi, United Aarab Emarites, vol. 1850, no. 1: AIP Publishing, p. 110011, 2016.
[110] G. Zanganeh, R. Bader, A. Pedretti, M. Pedretti, and A. Steinfeld, "A solar dish concentrator based on ellipsoidal polyester membrane facets," *Solar Energy,* vol. 86, no. 1, pp. 40–47, 2012.
[111] M. Reichert, 2014. "*rawpy 0.13.1,"* available at: https://pypi.org/project/rawpy. [accessed on: 02/05/2019].
[112] P. Rojtberg, 2017. "*Processing RAW images in Python,"* available at: https://www.researchgate.net/publication/314239357_Processing_RAW_images_in_Python. [accessed on: 25/05/2019].
[113] A. Žukauskas, "Heat transfer from tubes in crossflow," in: J. P. Hartnett, and T. F. Irvine (Eds.) *Advances in Heat Transfer*, vol. 8, New York, NY, United States: Academic Press, pp. 93–160, 1972.
[114] T. Fujii, and H. Imura, "Natural-convection heat transfer from a plate with arbitrary inclination," *International Journal of Heat and Mass Transfer,* vol. 15, no. 4, pp. 755–767, 1972.
[115] G. C. Vliet, "Natural convection local heat transfer on constant-heat-flux inclined surfaces," *Journal of Heat Transfer,* vol. 91, no. 4, pp. 511–516, 1969.
[116] R. Petela, "Exergy of undiluted thermal radiation," *Solar Energy,* vol. 74, no. 6, pp. 469–488, 2003.

[117] S. O. Onyegegbu, and J. Morhenne, "Transient multidimensional second law analysis of solar collectors subjected to time-varying insolation with diffuse components," *Solar Energy,* vol. 50, no. 1, pp. 85–95, 1993.
[118] S. Farahat, F. Sarhaddi, and H. Ajam, "Exergetic optimization of flat plate solar collectors," *Renewable Energy,* vol. 34, no. 4, pp. 1169–1174, 2009.
[119] W. G. Le Roux, T. Bello-Ochende, and J. P. Meyer, "A review on the thermodynamic optimisation and modelling of the solar thermal Brayton cycle," *Renewable and Sustainable Energy Reviews,* vol. 28, pp. 677–690, 2013.
[120] A. Bejan, D. W. Kearney, and F. Kreith, "Second law analysis and synthesis of solar collector systems," *Journal of Solar Energy Engineering,* vol. 103, no. 1, pp. 23–28, 1981.
[121] M. J. Brooks, S. du Clou, W. L. van Niekerk, P. Gauché, C. Leonard, M. J. Mouzouris, R. Meyer, N. van der Westhuizen, E. E. van Dyk, and F. J. Vorster, "SAURAN: A new resource for solar radiometric data in Southern Africa," *Journal of Energy in Southern Africa,* vol. 26, no. 1, pp. 2–10, 2015.
[122] N. Geuder, S. Wilbert, and N. Janotte, "Precise measurements of solar beam irradiance through improved sensor calibration," in *Proceedings of SolarPACES 2009*, Berlin, Germany, pp. 1–8, 2009.
[123] V. C. Sharma, and A. Sharma, "Solar properties of some building elements," *Energy,* vol. 14, no. 12, pp. 805–810, 1989.
[124] Firebird Thermal Products, 2019. "*Ceramic fibre products,"* available at: http://www.firebirdref.com/a/caipin/toupan/. [accessed on: 23/04/2019].

Appendix A: Python code for lunar flux mapping

A.1 Introduction

The following Python code was developed in collaboration with Mr Casey Roosendaal to process the JPEG and CR2 images taken during the lunar flux testing.

A.2 Python code

```
# -*- coding: utf-8 -*-
"""
Created on Fri Jul 26 22:41:00 2019

@author: jonsw
"""
import numpy as np
import matplotlib.pyplot as plt
import scipy.optimize as opt
from scipy import io

import rawpy
import imageio
from PIL import Image

import tkinter as tk
from tkinter import filedialog as fd

import os.path as osp

##INPUT#############################################################
########

noise = 0
maxpix = 255

amp = 1     #Amplify pixel intensity ...
tol = 1e-3  #within a given tolerance

DNI = 1000
Adish = 2.73
OptEff = 1
Ref = 0.97

Vertices = [[343,3510], ##Clockwise starting top left
            [2687,3387],
            [2688,1061],
            [273,1037]]

Vertices = np.append(Vertices, Vertices[0])
Vertices = np.reshape(Vertices, (5,2))

Center = [1460,2280]#JPEG
#Center = [1470,2282]#CR2

Actual_pixels = [5184,3456]
Area = 540**2

pol_boundary = 2
```

```
ap = np.arange(0,700,5) ##units = mm

##READ#############################################################################
########

root = tk.Tk()
root.withdraw()

fp = fd.askopenfilename()

print(fp)

filename,file_ext = osp.splitext(fp)

print(file_ext)

if file_ext == '.CR2':

    rimg = rawpy.imread(fp)

    shape = rimg.sizes
    print(shape)

    RGBimg = rimg.postprocess(
                                no_auto_bright=True,
                                use_camera_wb = True,
                                no_auto_scale=True,
                                output_color = rawpy.ColorSpace.sRGB,
                                output_bps=16
                              )
    """Pixel values will range from 0 to 65536 for a 16 bit RGB
image"""

    print(RGBimg)
    print(np.shape(RGBimg))
    print(np.max(RGBimg))
    print()

    plt.figure(1)
    plt.imshow(RGBimg)
    plt.show(1)

    imageio.imsave('test.tiff',RGBimg)
    rimg.close()

    img_gs = (RGBimg[:,:,0]+RGBimg[:,:,1]+RGBimg[:,:,2])/3

if file_ext == '.JPEG' or file_ext == '.jpeg' or file_ext == '.JPG':
##WORK BY MR CASEY ROOSENDAAL
    im = Image.open(fp)
    im.show()
    form, size, mode=(im.format, im.size, im.mode)
    im= im.load()

    print("Image Format: ",form)
    print()
    print("Image Size: ",size)
    print()
```

```
    print("Image Pixel Structure: ",mode)
    print()
    print()

    print("Processing Image File")
    RGBimg = np.zeros(size)
    img_gs = np.zeros(size)
    for i in range(size[0]):
        for j in range(size[1]):
            pix=im[i,j]
            img_gs[i,j] = (pix[0] + pix[1] + pix[2])/3

    img_gs = img_gs.transpose()

##PixelArea#################################################################
#######

print(Vertices)
print()

S = []
for i in range(len(Vertices)-1):
    S = np.append(S,[np.sqrt((Vertices[i+1,0]-Vertices[i,0])**2 +
                             (Vertices[i+1,1]-Vertices[i,1])**2)])

S = np.append(S,[np.sqrt((Vertices[2,0]-Vertices[0,0])**2 +
                         (Vertices[2,1]-Vertices[0,1])**2)])## Diagonal

print(S)
print()

s = [(S[0] + S[1] + S[4])/2, (S[2] + S[3] + S[4])/2]

a = np.array([

        [np.sqrt(s[0]*(s[0]-S[0])*(s[0]-S[1])*(s[0]-S[4]))],
        [np.sqrt(s[1]*(s[1]-S[2])*(s[1]-S[3])*(s[1]-S[4]))],

        ])

A_pixels = np.sum(a)

A_pixel = Area/A_pixels
s_pixel = np.sqrt(A_pixel)

print("A1:", str(A_pixel))
print("S1:", str(s_pixel))

##LINEAR
BOUNDARIES#################################################################

def constraints (V):
    ans = np.array([])
    for i in range(len(Vertices)-1):

        ans = np.append(

                        ans,
```

```
                          [V[i,1]-V[i,0]*((V[i+1,1]-V[i,1])/(V[i+1,0]-
V[i,0])),
                          (V[i+1,1]-V[i,1])/(V[i+1,0]-V[i,0])]

                          )

    ans = np.reshape(ans, (4,2))
    return ans

def pttoline(c,m,pt):

    mi = -1*1/m
    ci = pt[1]-mi*pt[0]

    xb = (ci-c)/(m-mi)
    yb = m*xb + c

    dist = np.hypot(pt[0]-xb,pt[1]-yb)

    return dist

##PROCESS#############################################################
########

n_img_gs = np.transpose(img_gs)
nx,ny = n_img_gs.shape

print(nx)
print(ny)

if file_ext == '.CR2':
    ##Adjust pos of vertices
    Vertices[:,0] = np.array(Vertices[:,0] + (ny-Actual_pixels[1])/2)
    Vertices[:,1] = np.array(Vertices[:,1] + (nx-Actual_pixels[0])/2)

    ##Adjust pos of center
    Center = np.round([Center[0]+(ny-Actual_pixels[1])/2,
                       Center[1]+(nx-Actual_pixels[0])/2],0)
    Center = np.array([int(Center[0]),int(Center[1])])

C = constraints(Vertices)
print(C)

xp = np.linspace(0, nx-1,nx)
yp = np.linspace(0, ny-1,ny)
Xp,Yp = np.meshgrid(yp,xp)

print(Xp)
print(Yp)

print(np.shape(Xp))
print(np.shape(Yp))

xp_a = np.linspace(1, nx,nx)
yp_a = np.linspace(ny, 1,ny)
Xp_a,Yp_a = np.meshgrid(yp_a,xp_a)

xs = np.linspace(0-Center[1]*s_pixel,(nx-Center[1])*s_pixel,nx)
```

```
ys = np.linspace(0-Center[0]*s_pixel,(ny-Center[0])*s_pixel,ny)
Xs,Ys=np.meshgrid(ys,xs)

##Intercept
Factor#################################################################

y2 = min(Vertices[0,1],Vertices[1,1])
y1 = max(Vertices[2,1],Vertices[3,1])
x2 = min(Vertices[1,0],Vertices[2,0])
x1 = max(Vertices[0,0],Vertices[3,0])

print()
print(y1)
print(y2)
print(x1)
print(x2)
print()

crpdx = y2-y1
crpdy = x2-x1

Y1 = np.arange(0,y1,1)
Y2 = np.arange(y2+1,nx,1)
X1 = np.arange(0,x1,1)
X2 = np.arange(x2+1,ny,1)

print(Vertices[0,1],Vertices[1,1])
print(Vertices[2,1],Vertices[3,1])
print(Vertices[1,0],Vertices[2,0])
print(Vertices[0,0],Vertices[3,0])
print()
print(min(Vertices[0,1],Vertices[1,1])-
max(Vertices[2,1],Vertices[3,1]))
print(max(Vertices[0,1],Vertices[1,1])-
min(Vertices[2,1],Vertices[3,1]))
print(min(Vertices[1,0],Vertices[2,0])-
max(Vertices[0,0],Vertices[3,0]))
print(max(Vertices[1,0],Vertices[2,0])-
min(Vertices[0,0],Vertices[3,0]))
print()
print('X: ', str(crpdx), 'Y:', str(crpdy))

n_img_gs[(Yp > C[0,0] + Xp*C[0,1]) |
         (Yp < C[2,0] + Xp*C[2,1]) |
         (Xp > (Yp - C[1,0])/C[1,1]) |
         (Xp < (Yp - C[3,0])/C[3,1])] = 0

print()
print("Max Pixel (pol):", str(np.max(n_img_gs)))
print()

n_img_gs = n_img_gs/np.max(n_img_gs)
Pol = np.zeros(4)
Pol_cnt = np.zeros(4)
pol = 0
pol_cnt = 0
for k in range(4):
    Pol[k] = np.sum(n_img_gs[(np.sqrt((Xs-Xs[0,Vertices[k,0]])**2 +
```

```
                                (Ys-Ys[Vertices[k,1],0])**2) <= 5) &
                                (Yp <= C[0,0] + Xp*C[0,1]) &
                                (Yp >= C[2,0] + Xp*C[2,1]) &
                                (Xp <= (Yp - C[1,0])/C[1,1]) &
                                (Xp >= (Yp - C[3,0])/C[3,1])])
    Pol_cnt[k] = np.count_nonzero(5 + n_img_gs[
                                    (np.sqrt((Xs-Xs[0,Vertices[k,0]])**2
+
                                    (Ys-Ys[Vertices[k,1],0])**2) <= 5) &
                                    (Yp <= C[0,0] + Xp*C[0,1]) &
                                    (Yp >= C[2,0] + Xp*C[2,1]) &
                                    (Xp <= (Yp - C[1,0])/C[1,1]) &
                                    (Xp >= (Yp - C[3,0])/C[3,1])])

pos = [Xp,Yp]
d1 = pttoline(C[0,0],C[0,1],pos)
d2 = pttoline(C[1,0],C[1,1],pos)
d3 = pttoline(C[2,0],C[2,1],pos)
d4 = pttoline(C[3,0],C[3,1],pos)
pol = np.sum(n_img_gs[(Yp <= C[0,0] + Xp*C[0,1]) &
                      (Yp >= C[2,0] + Xp*C[2,1]) &
                      (Xp <= (Yp - C[1,0])/C[1,1]) &
                      (Xp >= (Yp - C[3,0])/C[3,1]) &
                      ((d1 <= pol_boundary) | (d2 <= pol_boundary) |
                       (d3 <= pol_boundary) | (d4 <= pol_boundary))])
pol_cnt = np.count_nonzero(5 + n_img_gs[(Yp <= C[0,0] + Xp*C[0,1]) &
                    (Yp >= C[2,0] + Xp*C[2,1]) &
                    (Xp <= (Yp - C[1,0])/C[1,1]) &
                    (Xp >= (Yp - C[3,0])/C[3,1]) &
                    ((d1 <= pol_boundary) | (d2 <= pol_boundary) |
                     (d3 <= pol_boundary) | (d4 <= pol_boundary))])

totc = np.zeros_like(ap, dtype = float)
tot = np.sum(n_img_gs)

cnt = 0
for h in ap:
    print(cnt)
#    totc[cnt] = np.sum(n_img_gs[(abs(Xs) <= h/2) & (abs(Ys) <=
h/2)])#SQUARE
    totc[cnt] = np.sum(n_img_gs[np.sqrt((Xs)**2+(Ys)**2) <=
h/2])#CIRCLE

    cnt += 1

##Cropping###########################################################
########

crpd_img = np.delete(n_img_gs,Y2,0)
crpd_img = np.delete(crpd_img,Y1,0)
crpd_img = np.delete(crpd_img,X2,1)
crpd_img = np.delete(crpd_img,X1,1)

crpd_Xs = np.delete(Xs,Y2,0)
crpd_Xs = np.delete(crpd_Xs,X2,1)
crpd_Xs = np.delete(crpd_Xs,Y1,0)
crpd_Xs = np.delete(crpd_Xs,X1,1)
```

```
crpd_Ys = np.delete(Ys,Y2,0)
crpd_Ys = np.delete(crpd_Ys,X2,1)
crpd_Ys = np.delete(crpd_Ys,Y1,0)
crpd_Ys = np.delete(crpd_Ys,X1,1)

crpd_Xp = np.delete(Xp,Y2,0)
crpd_Xp = np.delete(crpd_Xp,X2,1)
crpd_Xp = np.delete(crpd_Xp,Y1,0)
crpd_Xp = np.delete(crpd_Xp,X1,1)

crpd_Yp = np.delete(Yp,Y2,0)
crpd_Yp = np.delete(crpd_Yp,X2,1)
crpd_Yp = np.delete(crpd_Yp,Y1,0)
crpd_Yp = np.delete(crpd_Yp,X1,1)

########################################################################
########

Pol = Pol/np.max(n_img_gs)
Pol_avgs = Pol/Pol_cnt
Pol_avg = np.average(Pol/Pol_cnt)

print()
print("Polution Totals: " + str(Pol))
print("Polution Pixels: " + str(Pol_cnt))
print("Polution Averages: " + str(Pol_avgs))
print("Polution Average: " + str(Pol_avg))
print()

pol = pol/np.max(n_img_gs)
pol_avgs = pol/pol_cnt
pol_avg = np.average(pol/pol_cnt)

print()
print("Polution Boundary Totals: " + str(pol))
print("Polution Pixels on Boundary: " + str(pol_cnt))
print("Polution Boundary Averages: " + str(pol_avgs))
print("Polution Boundary Average: " + str(pol_avg))
print()

intf = totc/tot*100

print()
print('Total:' + str(tot))
print()
print('Intercept Factor : ' + str(np.round(intf,0)))
print('Aperture diameter :' + str(ap))

sfIF = np.array([ap,intf])
sfIF = np.transpose(sfIF)

###Center of Gravity#####################################################
########

x_COG = np.sum(n_img_gs*Xp)/np.sum(n_img_gs)
y_COG = np.sum(n_img_gs*Yp)/np.sum(n_img_gs)

x_COGc = x_COG - (ny-Actual_pixels[1])/2
```

```
y_COGc = y_COG - (nx-Actual_pixels[0])/2

print()
print('COGx:' + str(x_COG))
print('COGy:' + str(y_COG))
print('COGxc:' + str(x_COGc))
print('COGyc:' + str(y_COGc))
print()

Vert_flux = n_img_gs[:,Center[0]]
Hor_flux = n_img_gs[Center[1],:]

print(len(Vert_flux))

###OUTPUT#########################################################################
########

plt.figure(1) #Flux map with indexed array
plt.title('Indexed Pixel Distribution')
plt.contourf(Xp, Yp, n_img_gs, 100)
plt.set_cmap('jet')
plt.colorbar(ticks=np.linspace(0,1,11))
plt.xlabel('Horizontal [Index]')
plt.ylabel('Verticle [Index]')
#
#plt.figure(2) #Flux map with actual pixel array
#plt.title('Actual Pixel Distribution')
#plt.contourf(Xp_a, Yp_a, n_img_gs, 100)
#plt.set_cmap('jet')
#plt.colorbar(ticks=np.linspace(0,1,11))
#plt.xlabel('Horizontal [Pixel]')
#plt.ylabel('Verticle [Pixel]')

plt.figure(3) #Flux map with scaled distance array
plt.title('Scaled Pixel Distribution')
plt.contourf(Xs, Ys, n_img_gs, 100)
plt.set_cmap('jet')
plt.colorbar(ticks=np.linspace(0,1,11))
plt.xlabel('x-coordinate [mm]')
plt.ylabel('y-coordinate [mm]')

#plt.figure(4) ##Radiation fluxmap
#plt.contourf(Xs, Ys, Its_fm, levels = 100)
#plt.set_cmap('jet')
#plt.colorbar(ticks=np.linspace(0,np.max(Its_fm),11))
#plt.xlabel('x-coordinate [mm]')
#plt.ylabel('y-coordinate [mm]')

plt.figure(5)
plt.title('Interception Factor')
plt.plot(ap,intf,'.:')
plt.ylabel("Interception Factor [%]")
plt.xlabel("Aperture Diameter [mm]")
plt.grid()

plt.figure(6)
plt.title('Interception Factor')
plt.plot(Adish/ap**2/1000**2,intf,'.:')
```

```
plt.xscale('log')
plt.ylabel("Interception Factor [%]")
plt.xlabel("Geometric Concetration Ratio (Aap/Adish)")
plt.grid()

plt.figure(7)
#plt.plot(ys[:,0],Vert_flux,'.', linewidth=2, markersize=12)
plt.plot(Ys[:,0],Vert_flux,'.', markersize = 2)
plt.ylabel("Normalized Flux")
plt.xlabel("y coordinates [mm]")
plt.grid()

plt.figure(8)
plt.plot(Xs[0,:],Hor_flux,'.', markersize = 2)
plt.ylabel("Normalized Flux")
plt.xlabel("x coordinates [mm]")
plt.grid()

plt.figure(9) #Flux map with indexed array
plt.title('Indexed Pixel Distribution')
plt.contourf(crpd_Xp,crpd_Yp,crpd_img, 100)
plt.set_cmap('jet')
plt.colorbar(ticks=np.linspace(0,1,11))
plt.xlabel('Horizontal [Index]')
plt.ylabel('Verticle [Index]')

plt.figure(10) #Flux map with scaled distance array
plt.title('Scaled Pixel Distribution')
plt.contourf(crpd_Xs,crpd_Ys,crpd_img, 100)
plt.set_cmap('jet')
plt.colorbar(ticks=np.linspace(0,1,11))
plt.xlabel('x-coordinate [mm]')
plt.ylabel('y-coordinate [mm]')

plt.show()

####Save Working
Data############################################################
root = tk.Tk()
root.withdraw()
saveFilePath  =  fd.asksaveasfilename(
                                        initialdir = "/",
                                        title = "Save Intercept Factor
Data",
                                      )
print(saveFilePath)

seq = ""
fn = saveFilePath + "(pol).csv"
#while osp.isfile(fn%seq):
#    seq = int(seq or 0) + 1
#fn = fn % seq

print(fn)

np.savetxt(
            fn,
            sfIF,
```

```
            delimiter = ','
           )
fn = saveFilePath + "_VF(pol).csv"
np.savetxt(
            fn,
            [Ys[:,0],Vert_flux],
            delimiter = ','
           )
fn = saveFilePath + "_HF(pol).csv"
np.savetxt(
            fn,
            [Xs[0,:],Hor_flux],
            delimiter = ','
           )

fn_mat = saveFilePath + "(pol).mat"

mdic = {
        "X": crpd_Xs,
        "Y": crpd_Ys,
        "Z": crpd_img,
        }

io.savemat(fn_mat,mdic)

##Intercept Factor#############################################################
########

print()
print("=============Results WITHOUT Polution=============")
n_img_gs = n_img_gs - pol_avg
n_img_gs[n_img_gs < 0] = 0
print("Max Pixel (npol):", str(np.max(n_img_gs)))

Pol = np.zeros(4)
Pol_cnt = np.zeros(4)
pol = 0
pol_cnt = 0
for k in range(4):
    Pol[k] = np.sum(n_img_gs[(np.sqrt((Xs-Xs[0,Vertices[k,0]])**2 +
                              (Ys-Ys[Vertices[k,1],0])**2) <= 5) &
                              (Yp <= C[0,0] + Xp*C[0,1]) &
                              (Yp >= C[2,0] + Xp*C[2,1]) &
                              (Xp <= (Yp - C[1,0])/C[1,1]) &
                              (Xp >= (Yp - C[3,0])/C[3,1])])
    Pol_cnt[k] = np.count_nonzero(5 + n_img_gs[
                                    (np.sqrt((Xs-Xs[0,Vertices[k,0]])**2
+
                                    (Ys-Ys[Vertices[k,1],0])**2) <= 5) &
                                    (Yp <= C[0,0] + Xp*C[0,1]) &
                                    (Yp >= C[2,0] + Xp*C[2,1]) &
                                    (Xp <= (Yp - C[1,0])/C[1,1]) &
                                    (Xp >= (Yp - C[3,0])/C[3,1])])

pos = [Xp,Yp]
d1 = pttoline(C[0,0],C[0,1],pos)
d2 = pttoline(C[1,0],C[1,1],pos)
d3 = pttoline(C[2,0],C[2,1],pos)
```

```
d4 = pttoline(C[3,0],C[3,1],pos)
pol = np.sum(n_img_gs[(Yp <= C[0,0] + Xp*C[0,1]) &
                      (Yp >= C[2,0] + Xp*C[2,1]) &
                      (Xp <= (Yp - C[1,0])/C[1,1]) &
                      (Xp >= (Yp - C[3,0])/C[3,1]) &
                      ((d1 <= pol_boundary) | (d2 <= pol_boundary) |
                       (d3 <= pol_boundary) | (d4 <= pol_boundary))])
pol_cnt = np.count_nonzero(5 + n_img_gs[(Yp <= C[0,0] + Xp*C[0,1]) &
                    (Yp >= C[2,0] + Xp*C[2,1]) &
                    (Xp <= (Yp - C[1,0])/C[1,1]) &
                    (Xp >= (Yp - C[3,0])/C[3,1]) &
                    ((d1 <= pol_boundary) | (d2 <= pol_boundary) |
                     (d3 <= pol_boundary) | (d4 <= pol_boundary))])

totc = np.zeros_like(ap, dtype = float)
tot = np.sum(n_img_gs)

cnt = 0
for h in ap:
    print(cnt)
#    totc[cnt] = np.sum(n_img_gs[(abs(Xs) <= h/2) & (abs(Ys) <= h/2)])
    totc[cnt] = np.sum(n_img_gs[np.sqrt((Xs)**2+(Ys)**2) <= h/2])
#    n_img_gs[(abs(Xs) <= h/2) & (abs(Ys) <= h/2)] = 1
#    n_img_gs[np.sqrt((Xs)**2+(Ys)**2) <= h/2] = 1

    cnt += 1

##Cropping#########################################################################
########

crpd_img = np.delete(n_img_gs,Y2,0)
crpd_img = np.delete(crpd_img,Y1,0)
crpd_img = np.delete(crpd_img,X2,1)
crpd_img = np.delete(crpd_img,X1,1)

crpd_Xs = np.delete(Xs,Y2,0)
crpd_Xs = np.delete(crpd_Xs,X2,1)
crpd_Xs = np.delete(crpd_Xs,Y1,0)
crpd_Xs = np.delete(crpd_Xs,X1,1)

crpd_Ys = np.delete(Ys,Y2,0)
crpd_Ys = np.delete(crpd_Ys,X2,1)
crpd_Ys = np.delete(crpd_Ys,Y1,0)
crpd_Ys = np.delete(crpd_Ys,X1,1)

crpd_Xp = np.delete(Xp,Y2,0)
crpd_Xp = np.delete(crpd_Xp,X2,1)
crpd_Xp = np.delete(crpd_Xp,Y1,0)
crpd_Xp = np.delete(crpd_Xp,X1,1)

crpd_Yp = np.delete(Yp,Y2,0)
crpd_Yp = np.delete(crpd_Yp,X2,1)
crpd_Yp = np.delete(crpd_Yp,Y1,0)
crpd_Yp = np.delete(crpd_Yp,X1,1)

#################################################################################
########
```

```
Pol = Pol/np.max(n_img_gs)
Pol_avgs = Pol/Pol_cnt
Pol_avg = np.average(Pol/Pol_cnt)

print()
print("Polution Totals: " + str(Pol))
print("Polution Averages: " + str(Pol_avgs))
print("Polution Average: " + str(Pol_avg))
print()

pol = pol/np.max(n_img_gs)
pol_avgs = pol/pol_cnt
pol_avg = np.average(pol/pol_cnt)

print()
print("Polution Boundary Totals: " + str(pol))
print("Polution Boundary Averages: " + str(pol_avgs))
print("Polution Boundary Average: " + str(pol_avg))
print()

intf = totc/tot*100

print()
print('Total:' + str(tot))
print()
print('Intercept Factor : ' + str(np.round(intf,0)))
print('Aperture diameter :' + str(ap))

sfIF = np.array([ap,intf])
sfIF = np.transpose(sfIF)

##RADIATION FLUX#############################################################
########

Qsolar = DNI*Adish
Qts1 = Qsolar*Ref*OptEff

def RootErrorSqr(Qpeak):
    Qfm = Qpeak*n_img_gs
    Qts2 = np.sum(Qfm)

    a = np.sqrt((Qts1-Qts2)**2)
    return a

ans = opt.minimize(RootErrorSqr,[100], method = 'Nelder-Mead')
print(ans)

Qts_peak = ans.x
Qts_tot = np.sum(Qts_peak*n_img_gs)
Qts_fm = Qts_peak*n_img_gs

Its_fm = Qts_fm/(A_pixel/1000**2)

print()
print("Expected radiation on target surface:",Qts1,"W")
print("Estimated radiation on target surface:",Qts_tot,"W")
print("Peak flux:",np.max(Its_fm),"W/m2")
```

```
##OUTPUT#########################################################################
########

plt.figure(1) #Flux map with indexed array
plt.title('Indexed Pixel Distribution')
plt.contourf(Xp, Yp, n_img_gs, 100)
plt.set_cmap('jet')
plt.colorbar(ticks=np.linspace(0,1,11))
plt.xlabel('Horizontal [Index]')
plt.ylabel('Verticle [Index]')
#
#plt.figure(2) #Flux map with actual pixel array
#plt.title('Actual Pixel Distribution')
#plt.contourf(Xp_a, Yp_a, n_img_gs, 100)
#plt.set_cmap('jet')
#plt.colorbar(ticks=np.linspace(0,1,11))
#plt.xlabel('Horizontal [Pixel]')
#plt.ylabel('Verticle [Pixel]')

plt.figure(3) #Flux map with scaled distance array
plt.title('Scaled Pixel Distribution')
plt.contourf(Xs, Ys, n_img_gs, 100)
plt.set_cmap('jet')
plt.colorbar(ticks=np.linspace(0,1,11))
plt.xlabel('x-coordinate [mm]')
plt.ylabel('y-coordinate [mm]')

plt.figure(4) ##Radiation fluxmap
plt.contourf(Xs, Ys, Its_fm, levels = 100)
plt.set_cmap('jet')
plt.colorbar(ticks=np.linspace(0,np.max(Its_fm),11))
plt.xlabel('x-coordinate [mm]')
plt.ylabel('y-coordinate [mm]')

plt.figure(5)
plt.title('Interception Factor')
plt.plot(ap,intf,'.:')
plt.ylabel("Interception Factor [%]")
plt.xlabel("Aperture Diameter [mm]")
plt.grid()

plt.figure(6)
plt.title('Interception Factor')
plt.plot(Adish/ap**2/1000**2,intf,'.:')
plt.xscale('log')
plt.ylabel("Interception Factor [%]")
plt.xlabel("Geometric Concetration Ratio (Aap/Adish)")
plt.grid()

plt.figure(7)
#plt.plot(ys[:,0],Vert_flux,'.', linewidth=2, markersize=12)
plt.plot(Ys[:,0],Vert_flux,'.', markersize = 2)
plt.ylabel("Normalized Flux")
plt.xlabel("y coordinates [mm]")
plt.grid()

plt.figure(8)
plt.plot(Xs[0,:],Hor_flux,'.', markersize = 2)
```

```
plt.ylabel("Normalized Flux")
plt.xlabel("x coordinates [mm]")
plt.grid()

plt.figure(9) #Flux map with indexed array
plt.title('Indexed Pixel Distribution')
plt.contourf(crpd_Xp,crpd_Yp,crpd_img, 100)
plt.set_cmap('jet')
plt.colorbar(ticks=np.linspace(0,1,11))
plt.xlabel('Horizontal [Index]')
plt.ylabel('Verticle [Index]')

plt.figure(10) #Flux map with scaled distance array
plt.title('Scaled Pixel Distribution')
plt.contourf(crpd_Xs,crpd_Ys,crpd_img, 100)
plt.set_cmap('jet')
plt.colorbar(ticks=np.linspace(0,1,11))
plt.xlabel('x-coordinate [mm]')
plt.ylabel('y-coordinate [mm]')

plt.show()

####Save Working Data#################################################
########
root = tk.Tk()
root.withdraw()
saveFilePath  =  fd.asksaveasfilename(
                                        initialdir = "/",
                                        title = "Save Intercept Factor
Data",
                                     )
print(saveFilePath)

seq = ""
fn = saveFilePath + "(npol).csv"
#while osp.isfile(fn%seq):
#    seq = int(seq or 0) + 1
#fn = fn % seq

print(fn)

np.savetxt(
            fn,
            sfIF,
            delimiter = ','
           )
fn = saveFilePath + "_VF(npol).csv"
np.savetxt(
            fn,
            [Ys[:,0],Vert_flux],
            delimiter = ','
           )
fn = saveFilePath + "_HF(npol).csv"
np.savetxt(
            fn,
            [Xs[0,:],Hor_flux],
            delimiter = ','
           )
```

```
fn_mat = saveFilePath + "(npol).mat"

mdic = {
        "X": crpd_Xs,
        "Y": crpd_Ys,
        "Z": crpd_img,
        }

io.savemat(fn_mat,mdic)
```

Appendix B: Python code for surface fitting

B.1 Introduction

The Python code was developed to process the photogrammetry data that was captured.

B.2 Python Code

```
# -*- coding: utf-8 -*-
"""
Created on Thu Oct 3 13:00:05 2019

@author: jonsw
"""

##Load Modules############################################################
import numpy as np
import pandas

import tkinter as tk
from tkinter import filedialog as fd

import scipy.optimize as opt

import matplotlib.pyplot as plt

##INPUTS#################################################################

#Stages = np.arange(0,20,1)
Stages = [0]
iterations = 10000
it = 10
e = 2 ##Choose equation 1 or 2

Equal_scaling = 0

Boundary_nodes = [1114,1117,1266]##enter 3 IDs of nodes at boundary

Ref_nodes = [1000,1001,1002,1003,1004,1005,1006,1007]

short = [1100,1102,1274,1273]
long = [1135,1213,1152,1233]

##GET FILE PATH##########################################################

root = tk.Tk()
root.withdraw()

fp = fd.askopenfilename()

print(fp)

C1 = np.array([])
C2 = np.array([])
C3 = np.array([])
E = np.array([])

for Stage in Stages:
```

```
    print(Stage)

    df = pandas.read_csv(fp)
    df = df.loc[(df['Stage'] == Stage) &
                (~df['ID/Name'].isin(Ref_nodes))]
    df1 = df.loc[(df['Stage'] == Stage) &
                 (~df['ID/Name'].isin(Ref_nodes))]
    bdf = df.loc[(df['Stage'] == Stage) &
                 (df['ID/Name'].isin(Boundary_nodes))]

    ##GET DATA###############################################################

    Stage_data = df['ID/Name']
    x = df['X']
    y = df['Y']
    z = df['Z']

    #pts = [Stage_data,x,y,z]

    bStage_data = bdf['ID/Name']
    bx = bdf['X']
    by = bdf['Y']
    bz = bdf['Z']

    ##FUNCTIONS##############################################################

    e1_EllipticalParaboloid = lambda x: ((xn - x[2])**2/x[0]**2 +
                                         (yn - x[3])**2/x[1]**2 +
                                         x[4]) ##Elliptical prabaloid

    e2_HemiEllipsoid = lambda x: (x[2] * np.sqrt(1 -
                                  (xn - x[3])**2/x[0]**2 -
                                  (yn - x[4])**2/x[1]**2) +
                                   x[5]) ##Hemmi Ellipsoid
    if e==1:
        cons = ({'type':'ineq','fun': lambda x: x[0] > 0},
                {'type':'ineq','fun': lambda x: x[1] > 0})

    if e==2:
        cons = ({'type':'ineq','fun': lambda x:
                 (1 - (xn + x[3])**2/x[0]**2 -
                 (yn + x[4])**2/x[1]**2) >= 0})

def RotateXYZ(rx,ry,rz):

        pt = [x,y,z]

        Rx = np.array([[1,0,0],
                       [0,np.cos(rx),-np.sin(rx)],
                       [0,np.sin(rx),np.cos(rx)]])

        Ry = np.array([[np.cos(ry),0,np.sin(ry)],
                       [0,1,0],
                       [-np.sin(ry),0,np.cos(ry)]])

        Rz = np.array([[np.cos(rz),-np.sin(rz),0],
                       [np.sin(rz),np.cos(rz),0],
                       [0,0,1]])
```

```
    ptn = np.dot(Rx,pt)
    ptn = np.dot(Ry,ptn)
    ptn = np.dot(Rz,ptn)

    return ptn

def Compare_norms(r):
    rx = r[0]
    ry = r[1]
    rz = r[2]

    ref_norm = np.array([0,0,1])

    rotpt = RotateXYZ(rx,ry,rz)

    df1['X'] = rotpt[0]
    df1['Y'] = rotpt[1]
    df1['Z'] = rotpt[2]

    bdf1 = df1.loc[(df1['Stage'] == Stage) &
                   (df1['ID/Name'].isin(Boundary_nodes))]

    bx1 = np.array(bdf1['X'])
    by1 = np.array(bdf1['Y'])
    bz1 = np.array(bdf1['Z'])

    v1 = [bx1[0]-bx1[1],by1[0]-by1[1],bz1[0]-bz1[1]]
    v2 = [bx1[1]-bx1[2],by1[1]-by1[2],bz1[1]-bz1[2]]

    norm = np.cross(v1,v2)

    unorm = norm/np.max(norm)

    error = np.sum((ref_norm-unorm)**2) ##Error Sum Of Squares

    return error

def RMSE(C):
    if e == 1:
        estz = e1_EllipticalParaboloid(C)
    if e == 2:
        estz = e2_HemiEllipsoid(C)

    ans = np.sum(np.sqrt((zn-estz)**2)/len(zn))
    return ans

def symetry_check(rz):

    Xi,Yi = RotateZ(rz)

    ansx1 = (np.sum(np.abs(Xi[(Xi > 0) &
            (Yi > 0)])) - np.sum(np.abs(Xi[(Xi < 0) &
            (Yi > 0)])))
    ansx2 = (np.sum(np.abs(Xi[(Xi > 0) &
            (Yi < 0)])) - np.sum(np.abs(Xi[(Xi < 0) &
            (Yi < 0)])))
    ansx = (ansx1 + ansx2)*10**9
```

```
    ansy1 = (np.sum(np.abs(Yi[(Yi > 0) & (Xi > 0)])) -
             np.sum(np.abs(Yi[(Yi < 0) & (Xi > 0)])))
    ansy2 = (np.sum(np.abs(Yi[(Yi > 0) & (Xi < 0)])) -
             np.sum(np.abs(Yi[(Yi < 0) & (Xi < 0)])))
    ansy = (ansy1 + ansy2)*10**9

    ans = np.sqrt(ansx**2+ansy**2)

    return ans

def RotateZ(rz):

    rz = np.radians(rz)
    Rz = np.array([[np.cos(rz),-np.sin(rz),0],
                   [np.sin(rz),np.cos(rz),0],
                   [0,0,1]])

    pt = [xn,yn,zn]
    ptn = np.dot(Rz,pt)

    return ptn[0],ptn[1]

##PROCESS Results#####################################################

print("Aligning Normals")
a = opt.minimize(Compare_norms,[1,1,1])
print(a)
print()
Rotpts = RotateXYZ(a.x[0],a.x[1],a.x[2])
xn = Rotpts[0]
yn = Rotpts[1]
zn = Rotpts[2]

print("Adjusting Centroid")
x_centroid = np.sum(xn)/np.count_nonzero(np.abs(xn)+1)
y_centroid = np.sum(yn)/np.count_nonzero(np.abs(yn)+1)
print(x_centroid,y_centroid)
print()

xn = xn - x_centroid
yn = yn - y_centroid

x_centroid = np.sum(xn)/np.count_nonzero(np.abs(xn)+1)
y_centroid = np.sum(yn)/np.count_nonzero(np.abs(yn)+1)
print(x_centroid,y_centroid)
print()

print("Rotating in Z")
init = [30]
for i in range(it):
    a = opt.minimize(symetry_check,init, tol = 1e-14)
    init = a.x

    print("Iteration: ",
          str(i+1), "Guess:",
          str(a.x),
          " Complete, Error: ",
```

```
                str(a.fun))
            print()
        print(a)
        print()
        xn,yn = RotateZ(a.x[0])

        df1['X'] = xn
        df1['Y'] = yn
        df1['Z'] = zn
        bdf1 = df1.loc[(df1['Stage'] == Stage) &
                       (df1['ID/Name'].isin(Boundary_nodes))]

        bStage_data1 = np.array(bdf1['ID/Name'])
        bx1 = np.array(bdf1['X'])
        by1 = np.array(bdf1['Y'])
        bz1 = np.array(bdf1['Z'])

        height = np.average(bz1)
        bz1 = bz1 - height
        zn = zn - height

        E = np.array([])

        if e == 1:
            initial = (1,1,1,1,1)
#        if e == 2:
#            initial = (1,1,1,1)
        if e == 2:
            initial = (1000,800,-900,0,0,800)
        print("Fitting Suface Plot")
        for i in range(iterations):

            a = opt.minimize(RMSE,
                             initial,
                             method = 'COBYLA',
                             constraints = cons,
                             tol=1e-6)
            initial = a.x
            E = np.append(E,a.fun)

            print("Iteration: " +
                  str(i+1) +
                  " Complete, Error: " +
                  str(a.fun) +
                  "Coefficients:" +
                  str(initial))

        print(a)

        if e == 1:
            c1 = a.x[0]
            c2 = a.x[1]
            c3 = a.x[2]
            c4 = a.x[3]
            c5 = a.x[4]

            ze = e1_EllipticalParaboloid([c1,c2,c3,c4,c5])
        if e == 2:
```

```
        c1 = a.x[0]
        c2 = a.x[1]
        c3 = a.x[2]
        c4 = a.x[3]
        c5 = a.x[4]
        c6 = a.x[5]

        ze = e2_HemiEllipsoid([c1,c2,c3,c4,c5,c6])

    Ec = ze - zn

    C1 = np.append(C1,c1)
    C2 = np.append(C2,c2)
    C3 = np.append(C3,c3)

##Creat Surface Plot#####################################################
#set equal scaling
if Equal_scaling:

    max_range = np.array([x.max()-x.min(),
                          y.max()-y.min(),
                          z.max()-z.min()]).max() / 2.0
    mid_x = (x.max()+x.min()) * 0.5
    mid_y = (y.max()+y.min()) * 0.5
    mid_z = (z.max()+z.min()) * 0.5

    max_rangen = np.array([xn.max()-xn.min(),
                           yn.max()-yn.min(),
                           zn.max()-zn.min()]).max() / 2.0
    mid_xn = (xn.max()+xn.min()) * 0.5
    mid_yn = (yn.max()+yn.min()) * 0.5
    mid_zn = (zn.max()+zn.min()) * 0.5

fig = plt.figure('Original Coordinates')
ax = fig.add_subplot(111, projection='3d')
ax.plot_trisurf(x,y,z, cmap= 'plasma')
if Equal_scaling:
    ax.set_xlim(mid_x - max_range, mid_x + max_range)
    ax.set_ylim(mid_y - max_range, mid_y + max_range)
    ax.set_zlim(mid_z - max_range, mid_z + max_range)


fig = plt.figure('Adjusted Coordinates With Surface')
ax = fig.add_subplot(111, projection='3d')
ax.plot_trisurf(xn,yn,ze, cmap= 'inferno')
ax.scatter(xn,yn,zn, c = 'green')
ax.set_xlabel('x [mm]')
ax.set_ylabel('y [mm]')
ax.set_zlabel('z [mm]')
if Equal_scaling:
    ax.set_xlim(mid_xn - max_rangen, mid_xn + max_rangen)
    ax.set_ylim(mid_yn - max_rangen, mid_yn + max_rangen)
    ax.set_zlim(mid_zn - max_rangen, mid_zn + max_rangen)


plt.figure()
plt.plot(Stages,C1,'.:')
plt.plot(Stages,C2,'.:')
```

```
plt.xticks(Stages)
plt.legend(['C1','C2'])

plt.figure()
plt.plot(Stages,C3,'.:')
plt.xticks(Stages)
plt.legend(['C1','C2'])

plt.figure('Errors')
plt.plot(np.arange(0,iterations),np.round(E,15),':')
plt.ylabel("RMS Error [mm]")
plt.xlabel("Iterations")
plt.xscale("log")
plt.yscale("log")
plt.grid()


plt.figure('Error Contour')
plt.tricontourf(xn,yn,Ec, 100)
plt.set_cmap('inferno')
plt.colorbar(ticks=np.linspace(np.min(Ec),np.max(Ec),11))
plt.xlabel('x [mm]')
plt.ylabel('y [mm]')

plt.show()
```

Appendix C: Calibration

C.1 Introduction

Calibration of the primary measurement sensors was performed to determine their respective correction coefficients with regard to a reference standard. The primary measurement sensors used in the current research are the insertion thermocouples, the pressure transducers and the load cell. The detail on the method of calibration and the resulting correction correlations is presented in the following sections.

C.2 Thermocouples

The ten K-type insertion thermocouples used to measure the temperature of the process steam were calibrated by exposing the thermocouples to a uniform temperature environment and measuring their respective readings in comparison with the reference standard. A correlation between the measured value and the reference measurement was then determined for a temperature range of 15 to 650 °C. The linear correlation was established through an LMS fit, which was then used to calculate the standard uncertainty of the temperature measurements.

The reference standard used in the thermocouple calibration was a K-type insertion thermocouple of similar manufacturing as the thermocouples being calibrated. The manufacturer calibrated the reference thermocouple and provided a calibration certificate that gave the uncertainty of the thermocouple to be 2.39 °C at a 95% confidence level.

A cylindrical thermal furnace, presented in Figure 67, was used to create the uniform temperature experienced by the insertion thermocouples, and the temperature of the furnace was controlled by a digital load controller. The ten insertion thermocouples and the reference thermocouple had their junctions positioned at the centre of the thermal furnace's cylindrical cavity. Ceramic fibre was used to plug the two apertures on either end of the cavity to minimise heat loss and ensure that the thermocouples experienced a uniform temperature. A schematic of the calibration test set is presented in Figure 68.

During the calibration, the furnace temperature was set to target temperatures within a range of 15 to 650 °C. The target temperature was increased in steps of 50 °C within the given range. The furnace was then left for a duration of roughly 15 minutes to allow the cavity temperature to reach steady state for each temperature step. However, true steady state was never actually reached since the temperature measurements showed a logarithmic decrement as they increased towards the set temperature.

Figure 67: Calibration equipment setup

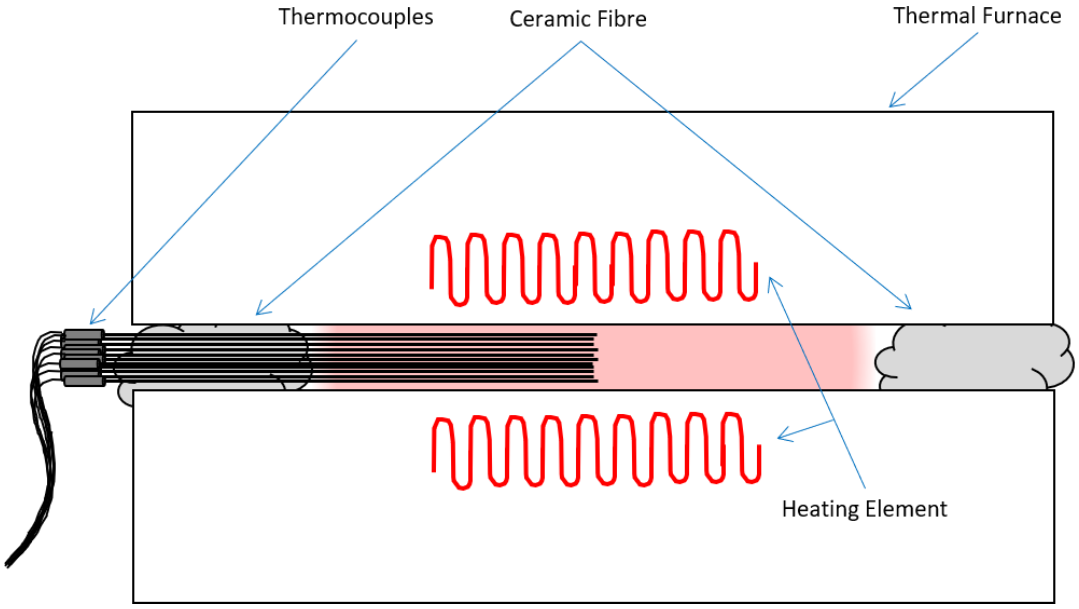

Figure 68: Schematic of thermocouple calibration setup

Calibration curves were developed for the ten thermocouples by plotting the thermocouple reading on the x-axis and the reference thermocouple reading on the y-axis. From this, a least-squares regression line was fit to the data, which had a linear equation that was used as the correction correlation between the thermocouple readings and the reference temperature readings. The resulting plots are presented in Figure 69 and Figure 70. Statistical analysis was applied to the calibrated readings and their respective errors from the reference measurements. This resulted in the determining of the standard deviations of the residuals between the calibrated and the reference measurements. The standard deviations were then used to determine the standard uncertainties of the insertion thermocouples in Appendix D.

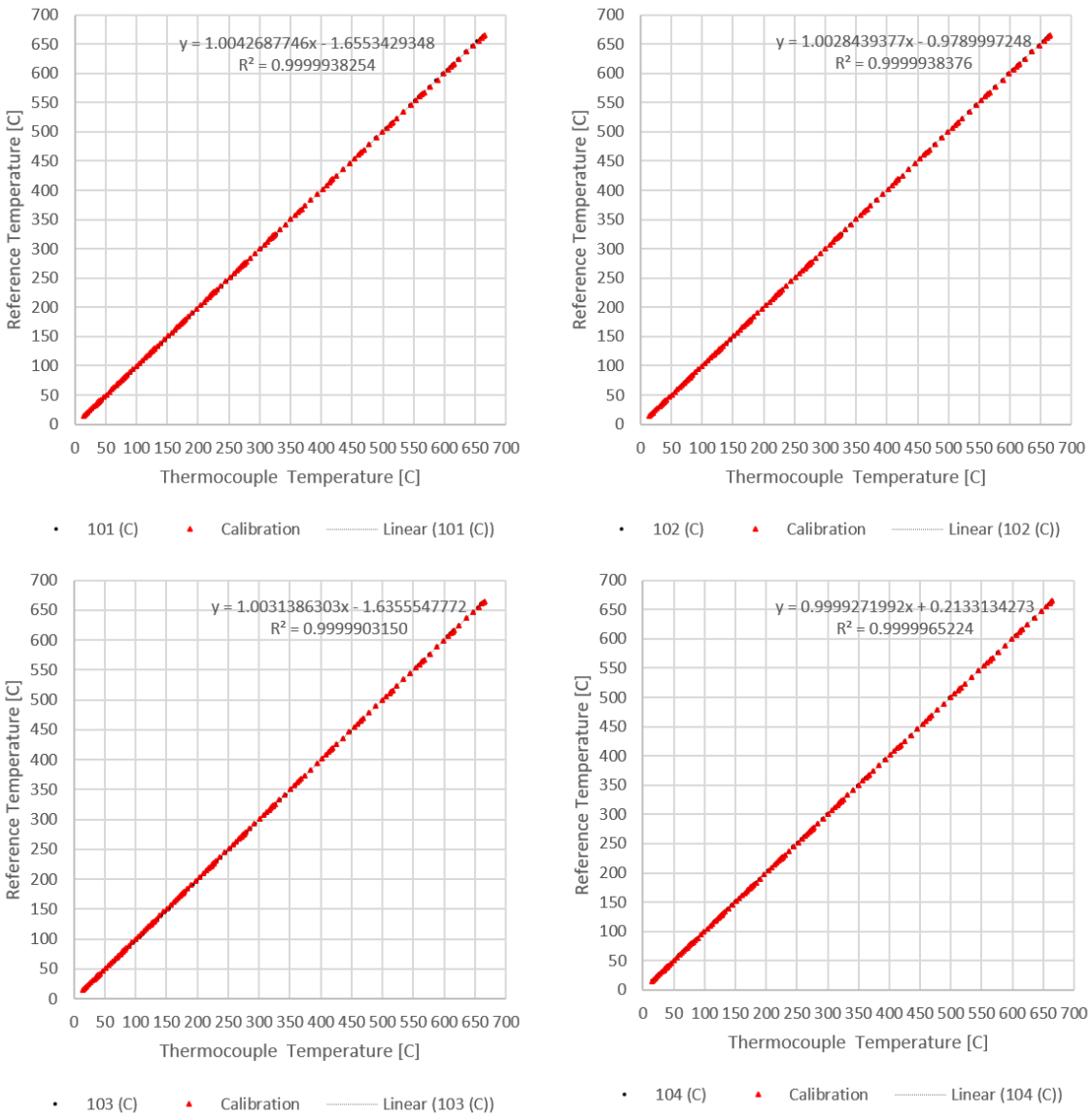

Figure 69: Calibration correlations for TC 1 to TC 4

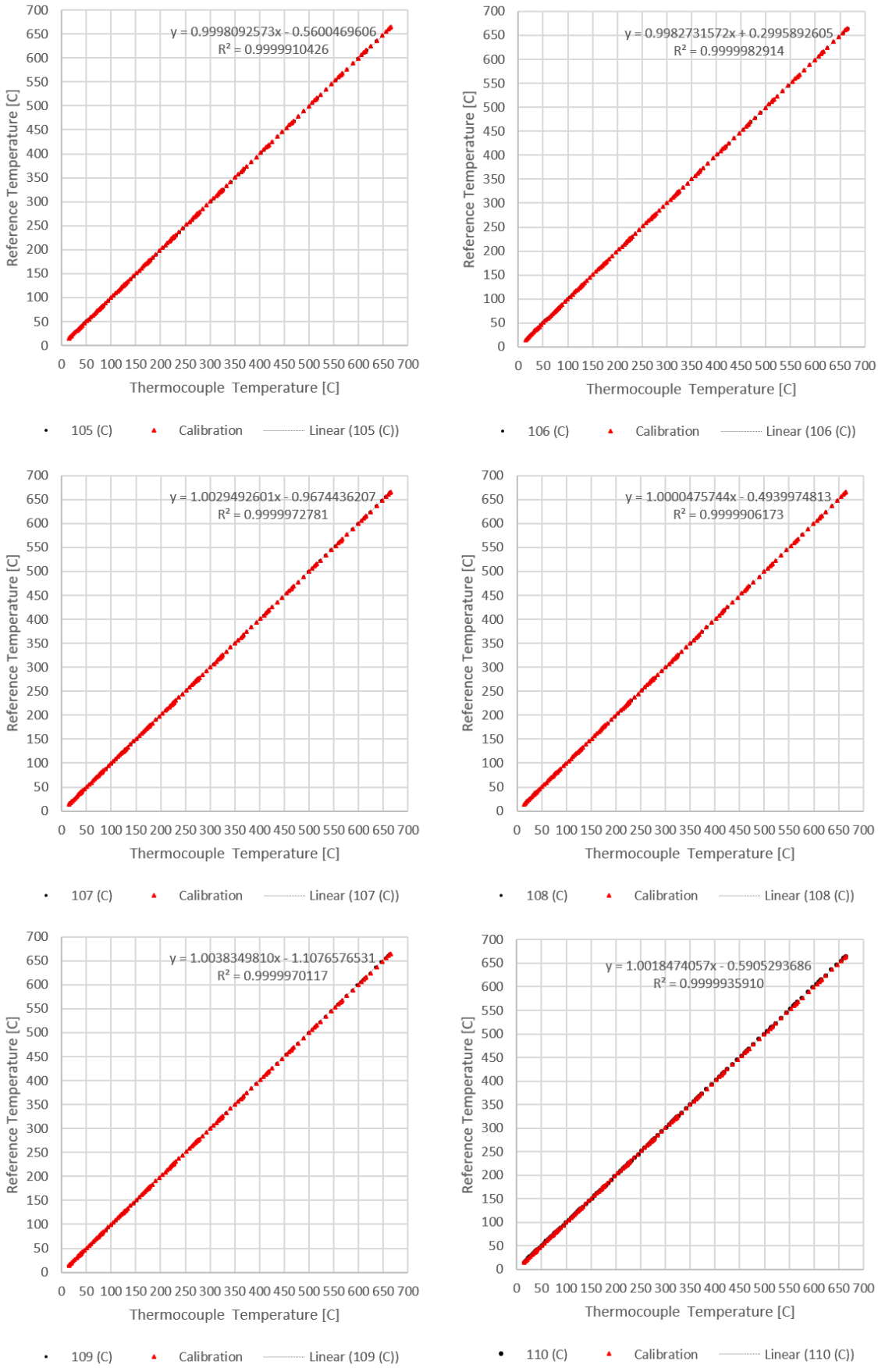

Figure 70: Calibration correlations for TC 5 to TC 10

C.3 Pressure transmitters

The calibration of the pressure transmitters followed a similar process to that of the insertion thermocouples. A linear regression model was used to fit a line to the measured data that correlated the measurements of the pressure transmitters to those of the reference pressure transmitter.

The reference standard used in the calibration of the pressure transmitters was a 10-bar pressure transmitter from WIKA. The reference transmitter was connected to a digital display that read out the measurements, so a process of adjusting the pressure and manually logging the displayed reference pressure was performed during calibration. The reference transmitter had an accuracy within 0.03% according to the calibration certificate.

The two pressure transmitters and the reference pressure transmitter were connected to a manifold that was, in turn, connected to a pneumatic line, shown in Figure 71. The pneumatic line was set to regulated pressures within a range of 87 to 800 kPa and was adjusted in steps of 50 kPa within the given range.

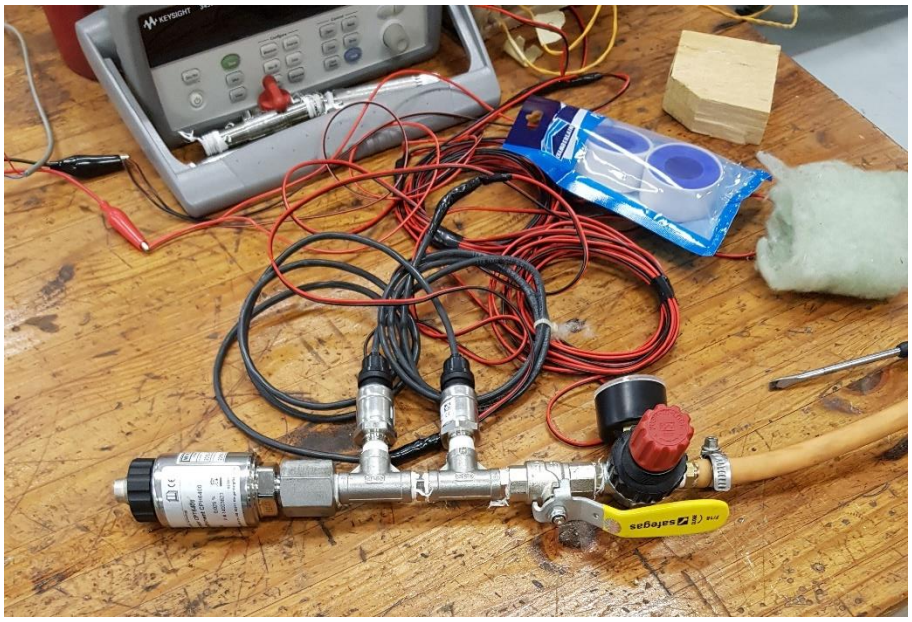

Figure 71: Pressure transmitter calibration setup

The calibration curves for the pressure transmitters were developed using the linear regression model and are presented in Figure 72. The pressure transmitters had a voltage output that was fitted to the reference pressure readings using the correction correlations.

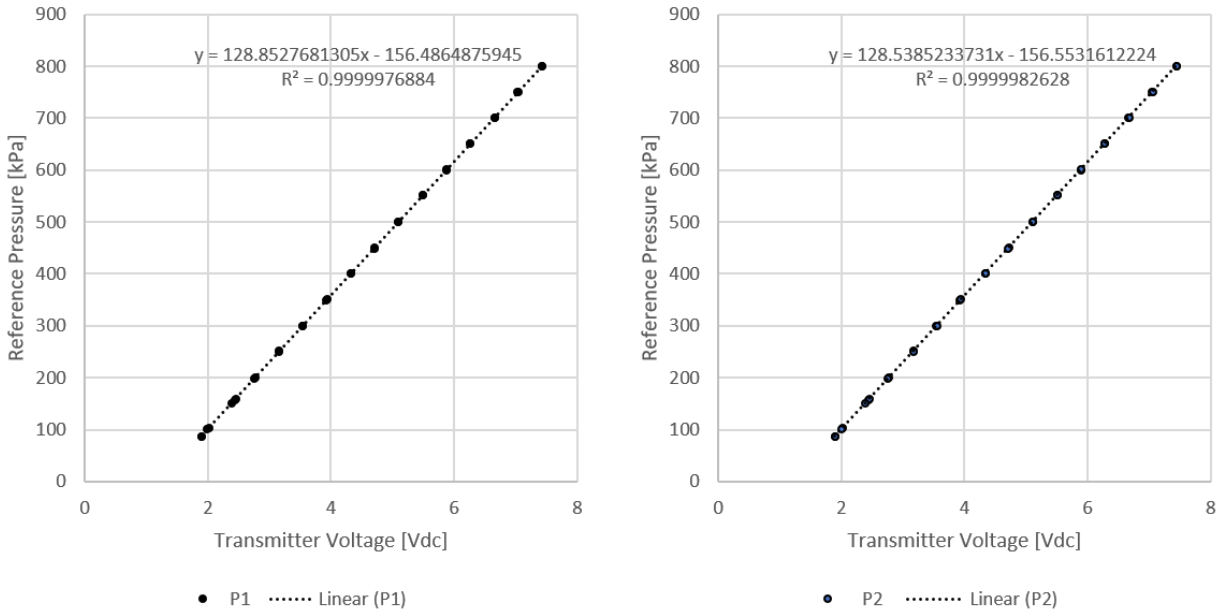

Figure 72: Calibration curves for P 1 and P 2

C.4 Load cell

The 20 kg load cell was calibrated using a set of reference weights within a range of 0 to 8 536 g. The weights were sequentially loaded onto the load cell and the respective voltage across the load cell was measured.

The masses of the reference weights were determined using a scale that was accurate to 1 g. The masses varied according to Table 24.

Table 24: Reference weights used in the calibration of the load cell.

Property	**Value (g)**
Weight mount	544
Weight 1	458
Weight 2	458
Weight 3	1 031
Weight 4	1 145
Weight 5	1 924
Weight 6	2 976

By loading the holder sequentially with the reference weights, a correlation between the voltage response of the load cell and the reference weight being measured could be developed using a linear regression model. The results are presented in Figure 73.

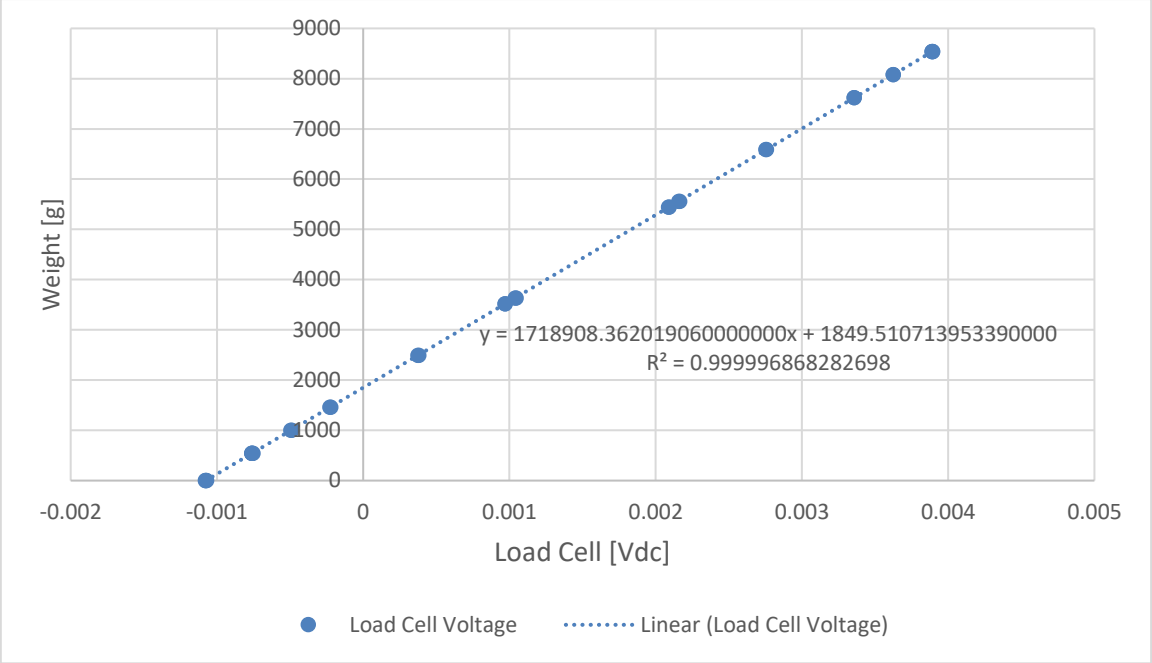

Figure 73: Calibration curve for the load cell

Appendix D: Uncertainty analysis

D.1 Introduction

When justifying experimental results, it is important to determine the uncertainty of the measurements taken during testing in order for readers to gauge the reliability of the results. Uncertainty of measurement is defined by the ISO/IEC Guide 98-3:2008 [1], as the "parameter, associated with the result of a measurement that characterises the dispersion of the values that could reasonably be attributed to the measurand." The uncertainty of the DNI, the captured heat flux and the first- and second-law efficiencies of the solar receiver are determined in the following paragraphs. These are the fundamental output parameters that were analysed in the experimental analysis in Chapter 5. This is done by determining the combined standard uncertainty, and later, the expanded uncertainty of the output parameters as functions of the respective measurement uncertainties of the sensor equipment used.

D.2 Fundamental correlations

Standard uncertainty is referred to as the uncertainty of a measured quantity, which is statistically expressed as a standard deviation [1]. The standard uncertainty of a measurement is typically determined as a function of two variables: the measurement bias and the measurement precision. The measurement bias refers to the accuracy or deviation of the measurement from the true value or measurand and occurs as a result of manufacturing. Measurement precision refers to the grouping of measured data around a mean that deviates from the measurand. Precision errors typically occur due to handling errors such as calibration error or the mishandling of the test equipment. Precision errors are difficult to determine and will not be addressed in the current study. The measurement bias is typically determined after the calibration of the device where a linear correlation between the reference standard and the measurement device has been determined through linear regression. Using the n number of corrected measurements, the deviation of the measurements from the reference standard (x_{ref}), otherwise known as measurement bias, can be determined using Equation D-1.

$$b_i = \sqrt{\frac{\sum_{j=1}^{n}\left(x_{i,j} - x_{ref,j}\right)^2}{n-1}} \tag{D-1}$$

The standard uncertainty of the measurement device is then determined by considering the root sum of squares between the measurement bias and the standard uncertainty of the reference standard as presented in Equation D-2.

$$\delta(x_i) = \sqrt{b_i^2 + \delta^2(x_{ref})} \tag{D-2}$$

In cases where the manufacturer has calibrated the measurement device, the measurement bias may be presented in technical documentation or supporting literature. Measurement bias can be presented in many different ways, but a slight manipulation of the data provided will lead to a standard uncertainty. An important point to note is that if symmetrical bounds are given for the accuracy of a measurement device (i.e. $X_i = x_i \pm a_i$), and no other information is given with regard to these bounds, the convention according to the ISO/IEC Guide 98-3:2008 [1] is followed and a rectangular probability distribution is assumed. This means that the probability that a measurement will occur within these bounds is 1 and the probability that a measurement will fall outside these bounds is effectively 0. The bias would thus be determined using Equation D-3.

$$\delta(x_i) = \sqrt{\frac{a_i^2}{3}} \tag{D-3}$$

In most cases, the measurements are used in a relationship to determine an output parameter (y_i), which is then used in an analysis. In other words, an output parameter is a function of an N number of measurement inputs and can be written according to Equation D-4.

$$y = f(x_1, x_2, \dots, x_N) \tag{D-4}$$

Combined standard uncertainty is referred to as the resulting uncertainty of an output parameter that is a function of other uncertainties (i.e. measurement uncertainties like temperature and pressure). The combined standard uncertainty for the given output parameter may be calculated using Equation D-5.

$$\delta(y) = \sqrt{\sum_{i=1}^{N} \left(\frac{\partial f}{\partial x_i}\right)^2 \delta^2(x_i)} \tag{D-5}$$

Expanded uncertainty addresses the distribution of results and provides a confidence interval in which a resulting output is expected to fall within that of the ISO/IEC Guide 98-3:2008 [1]. In order to determine the expanded uncertainty, the standard uncertainty of a measurement or output parameter is multiplied by a factor to obtain an interval in which the measurements will fall with a certain degree of certainty. In statistical analysis, when dealing with a normal distribution, one standard deviation encompasses 68.27% of the possible measurement's values, while two and three standard deviations encompass 95.46 and 99.73% of the possible measurements, respectively. These percentages translate as the level of confidence that the measurement will fall within the given interval.

D.3 Uncertainty of measurements

D3.1 Temperature

The thermocouple's measurements were corrected using the calibration curve that was developed in Appendix C.2. The measurement bias of the corrected thermocouple measurements was then compared to the standard uncertainty of the reference thermocouple and a standard uncertainty was determined for each thermocouple using Equation D-2. The expanded uncertainty was determined by multiplying the standard uncertainty by 2, which accounts for a 95% confidence level. The resulting thermocouple uncertainties are presented in Table 25. The standard uncertainty of the reference thermocouple is simply $\delta(TC_{ref}) = {}^{2.39}/_{2} = 1.20\,°C$.

Table 25: Measurement uncertainties of the thermocouple

Thermocouple	Measurement bias (b_i) (°C)	Standard uncertainty $\delta(x_i)$ (°C)	Expanded uncertainty (95% confidence level) (°C)
TC_{ref}	-	1.2	-
$TC\ 1$	0.94	1.52	3.05
$TC\ 2$	0.57	1.33	2.66
$TC\ 3$	0.98	1.55	3.10
$TC\ 4$	0.19	1.21	2.43
$TC\ 5$	0.61	1.35	2.69
$TC\ 6$	0.36	1.25	2.51
$TC\ 7$	0.57	1.33	2.66
$TC\ 8$	0.48	1.29	2.58
$TC\ 9$	0.71	1.39	2.79
$TC\ 10$	0.35	1.25	2.50

The uncertainty pertaining to the ambient temperature measurements was determined by considering the calibration certificate for the SOLYS 2 weather station. The ambient temperature had an expanded uncertainty of 0.85 °C. Based on Equation D-3, the standard uncertainty of the ambient temperature measurement was 0.49 °C.

D.3.2 Pressure

The pressure transmitter measurements were corrected using the calibration curve that was developed in Appendix C.3. The measurement bias of the corrected pressure measurements was then compared to the standard uncertainty of the reference pressure transmitter, and a standard uncertainty was determined for the two pressure transmitters using Equation D-2. The expanded uncertainty was determined by multiplying the standard uncertainty by 2, which accounts for a 95% confidence level. The resulting pressure transmitter uncertainties are presented in Table 26. The

standard uncertainty of the reference pressure transmitter was determined to be $\delta(P_{ref}) = \sqrt{0.3^2/_3} = 0.17\ kPa$, using Equation D-3.

Table 26: Measurement uncertainties of the pressure transmitters

Pressure transmitter	Measurement bias (b_i) (Pa)	Standard uncertainty $\delta(x_i)$ (Pa)	Expanded uncertainty (95% confidence level) (Pa)
P_{ref}	-	170	-
$P1$	351.87	390.78	781.56
$P2$	305.03	349.20	698.41

The uncertainty pertaining to the ambient pressure measurements was determined by considering the calibration certificate for the SOLYS 2 weather station. The ambient pressure was measured with an expanded uncertainty of 220 Pa. Based on Equation D-3, the standard uncertainty of the ambient pressure measurement was 127 Pa.

D.3.3 Mass

A similar process was followed with the load cell where the measurements were corrected from the calibration curve in Appendix C.4. The standard uncertainty of the reference scale was $\delta(m_{ref}) = 0.5\ g$.

Table 27: Measurement uncertainty of the load cell

Load cell	Measurement bias (b_i) (kg)	Standard uncertainty $\delta(x_i)$ (kg)	Expanded uncertainty (95% confidence level) (kg)
m_{ref}	-	0.5e-3	-
m_w	5.61e-3	5.64e-3	11.28e-3

D.3.4 Time

The measurements were recorded using computer software that also kept track of time throughout the period of testing. Since the software determined test duration based on the computer's clock, the variance in time can be taken to be negligible, in other words, $\delta(t) \approx 0$

D.3.5 Length and area

The lengths associated with the experimental model were mostly determined using a measuring tape with an accuracy of 1 mm. Due to possible handling errors, this was taken as the standard measurement uncertainty ($\delta(L) \approx 1mm$) rather than the assumed symmetrical bounds.

The incident area of the dish was calculated using the equation of an ellipsis as shown in Equation D-6.

$$A_{dish} = 6 \times \pi ab \tag{D-6}$$

The a coefficient is the radius along the major axis and the b coefficient is the radius along the minor axis. These coefficients were determined from length measurements. The standard uncertainty pertaining to the incident area can thus be determined using Equation D-5.

$$\delta(A_{dish}) = \left[\left(\frac{\partial A_{dish}}{\partial L_a}\right)^2 \delta^2(L_a) + \left(\frac{\partial A_{dish}}{\partial L_b}\right)^2 \delta^2(L_b)\right]^{0.5}$$

$$\delta(A_{dish}) = [(6\pi b)^2\, \delta^2(L_a) + (6\pi a)^2 \delta^2(L_b)]^{0.5}$$

$$\delta(A_{dish}) \approx [(6\pi \times 0.76)^2\, (0.001)^2 + (6\pi \times 0.762)^2 (0.001)^2]^{0.5}$$

$$\delta(A_{dish}) \approx 0.02\ m^2$$

D.3.6 Direct normal irradiance

The accuracy of the DNI measurements taken by the SOLYS 2 solar tracker was estimated to have a measurement accuracy within 2% [2]. For the steady-state DNI having been determined in Section 4.5.1 to be 757 W/m^2, this translates to a standard measurement uncertainty of $\delta(I_{sun}) \approx 15.14\ W/m^2$.

D.3.7 Reflectivity

The UV/VIS spectrometer used to measure the transmittance and absorptance of the Mylar specimen was the CARY bio 100 spectrometer. According to the manufacturer's technical specifications, the accuracy of the transmittance and absorptance readings was quoted to be within 1 and 1.2%, respectively [3]. Based on Equation 3-2 used to determine the Mylar sheet reflectance, the standard uncertainty with respect to the reflectance measurement may be determined.

$$1 = \alpha_{mylar} + \rho_{mylar} + \tau_{mylar} \tag{D-7}$$

$$\delta(\rho_{mylar}) = \left[\left(\frac{\partial \rho_{mylar}}{\partial \alpha_{mylar}}\right)^2 \delta^2(\alpha_{mylar}) + \left(\frac{\partial \rho_{mylar}}{\partial \tau_{mylar}}\right)^2 \delta^2(\tau_{mylar})\right]^{0.5}$$

$$\delta(\rho_{mylar}) = [\, \delta^2(\alpha_{mylar}) + \delta^2(\tau_{mylar})]^{0.5}$$

$$\delta(\rho_{mylar}) \approx [\, 0.012^2 + 0.01^2]^{0.5}$$

$$\delta(\rho_{mylar}) \approx 0.016$$

D.3.8 Interception factor

During the lunar flux mapping, a CANON EOS 700D was used to capture the images of the flux distribution on the target surface. The relative error associated with the resulting pixel values was investigated in the work of Ho, and Khalsa [4], who used a NIKON D90 and was estimated to be 3%.

Since the method of lunar flux mapping has been reported to produce flux distributions that differ by up to 7% when compared to on-sun flux distributions, according to Burgess et al. [5], a conservative estimate of the standard uncertainty associated with the intercept factor was made.

The uncertainty of the intercept factor was thus estimated to be:

$$\delta(IF) \approx IF \times \left[\left(\frac{\delta\eta_{camera}}{\eta_{camera}}\right)^2 + \left(\frac{\delta\eta_{LFM}}{\eta_{LFM}}\right)^2\right]^{0.5}$$

$$\delta(IF) \approx 0.87[(0.03)^2 + (0.07)^2]^{0.5}$$

$$\delta(IF) \approx 0.066$$

D.3.9 Fluid properties from the CoolProp library

The CoolProp library used to determine the fluid properties of the working fluid (water) uses the most accurate version of the Helmholtz energy formulation, according to the International Association of Properties of Water and Steam (IAPWS), is presented in Wagner and Pruß [6]. The work provides detail on the uncertainties determined for all the fluid properties pertaining to water (besides enthalpy) at different temperature and pressure states. The uncertainties pertaining to the formulation with regard to determining the specific enthalpy were presented by IAPWS [7].

From the referenced work, it is clear that the Helmholtz energy formulation used by the CoolProp library is able to predict the fluid properties of water (besides enthalpy) to an accuracy within a relative uncertainty of 0.2%. The enthalpy state of water can be determined within an uncertainty of 1 000 J/kg for the given parameter range of the current research. Thus, the standard uncertainties pertaining to the fluid properties may be calculated using Equation D-3.

The standard uncertainty pertaining to the specific enthalpy state of water is calculated as follows.

$$\delta(h_{cp}) \approx \sqrt{\frac{1000^2}{3}}$$

$$\delta(h_{cp}) \approx 577.35\, J/kg$$

D.4 Combined standard uncertainty of output parameters

The test parameters considered for the uncertainty analysis were based on the testing conditions determined during the experimental analysis in Chapter 4. The parameters are summarised in Table 28. The output parameters differ slightly from the experimental results since they were calculated for the given input parameters in Table 28 rather than determining their averages over the test period.

Table 28: Test parameters from the experimental analysis

Parameter	Symbol	Value	Units
Duration of the testing period	Δt	5 460	seconds
Initial mass of water	m_{w1}	5.28	kg
Final mass of water	m_{w2}	6.89	kg
Mass flow rate	$\dot{m}_w$	2.94e-4	kg/s
Inlet temperature	T_1	327.27	Kelvin
Outlet temperature	T_9	616.27	Kelvin
Ambient temperature	T_∞	302.79	Kelvin
Sun temperature	T_{sun}	5 762	Kelvin
Average steam pressure	P_{avg}	3.49e5	Pa
Ambient pressure	P_∞	8.66e4	Pa
Inlet specific enthalpy	h_1	2.27e5	J/kg
Outlet specific enthalpy	h_9	3.16e6	J/kg
Ambient specific enthalpy	h_∞	4.29e5	J/kg
Inlet specific entropy	s_1	756.03	J/kg
Outlet specific entropy	s_9	7 780.90	J/kg
Ambient specific entropy	s_∞	3 941.32	J/kg
Direct normal irradiance	I_{sun}	757.13	W/m^2
Incident dish area	A_{dish}	2.73	m^2
Reflector efficiency	η_{ref}	97	%
Intercept factor	IF	87	%
Intercepted radiation at the aperture	$\dot{Q}_{ap}$	1 744.31	W
Captured heat	ΔH_w	8 62.25	W
Available work of intercepted radiation at the aperture	Φ_{ap}	1 622.09	W
Inlet specific exergy	Ψ_1	224.25	W
Outlet specific exergy	Ψ_9	460.59	W

D.4.1 Mass flow rate

$$\dot{m}_w = \frac{m_{w,2} - m_{w,1}}{\Delta t}$$

$$\delta(\dot{m}_w) = \left[\left(\frac{\partial \dot{m}_w}{\partial m_{w,1}}\right)^2 \delta^2(m_{w,1}) + \left(\frac{\partial \dot{m}_w}{\partial m_{w,2}}\right)^2 \delta^2(m_{w,2}) + \left(\frac{\partial \dot{m}_w}{\partial \Delta t}\right)^2 \delta^2(\Delta t)\right]^{0.5}$$

$$\delta(\dot{m}_w) = \left[\left(-\frac{1}{\Delta t}\right)^2 \times \delta^2(m_{w,1}) + \left(\frac{1}{\Delta t}\right)^2 \times \delta^2(m_{w,2}) + \left(\frac{m_{w,2} - m_{w,1}}{(\Delta t)^2}\right)^2 \times \delta^2(\Delta t)\right]^{0.5}$$

D.4.2 Average pressure

$$P_{avg} = \frac{P_1 + P_2}{2}$$

$$\delta(P_{avg}) = \left[\left(\frac{\partial P_{avg}}{\partial P_1}\right)^2 \delta^2(P_1) + \left(\frac{\partial P_{avg}}{\partial P_2}\right)^2 \delta^2(P_2)\right]^{0.5}$$

$$\delta(P_{avg}) = [0.25 \times \delta^2(P_1) + 0.25 \times \delta^2(P_2)]^{0.5}$$

D.4.3 Fluid properties

D.4.3.1 Specific enthalpy

$$\delta(h) = h \times \left[\left(\frac{\delta h_{cp}}{h_{cp}}\right)^2 + \left(\frac{\delta T_i}{T_i}\right)^2 + \left(\frac{\delta P_{avg}}{P_{avg}}\right)\right]^{0.5}$$

D.4.3.2 Specific entropy

$$\delta(s) = s \times \left[\left(\frac{\delta s_{cp}}{s_{cp}}\right)^2 + \left(\frac{\delta T_i}{T_i}\right)^2 + \left(\frac{\delta P_{avg}}{P_{avg}}\right)^2\right]^{0.5}$$

D.4.3.3 Captured heat

$$\dot{Q}_{net} = \dot{m}_w(h_{out} - h_{in})$$

$$\delta(\dot{Q}_{net}) = \left[\left(\frac{\partial \dot{Q}_{net}}{\partial \dot{m}_w}\right)^2 \delta^2(\dot{m}_w) + \left(\frac{\partial \dot{Q}_{net}}{\partial h_{in}}\right)^2 \delta^2(h_{in}) + \left(\frac{\partial \dot{Q}_{net}}{\partial h_{out}}\right)^2 \delta^2(h_{out})\right]^{0.5}$$

$$\delta(\dot{Q}_{net}) = [(h_{in} - h_{out})^2 \times \delta^2(\dot{m}_w) + (\dot{m}_w)^2 \times \delta^2(h_{in}) + (-\dot{m}_w)^2 \times \delta^2(h_{out})]^{0.5}$$

D.4.3.4 Heat incident at aperture

$$\dot{Q}_{ap} = IF \times \eta_{ref} A_d I_{sun}$$

$$\delta(\dot{Q}_{ap}) = \left[\left(\frac{\partial \dot{Q}_{ap}}{\partial IF}\right)^2 \delta^2(IF) + \left(\frac{\partial \dot{Q}_{ap}}{\partial \eta_{ref}}\right)^2 \delta^2(\eta_{ref}) + \left(\frac{\partial \dot{Q}_{ap}}{\partial A_d}\right)^2 \delta^2(A_d) + \left(\frac{\partial \dot{Q}_{ap}}{\partial I_{sun}}\right)^2 \delta^2(I_{sun})\right]^{0.5}$$

$$\delta(\dot{Q}_a) = \begin{bmatrix} (\eta_{ref} A_d I_{sun})^2 \times \delta^2(IF) \\ +(IF A_d I_{sun})^2 \times \delta^2(\eta_{ref}) \\ +(\eta_{ref} IF I_{sun})^2 \times \delta^2(A_d) \\ +(\eta_{ref} IF A_d)^2 \times \delta^2(I_{sun}) \end{bmatrix}^{0.5}$$

D.4.4 First-law efficiency (receiver)

$$\eta_{th} = \frac{\dot{Q}_{net}}{\dot{Q}_{ap}}$$

$$\delta(\eta_{th}) = \left[\left(\frac{\partial \eta_{th}}{\partial \dot{Q}_i}\right)^2 \delta^2(\dot{Q}_i) + \left(\frac{\partial \eta_{th}}{\partial \dot{Q}_{ap}}\right)^2 \delta^2(\dot{Q}_{ap})\right]^{0.5}$$

$$\delta(\eta_{th}) = \left[\left(\frac{1}{\dot{Q}_{ap}}\right)^2 \delta^2(\dot{Q}_i) + \left(-\frac{\dot{Q}_i}{\dot{Q}_{ap}^2}\right)^2 \delta^2(\dot{Q}_{ap})\right]^{0.5}$$

D.4.5 Exergy

$$\Psi_w = \dot{m}_w[(h_w - h_\infty) - T_\infty(s_w - s_\infty)]$$

$$\delta(\Psi_w) = \left[\left(\frac{\Psi_w}{\partial \dot{m}_w}\right)^2 \delta^2(\dot{m}_w) + \left(\frac{\Psi_w}{\partial h_w}\right)^2 \delta^2(h_w) + \left(\frac{\Psi_w}{\partial h_\infty}\right)^2 \delta^2(h_\infty) + \left(\frac{\Psi_w}{\partial T_\infty}\right)^2 \delta^2(T_\infty) + \left(\frac{\Psi_w}{\partial s_w}\right)^2 \delta^2(s_w) + \left(\frac{\Psi_w}{\partial s_\infty}\right)^2 \delta^2(s_\infty)\right]^{0.5}$$

$$\delta(\Psi_w) = \Big[([(h_w - h_\infty) - T_\infty(s_w - s_\infty)])^2 \times \delta^2(\dot{m}_w) + (\dot{m}_w)^2 \times \delta^2(h_w) + (-\dot{m}_w)^2 \times \delta^2(h_\infty) + \big(-\dot{m}_w(s_w - s_\infty)\big)^2 \times \delta^2(T_\infty) + (-T_\infty \dot{m}_w)^2 \times \delta^2(s_w) + (T_\infty \dot{m}_w)^2 \times \delta^2(s_\infty)\Big]^{0.5}$$

D.4.6 Available work at aperture

$$\Phi_{ap} = \dot{Q}_{ap}\left[1 - \frac{4T_\infty}{3T_{sun}}\right]$$

$$\delta(\Phi_{ap}) = \left[\left(\frac{\partial \Phi_{ap}}{\partial \dot{Q}_{ap}}\right)^2 \delta^2(\dot{Q}_{ap}) + \left(\frac{\partial \Phi_{ap}}{\partial T_\infty}\right)^2 \delta^2(T_\infty)\right]^{0.5}$$

$$\delta(\Phi_{ap}) = \left[\left(1 - \frac{4T_\infty}{3T_{sun}}\right)^2 \delta^2(\dot{Q}_{ap}) + \left(-\frac{4\dot{Q}_{ap}}{3T_{sun}}\right)^2 \delta^2(T_\infty)\right]^{0.5}$$

D.4.7 Second-law efficiency

$$\eta_{2nd} = \frac{\Psi_{\text{out}} - \Psi_{\text{in}}}{\Phi_{ap}}$$

$$\delta(\eta_{2nd}) = \left[\left(\frac{\partial \eta_{2nd}}{\partial \Psi_{\text{out}}}\right)^2 \delta^2(\Psi_{\text{out}}) + \left(\frac{\partial \eta_{2nd}}{\partial \Psi_{in}}\right)^2 \delta^2(\Psi_{\text{in}}) + \left(\frac{\partial \eta_{2nd}}{\partial \Psi_{out}}\right)^2 \delta^2(\Psi_{out})\right]^{0.5}$$

$$\delta(\eta_{2nd}) = \left[\left(\frac{1}{\Phi_{ap}}\right)^2 \times \delta^2(\Psi_{\text{out}}) + \left(-\frac{1}{\Phi_{ap}}\right)^2 \times \delta^2(\Psi_{\text{in}}) + \left(\frac{\Psi_{\text{out}} - \Psi_{\text{in}}}{\Phi_{ap}^2}\right)^2 \times \delta^2(\Psi_{out})\right]^{0.5}$$

D.5 References

[1] ISO/IEC Guide 98-3:2008, "Uncertainty of measurement – Part 3: Guide to the expression of uncertainty in measurement (GUM:1995)," ISO/IEC, Geneva, Switzerland, 2008.

[2] N. Geuder, S. Wilbert, and N. Janotte, "Precise measurements of solar beam irradiance through improved sensor calibration," in *Proceedings of SolarPACES 2009*, Berlin, Germany, pp. 1–8, 2009.

[3] Agilent, 2019. "*Cary 100 UV-Vis,"* available at: https://www.agilent.com. [accessed on: 23/06/2019].

[4] C. K. Ho, and S. S. Khalsa, "A photographic flux mapping method for concentrating solar collectors and receivers," *Journal of Solar Energy Engineering,* vol. 134, no. 4, p. 041004, 2012.

[5] G. Burgess, J. Zapata, R. Chauvin, M. Shortis, J. Pye, and J. Preston, "Three-dimensional flux prediction for a dish concentrator cavity receiver," in *Proceedings of SolarPACES 2012*, Marrakech, Morocco, 2012.

[6] W. Wagner, and A. Pruß, "The IAPWS formulation 1995 for the thermodynamic properties of ordinary water substance for general and scientific use," *Journal of Physical and Chemical Reference Data,* vol. 31, no. 2, pp. 387–535, 2002.

[7] IAPWS, "Uncertainties in enthalpy for the IAPWS formulation 1995 for the thermodynamic properties of ordinary water substance for general and scientific use (IAPWS-95) and the IAPWS industrial formulation 1997 for the thermodynamic properties of water and steam (IAPWS-IF97)," in "AN1-03, Advisory Note No. 1," 2003, available at: http://www.iapws.org. [accessed on: 23/08/2019].